Doctoral Dissertation

Properties of Triazasumanene and Related Cyclic Triamides

Sitanan Sartyoungkul

July 2020

Division of Applied Chemistry,
Graduate School of Engineering
Osaka University

Contents

Chapter 1

General Introduction

Chapter 1: General Introduction

1.1 Buckybowls

Polyaromatic hydrocarbon material including graphenes,[1] fullerenes,[2] carbon nanotubes,[3] nanoribbons[4] and buckybowls,[5-8] which have plenty attentions due to their unique structure and properties such as delocalization from π-conjugated system, metal coordination, electron conductivity, dynamic behavior, redox chemistry and host-guest system (Fig. 1). Since fullerene was discovered by H. W. Kroto, R. F. Curl and R. E. Smalley in 1985, large numbers of publications on their properties and reactivities were continuously investigated and published until now. It's well-known that modification or functionalization on their structures lead to dramatically changed in characteristics and properties.

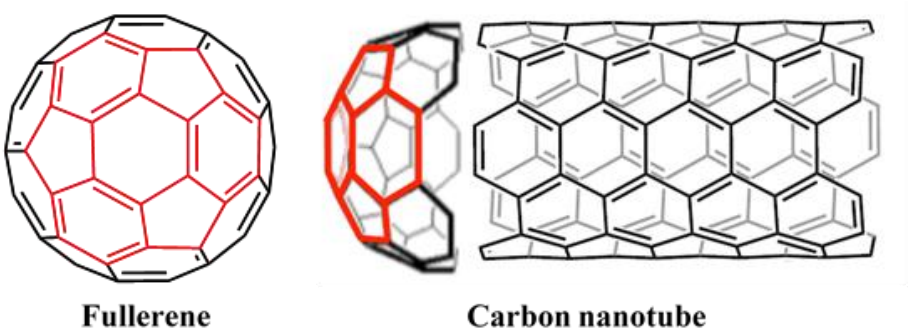

Figure 1. Molecular structure of fullerene and carbon nanotube.

Buckybowls are non-planar aromatic compounds as considered as a partial structure of fullerene such as sumanene,[5] corannulene,[6] diindenochrysene,[7] circumtrindene[8] and so on. Nowadays, there are many attempts to achieve synthesis of fullerene starting from these either small buckybowls. However, difficulty from molecular strain from fused-ring and specific C-C bond construction were main problem that chemists need to consider.

Among the members of buckybowls, sumanene (**1**) and corannulene (**2**), the smallest C_{3v} and C_{5v} symmetry, respectively, are bowl-shaped buckybowls, which their derivatives have been well synthesized and compared in term of structural features and properties.[9,10] They are pristine hydrocarbon buckybowls composed of both pentagon and hexagon. While **1** is consisting of three pentagons located on the rims of the triphenylene, **2** is composed from one center pentagon surrounded by five hexagons (Fig. 2). By external pentagons in **1**, it could lead to the different reactions from **2** and undergo more various kinds of functionalization methods.[11]

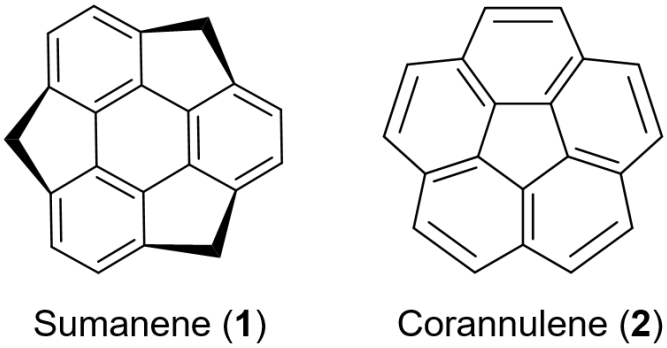

Figure 2. Molecular structure of sumanene (**1**) and corannulene (**2**).

Unique properties could be expected from these bowl-shaped structures such as dynamic bowl-to-bowl inversion or racemization process at 20 °C (Fig. 3),[12] electron conductivity through well-organized columnar packing structure (Fig. 4),[13-15] host-guest interaction[16] and metal coordination.[17] At the present, there are various publications reported their derivatives synthesis and those properties and reactivities have been continued investigated.

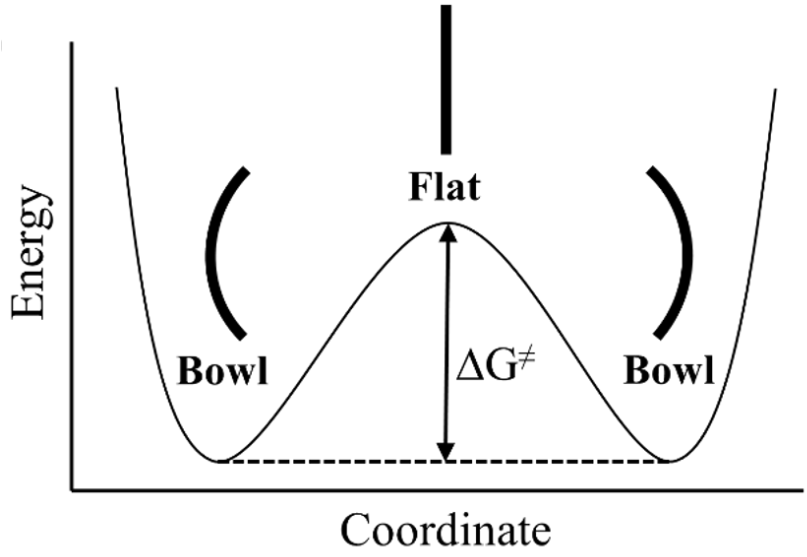

Figure 3. Dynamic bowl inversion of **1** and **2** through flat transition state.

1.2 Nitrogen-doped sumanene, triazasumanene

Introduction of heteroatoms (such as nitrogen, oxygen and boron) to hydrocarbon system is one of practical ways to tune up the physical and chemical properties by electronic perturbation due to lone pair electrons localized around these atoms. Nitrogen atom is popular heteroatoms introduced in flat and curved hydrocarbon system such as graphene, carbon nanotube and fullerene.[18] As a result, the physical and electronic properties are critically changed such as increase surface area,[18b] favorable coordination,[19] higher catalytic activity[20] and increasing charge transfer for supercapacitors.[19b]

The similar strategy takes place on the buckybowls chemistry, nitrogen atoms are nicely introduced in **1** and **2** skeletons and their properties are intensively studied (Fig. 4).[21,22] In 2012, Sakurai *et al* succeeded in the first enantioselective synthesis of C_3 symmetric nitrogen-doped on **1**, triazasumanene, with three MeS or $MeSO_2$ substituents.[22] Finally, an enantioselective synthesis of pristine C_3 symmetric triazasumanene (**3**), has been achieved through desulfurization reaction from tris(methylthio)triazasumanene precursor (**10**) as shown in Scheme 1.[23]

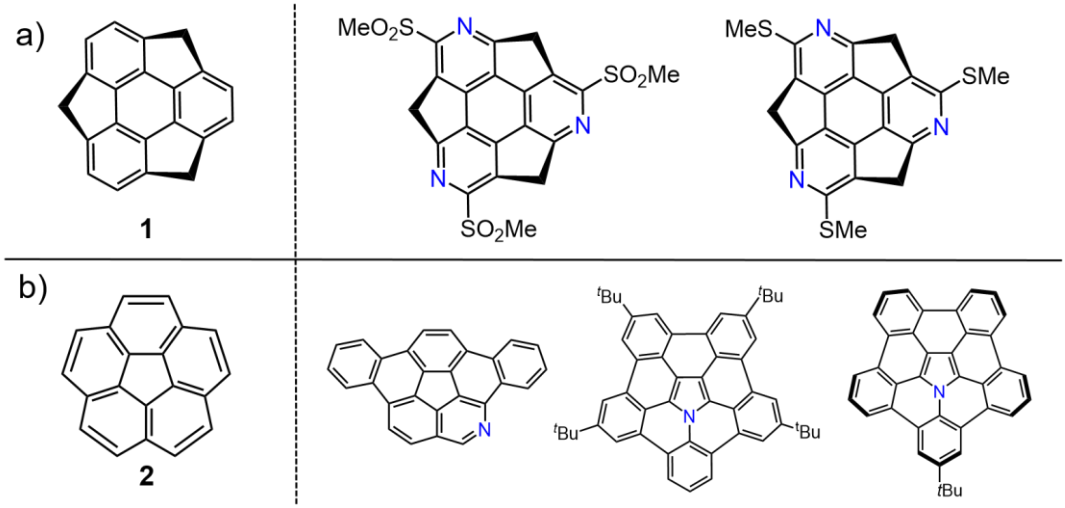

Figure 4. Some of molecular structures of nitrogen-doped on a) **1** and b) **2**.

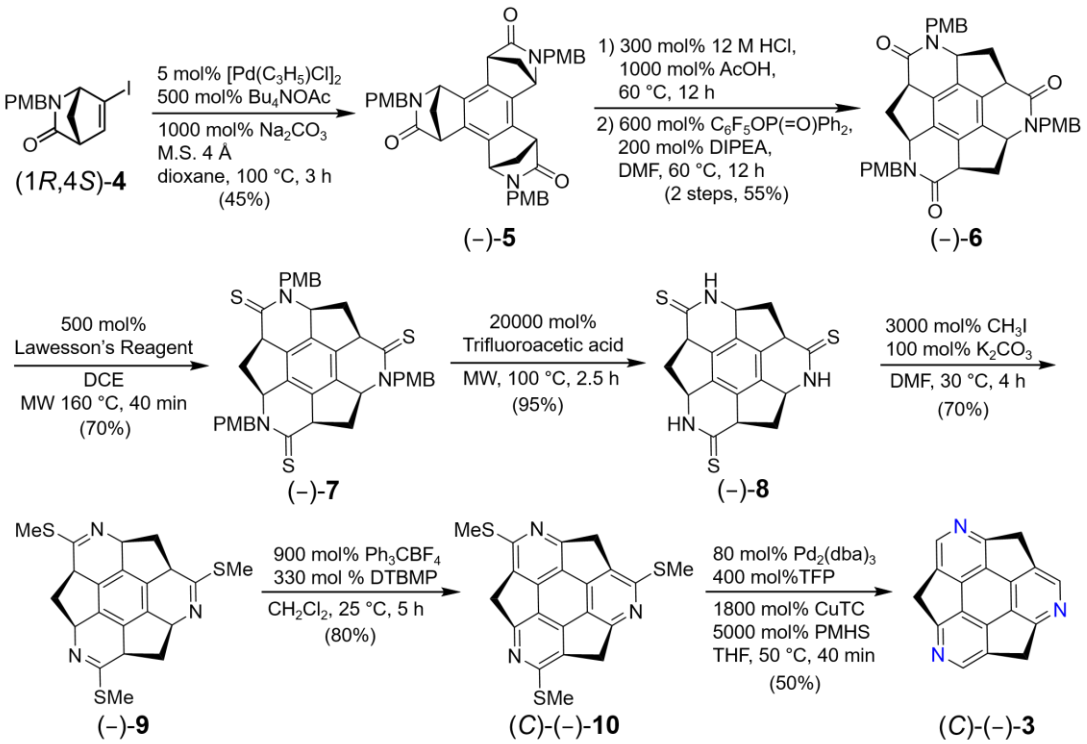

Scheme 1. Enantioselective synthesis of (*C*)-(–)-**3**.

Doping effect of nitrogen significantly affects to change the properties of **3** and its derivatives from **1**.[23] First, **3** showed drastically deeper bowl depth of 1.29 Å than that of **1** (c.f., 1.11 Å). Haddon's π-orbital axis vector (POAV) angle[24] reveals that the central six carbons are pyramidalized to an extent of 9.5 Å and 11.0 Å, respectively, Hence **3** possesses the bowl inversion energy barrier of 42.2 kcal mol^{-1}, which corresponded to 54 billion years for half-lifetime at 20 °C, while **1** is exhibiting fast bowl inversion at the same temperature. As a result, **3** has no racemization leading to stable chiral bowl-shaped structures. It is apparent that nitrogen-doped on the periphery of **1** providing more strained structures. Single X-ray analysis indicated that homochiral **3**, which prepared by slow evaporation of (*C*)-(–)-**3** in CH_2Cl_2/hexane (1:1 v/v) under Ar atmosphere, exhibited bidirectional slippery columnar packing in helical columns, unlike the columnar packing structure found in **1** (Fig. 5). While **1** possesses π···π interaction between the central benzene rings and CH···π interactions between the peripheral benzenes and benzylic *endo*-H (Fig. 5g and h), the slipped molecular packing found in **3** gave a right-handed helical form showing π···π and CH···π interactions between the central benzenes and the peripheral pyridine moieties due to electron-deficient character of the pyridine rings.

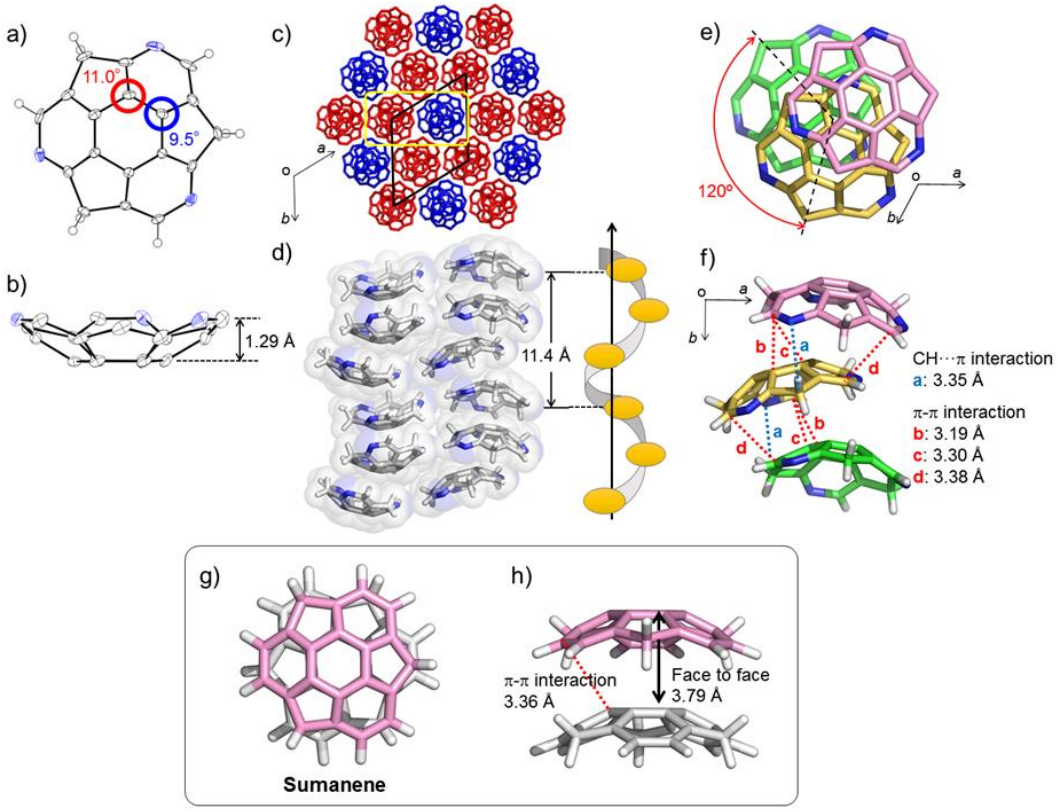

Figure 5. X-ray crystallographic analysis of (*C*)-(–)-**3**. a) Top view, b) side view of ORTEP drawing with 50% probability with POAV angles and bowl depth. c) Packing structure viewed from the *c* axis. The red columns are concave upward and the blue ones are convex upward. Black line indicates the unit cell. The encircled part with yellow line corresponds to the columns shown in d). d) Stick and space-filling model of the right-handed helical columns encircled in c) with one pitch distance. The left side (in downward direction) column: red, the right (in upward direction) column: blue. e) The right-handed helical arrangement of three molecules viewed from the *c* axis, f) CH···π (blue) and π···π (red) interactions within a pitch of the column. Crystal structures of sumanene. g) Top view, and h) face to face distance of the two central benzene rings and π···π (red) interactions in the columnar structures.

The racemic crystal of **3** was prepared by mixing of (*C*)-(–)-**3** and (*A*)-(+)-**3** in 1:1 ratio in CH_2Cl_2, then slow evaporation under N_2 atmosphere. The crystal structure of the prepared racemic compound was observed by synchrotron X-ray crystallographic analysis (Fig. 6). Different from homochiral **3**, the racemic **3** showed unidirectional columnar packing, which was isostructural with that of **1**, in which two enantiomers stacked alternatively along the *c* axis with the same staggered fashion in **1** crystal (Fig. 6c and d). The face-to-face distance of the two central benzene rings in the stacking column was 3.82 Å, which was slightly shorter than in the case of sumanene

(Fig. 6e). Dislike the crystal structure of homochiral (*C*)-(−)-**3**, racemic **3** did not form any CH···π interaction within the column, but between the columns. Instead, four kinds of π···π stacking interactions (3.24~3.35 Å) were formed between the central benzene ring and the peripheral pyridine rings (Fig. 6e). These structural differences among **1**, homochiral (*C*)-(−)-**3** and racemic **3** may derive from the electron-deficient character of the pyridine rings. The pyridine rings favor the formation of π···π interactions with the electron-rich central benzenes and CH···π interactions with the *endo*-H and the electron-rich central benzene rather than the electron-deficient pyridines. This electronic effect of pyridine rings may be cancelled in the stacking column of racemic **3** to exhibit isostructural molecular arrangement with that of **1**.

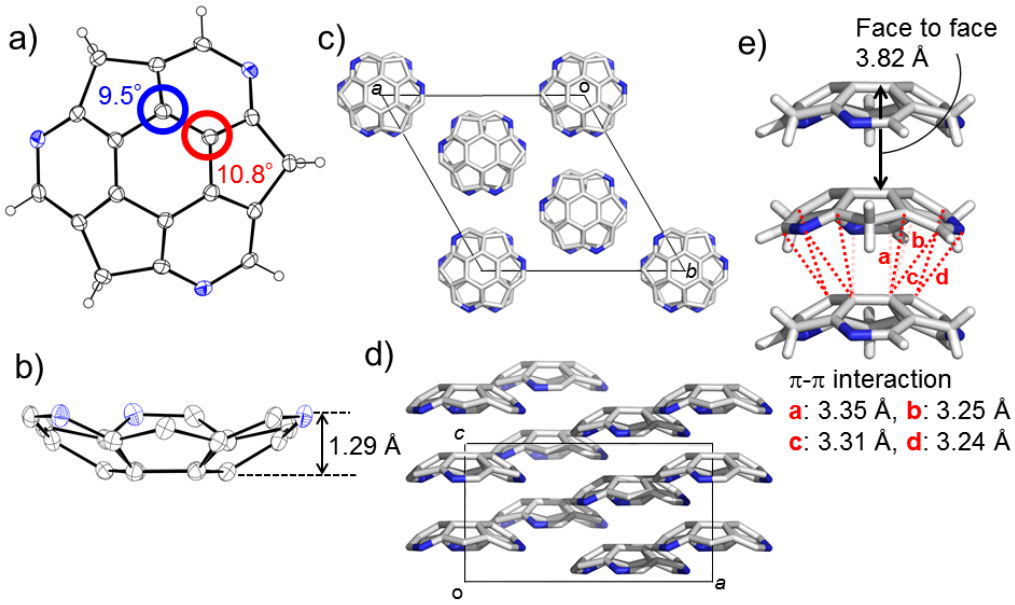

Figure 6. X-ray crystallographic analysis of racemic **3**. a) Top view, b) side view of ORTEP drawing with 50% probability with POAV angles and bowl depth. c) Packing structure viewed from the *c* axis. d) Packing structure viewed from the *b* axis. e) Face to face distance of the two central benzene rings and π-π (red) interactions in the columnar structures.

The chirality of **3** was confirmed by circular dichroism (CD) spectroscopy. The desulfurized product (*C*)-(–)-**3** and (*A*)-(+)-**3**, showed opposite CD spectrum at room temperature, indicating that both products were opposite enantiomers. The CD spectra of **3**, shown in Fig. 7, in conjunction with the X-ray crystal analysis data reveals that the (*C*)-(–)-**3** is the enantiomer pure product prepared from desulfurization of enantiomer pure (*C*)-(–)-**10**, and has chirality stable at room temperature.

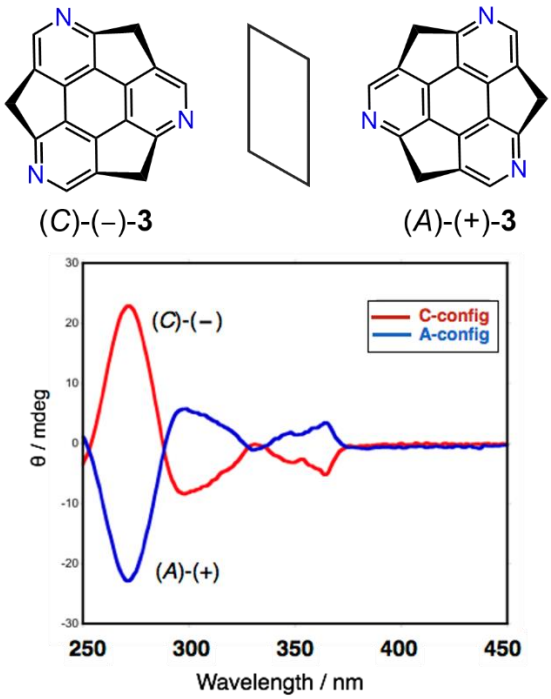

Figure 7. CD spectra of (*C*)-(–)-**3** and (*A*)-(+)-**3** in CH_2Cl_2 at room temperature**.**

1.3 Functionalizations of triazasumanene

In order to tune up the properties of (*C*)-(–)-**3**, modification of (*C*)-(–)-**3** frameworks by functionalization with appropriate groups is faithful way to change their crystal packing pattern, thereby leading to a tailored physical and chemical properties. Various functionalization could be achieved at many positions on triazasumanene skeleton such as at benzylic position, substituents on nitrogen atoms, extended fused-ring and *α*-position on pyridine moieties (Fig. 8).

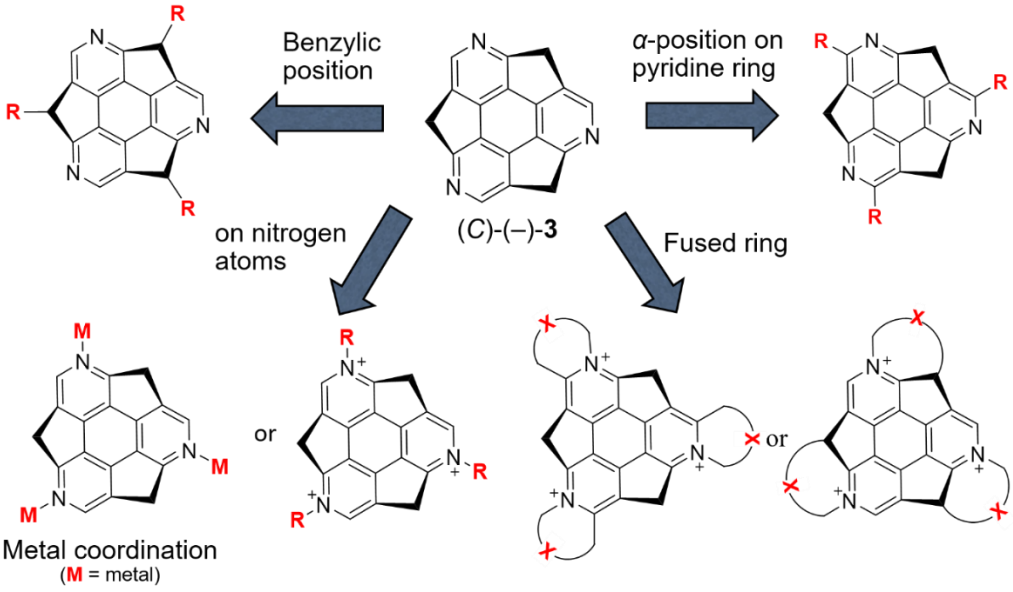

Figure 8. Possible positions of functionalization on (*C*)-(–)-**3** frameworks.

Recently, Sakurai *et al* reported the several transformation reactions at *α*-position of pyridine rings from the precursor (*C*)-(–)-**10**, having *α*-methylthiopyridine moieties, to afford various functionalized triazasumanene derivatives.[23,25] X-ray crystallographic analysis revealed that various kinds of functional groups can significantly change the crystal packing structures including different bowl-depth (Fig. 9). Among them, tris(2-hydroxyphenyl)triazasumanene ((*C*)-(–)-**11**), possesses three intramolecular hydrogen bonds (H-bonds) from pyridine moieties and hydroxyl groups derived from phenols, was found to exhibit fascinating photophysical properties derived from excited state intramolecular proton transfer (ESIPT) coupled with aggregation-induced emission enhancement (AIEE) at the solid state. This photonic properties rarely observe in the buckybowls chemistry because the fluorescence quenching was found in the solid state of pristine buckybowls due to π···π interaction derived from its columnar stacking structures.[25b] In other word, (*C*)-(–)-**11** demonstrated the nitrogen-doped, which acted as H-bonded acceptor, drastically changed the photophysical properties of buckybowls.

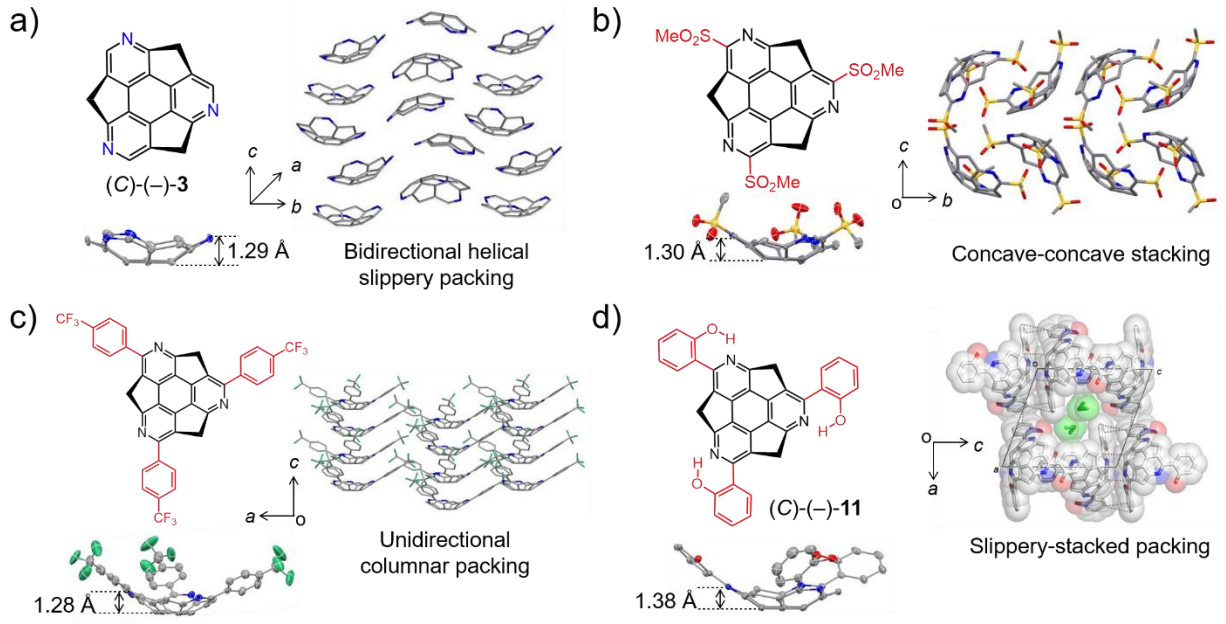

Figure 9. X-ray crystallographic analysis showed the different bowl-depth and crystal packing structures depending on aryl substituents of a) pristine (*C*)-(–)-**3**, b) tris(methanesulfonyl)triazasumanene, c) tris(4-fluoromethylphenyl)triazasumanene, and d) tris(2-hydroxyphenyl)triazasumanene (*C*)-(–)-**11**).

The author paid attention to two precursors from the enantioselective synthesis of (*C*)-(–)-**3** (Scheme 1), the two different types of cyclic triamides (–)-**5** and (–)-**6**. Amide is one of interesting functional groups, which plays an important role to construct the specific structures

through the strong H-bonds via NH···O bonds. Thus, amide units are often utilized as supramolecular synthon enabling directionality and structural stabilization in various supramolecular construction[26] and as binding site for molecular recognition.[27] Unique structural features of (–)-**5**; a cup-shape, and (–)-**6**; a bowl-shape, highly motivated the author to investigate the hidden properties using the their corresponding deprotected cyclic triamides on curved structures, (–)-**12** and (–)-**13**. Author interests to discover how the nitrogen atoms in the formed of amides effect to the different curved structures and apply them as the molecular synthon and/or molecular recognition ability.

1.4 Objectives

The aim of this thesis is to evaluate the various properties from nitrogen-doped effect on C_3 symmetric curved structures by experimental elucidations and theoretical calculation. The content regarding the properties investigation of triazasumanene derivatives and its corresponding cyclic triamides will be covered in this doctoral thesis, which divides to three chapters (Scheme 2). In Chapter 2, the theoretical calculation time-dependent density functional theory (TDDFT) investigation for the analysis of the ESIPT behavior of (*C*)-(–)-**11** is presented. Chapter 3 describes the preparation and physical properties of two different heterocyclic triamides ((–)-**12** and (–)-**13**). Chapter 4 demonstrates the performance of trilactams (–)-**12** for chiral recognition by using an analytical chemistry approach.

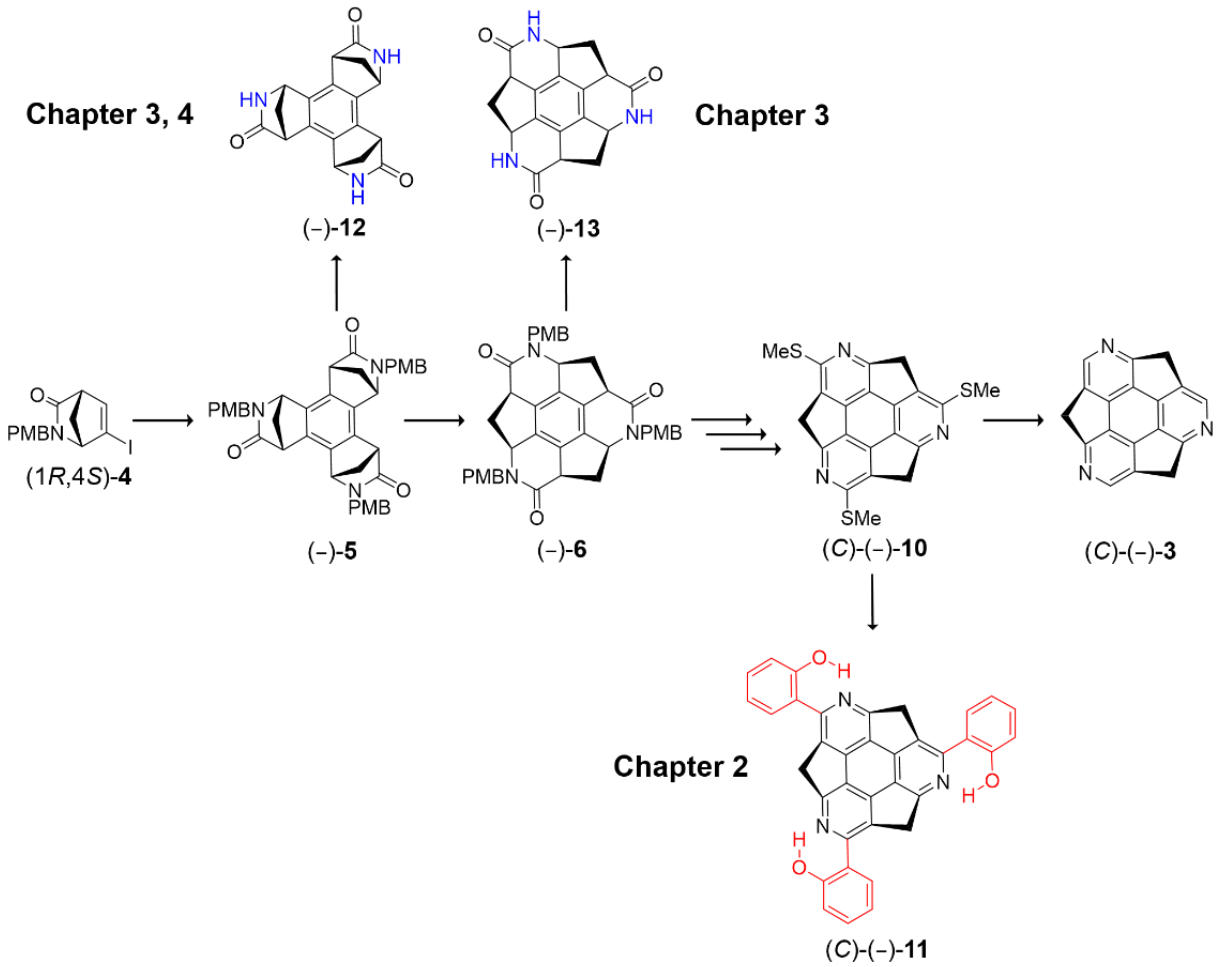

Scheme 2. Summary of this thesis based on the enantioselective synthesis of (*C*)-(–)-**3** and its related heterocyclic triamides.

Chapter 2

Time-Dependent Density Functional Theory Investigation of Excited State Intramolecular Proton Transfer in Tris(2-hydroxyphenyl)triazasumanene

S. Sartyoungkul, M. Ehara, H. Sakurai,

J. Phys. Chem. A, **2020**, *124*, 1227-1234.

Chapter 2: Time-Dependent Density Functional Theory Investigation of Excited State Intramolecular Proton Transfer in Tris(2-hydroxyphenyl)triazasumanene

2.1 Introduction

Proton transfer (PT), which is a crucial reaction in various chemical and biological processes, has been extensively investigated in relevant fields.[28] Excited-state intramolecular proton transfer (ESIPT) process is often observed in the molecules with intramolecular hydrogen bond (H-bond) between proton donor units (e.g., −OH and −NH_2) to proton acceptor units (e.g., −C=O and −C=N). In the process, the molecules initially get energized to excited state, then the photoexcited molecules transfer protons via tautomerization, usually from enol → keto or imine → enamine.[29] This process occurs on an ultrafast time scale (i.e., sub-picoseconds) and generates a large Stokes shift of 6000–12000 cm^{-1} in the emission spectra, resulting from the relaxation from lower energy of the excited tautomer form (Scheme 3).[30] ESIPT-active compounds has highly attracted investigated and transformed into various potential applications in optoelectronic devices such as organic-light emitting diodes,[31] fluorescence biosensors[32] and electroluminescence materials.[33] Therefore, finding novel motives of ESIPT-active molecules has continuously been expected.

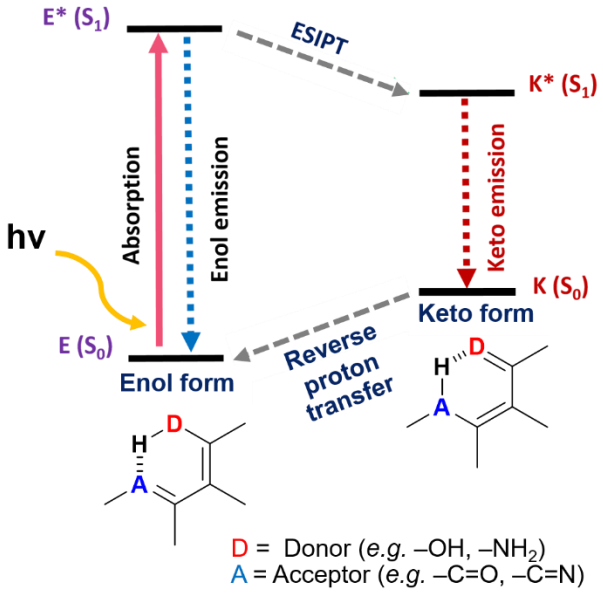

Scheme 3. General ESIPT photocycle process.

Plenty of experimental and theoretical studies for ESIPT have been investigated from the viewpoint of the reaction process, the effect of solvent, the electronic effect, and the role of the H-bond interaction.[33-34] These studies elucidated that H···O or H···N type H-bond interactions is crucial for the dynamic ESIPT process, and stronger H-bonded interaction in excited state provides the red shift, while weaker H-bond results in the blue shift in emission spectra, respectively.[35] Hence, the geometrical proximity between proton donor and acceptor units intramolecularly is required for the effective ESIPT process. However, ESIPT is a quite susceptible process; highly dependent on the external conditions such as the solvents and temperature, as well as the intrinsic natures of the compounds including the strength of H-bond.[36] In particular, the ESIPT in the solid and the solution states are different, so that the comprehensive computational study is highly demanded for the effective design of ESIPT molecules.[32b,34a,37] Time-dependent density functional theory (TDDFT) is a suitable computational method for more in-depth understanding of the mechanistic detail and electronic effect of ESIPT process.[38] Recently, the mechanistic details and electronic effects of multiple excited PT process by TDDFT were highly studied, nevertheless, the reports on the intramolecular dynamic processes are still few.[39] Pradhan *et al* reported the TDDFT calculations of the mechanistic excited-state dual PT via enolization of diformyl-dipyrromethanes through stepwise process influenced by the substituents.[39b] Another TDDFT calculations from Zhao *et al* revealed that the excited state double proton transfer (ESDPT) mechanism of pigment alkannin involved a stepwise process, where a polar aprotic solvent affected the first PT step.[39c]

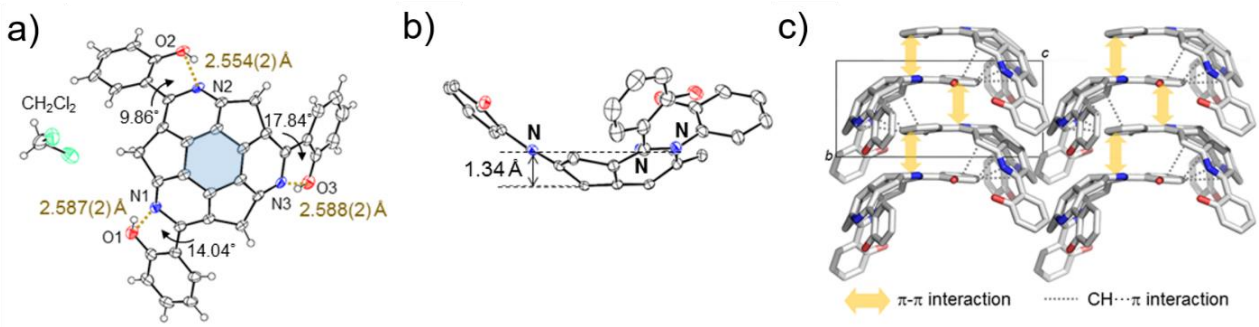

Figure 10. Crystal structure of (*C*)-(–)-**11**. a) ORTEP model showing the intramolecular H-bonds and dihedral angles φ. b) Deepest position of the bowl depth. c) Stacking structure viewed from the *b* axis with the intermolecular CH···π (grey dotted line) and π···π (yellow solid arrow) interactions.

As the author mentioned in the Chapter 1, one of the triazasumanene derivative, tris(2-hydroxyphenyl)triazasumanene ((*C*)-(–)-**11**), forms three intramolecular OH···N type H-bonds, exhibited ESIPT coupled with AIEE properties, which is rarely observed in buckybowl chemistry.[25] Crystal analysis revealed that the unusual shorten H-bonded length O···N distances between the phenol hydroxyl group and the nitrogen atom on the peripheral pyridine of (2.554(2) −2.588(2) Å), coupled with a small twist of the phenolic rings with respect to the pyridine moieties is observed at dihedral angles (φ) of 9.86°, 14.04° and 17.84° (average φ = 14.0°). These different φ resulted from the intermolecular CH···π and π···π interactions with the nearby molecules in a slippery-stacked columnar structure (Fig. 10). This nearly co-planar and strong six-membered ring type H-bonding geometry, which is similar to the ESIPT-active 2-(2'-hydroxyphenyl)pyridine (HPP) molecule.[40] LeGourriérec *et al* reported that the ESIPT of HPP was observed around 500 nm at 77 K in non-polar media,[40a] which contributed to the non-radiative decay by twisting motion and nπ* deactivation.[40b] Hence, (*C*)-(–)-**11** would permits the facile PT from donor hydroxyl groups to the proximal nitrogen acceptor via ESIPT dynamic process.

In the experiment, (*C*)-(–)-**11** exhibited dual emission spectra in the solid state (Fig. 13b, blue), among them, the latter peak revealed a large Stokes shift from the ESIPT property due to photoinduced enol-keto tautomerization of phenolic rings. However, the same phenomenon was not observed in the solution state even in the presence of a non-polar aprotic solvent (e.g., dichloromethane (CH_2Cl_2) solution) (Fig. 13b, red), in which significant intramolecular hydrogen bonding interactions might be expected. In this Chapter, to obtain more insights into the mechanistic process involving the contribution of the three OH···N H-bonds to the ESIPT of (*C*)-(–)-**11**, namely, stepwise or concerted processes, TDDFT calculations were performed and compared with experimental observation. The involved species of (*C*)-(–)-**11** for photoinduced ESIPT are considered as followed; EEE, KEE, KKE and KKK refer to trienol, monoketo, diketo, and triketo forms, respectively (Fig. 11).

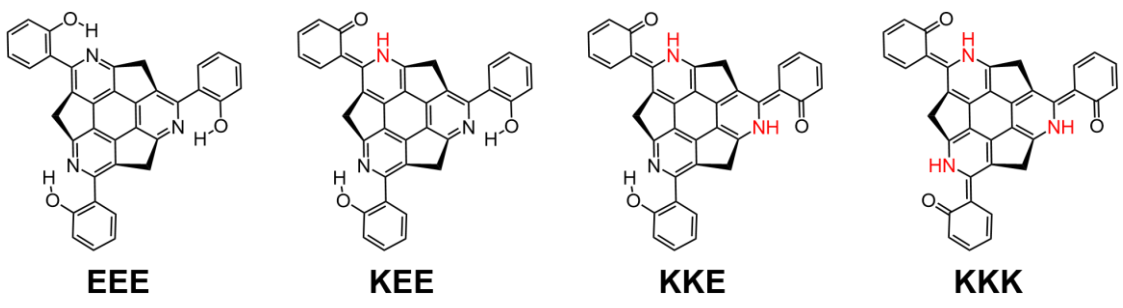

Figure 11. Molecular species of (*C*)-(–)-**11** considered in this work.

2.2 Results and discussion

2.2.1 Optimized Geometric Structures, Electronic Spectra and Frontier Molecular Orbitals

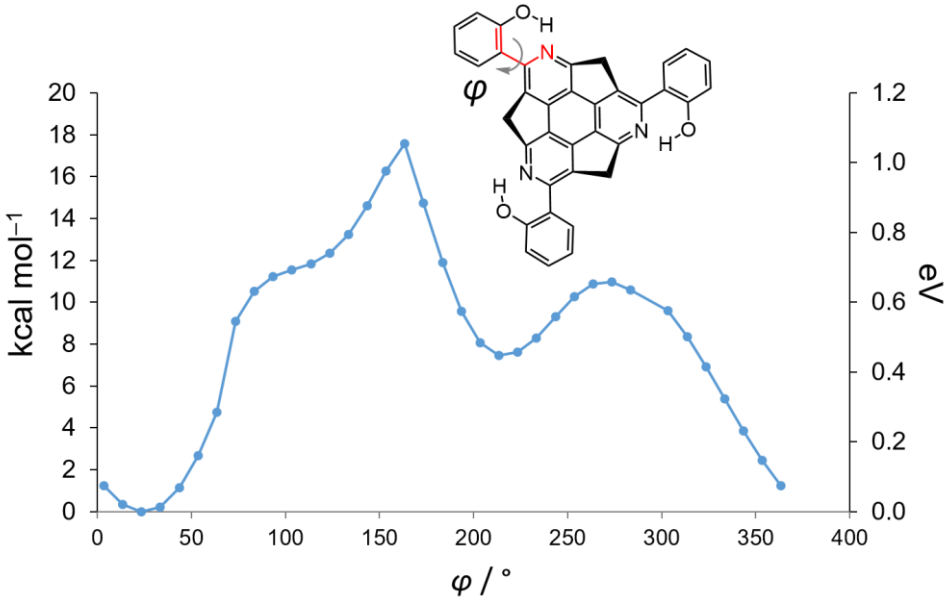

Figure 12. The potential energy curve of (*C*)-(–)-**11** along the dihedral angle φ of one from phenyl ring against peripheral pyridine of triazasumanene of S_0−EEE simulated at CAM-B3LYP/6-31+G(d,p) level revealed small twisting dihedral angle φ provided the most stable ground state of (*C*)-(–)-**11** conformation.

The optimized EEE structure in the S_0 state revealed a non-planar structure with dihedral angle φ of 9.66°, 13.60° and 13.62° (average dihedral angle φ = 12.3°) for the phenol-pyridine planes and an average O···N distance of 2.597 Å. This result indicated that (*C*)-(–)-**11** exhibits a non-symmetric C_1 structure, which is similar to previously reported single-crystal analysis data.[25] The potential energy curve of S_0−EEE along the dihedral angle φ was calculated (Fig. 12), which shows that the energy variation is relatively large and the small dihedral angle affords the most stable conformation in the ground state due to the stabilization of intramolecular H-bonds between −OH phenolic and N from pyridine moieties.

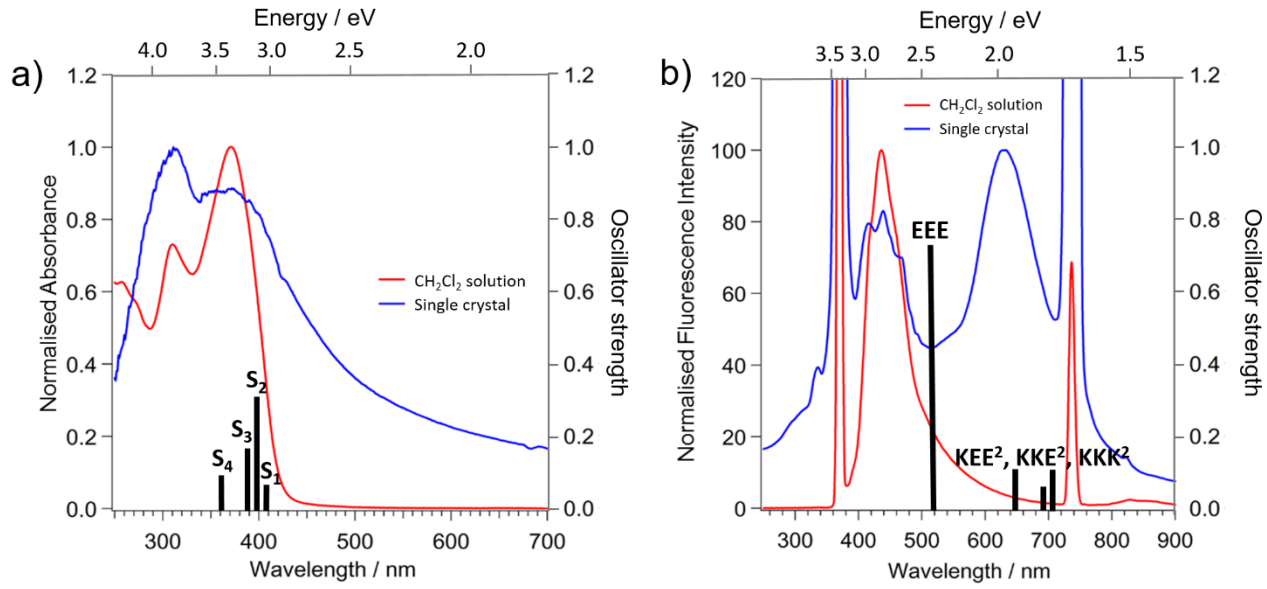

Figure 13. Room temperature a) absorption and b) emission spectra of (*C*)-(–)-**11**. Red: 4×10^{-5} M CH_2Cl_2 solution. Blue: single crystalline solid. λ_{ex} = 370 nm.[25] Black solid arrows: transitions calculated for (*C*)-(–)-**11** at B3LYP/6-31+G(d,p) level. The length of each arrow is proportional to the calculated oscillator strength. Superscript 2: the second electronic transition. For the first electronic transitions of PT species (KEE, KKE and KKK) are all located in the infrared region (>1000 nm).

With respect to the photophysical properties, the absorption and emission spectra of the four different structures (Fig. 11) were calculated and compared with the experimental results. In the preliminary TDDFT calculations, large underestimation of the emission energies was obtained using B3LYP (Fig. 13), while reasonable results were obtained using CAM-B3LYP for interpreting the UV-Vis absorption and emission spectra (Fig. 14). Hence, for the further investigation of the ESIPT process of (*C*)-(–)-**11**, CAM-B3LYP was adopted.

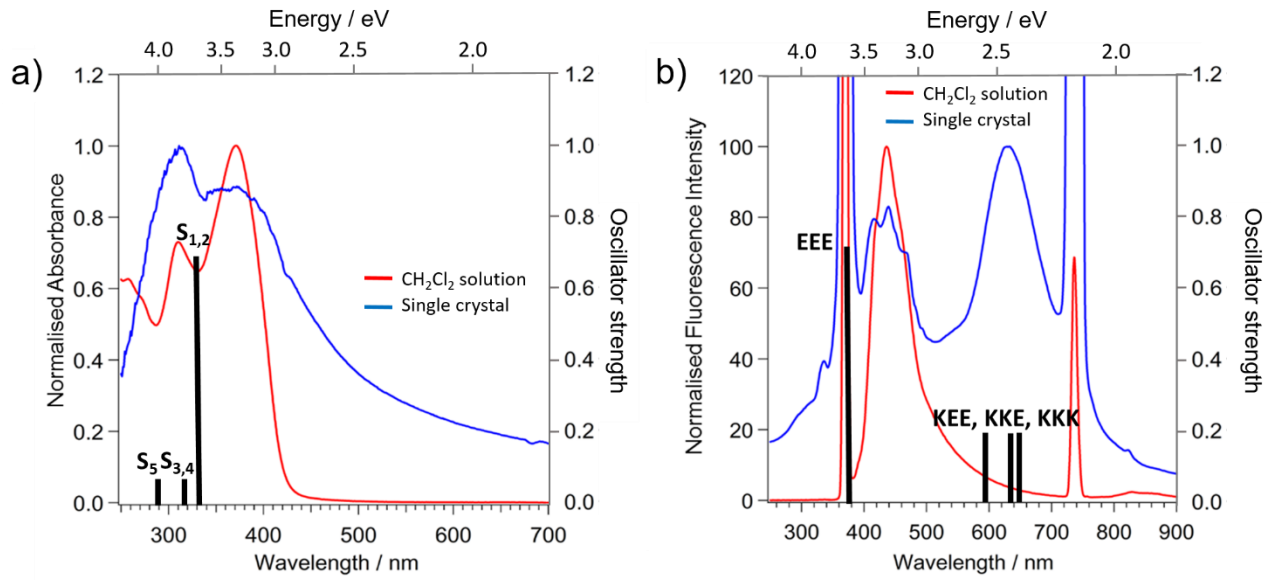

Figure 14. a) Absorption and b) emission spectra of (*C*)-(–)-**11** at room temperature (Red: in CH_2Cl_2 solution of 4×10^{-5} M CH_2Cl_2 solution, Blue: single crystalline solid. (λ_{ex} = 370 nm)[25] plotted with the spectra calculated by the CAM-B3LYP/6-31+G(d,p) level. The length of the bars corresponds to the calculated oscillator strength.

In general, the charge distribution over the molecules is known to play an important role in ESIPT.[34b,39d,39g] The frontier molecular orbitals (MOs) of EEE in the S_0 state were analyzed to investigate the excited-state characteristics for the promotion of ESIPT. The highest occupied molecular orbital (HOMO) was predominantly localized on the oxygen atom of phenol ring, while the lowest unoccupied molecular orbital (LUMO) was located on the nitrogen atom of the pyridine moiety and triazasumanene skeleton (Fig. 15), indicating that the charge distribution around H-bonded moieties is relevant for ESIPT. The energy gab between HOMO-LUMO was found at 0.22 eV. The low-lying five excited states of EEE were examined and the lowest two excited states were nearly degenerated (Table 1). Clearly, the S_0–S_1 transition was assigned as the HOMO-LUMO transition, and it afforded a large oscillator strength, which was responsible for the photoabsorption to promote ESIPT.

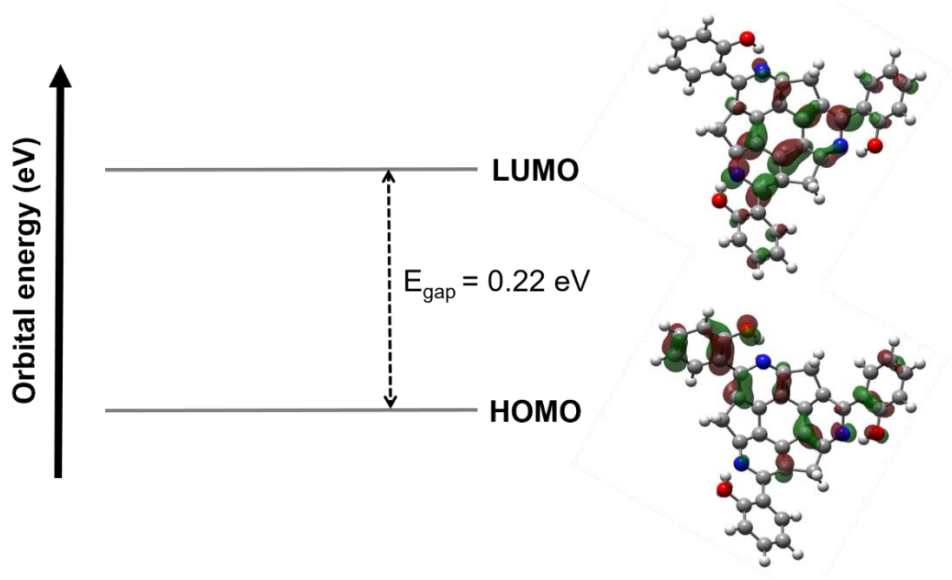

Figure 15. View of HOMO and LUMO orbitals of (*C*)-(–)-**11** calculated by CAM-B3LYP/6-31+G(d,p) level (isovalue = 0.04) with energy gap of 0.22 eV.

Table 1. Absorption wavelength (λ_{abs}), transition energy (ΔE_{abs}), corresponding oscillator strength (*f*) and main configurations of the low-lying excited states of EEE calculated by TDDFT with CAM-B3LYP/6-31+G(d,p), based on the optimized ground state geometry.

Transition state	λ_{abs} (nm)	ΔE_{abs} (eV)	*f*	Transition character
$S_0 \rightarrow S_1$	333	3.72	0.7249	HOMO → LUMO
$S_0 \rightarrow S_2$	333	3.72	0.7253	HOMO → LUMO
$S_0 \rightarrow S_3$	328	3.78	0.0637	HOMO → LUMO
$S_0 \rightarrow S_4$	324	3.82	0.0748	HOMO → LUMO
$S_0 \rightarrow S_5$	294	4.21	0.0230	HOMO → LUMO + 1

2.2.2 Vertical emission energies, adiabatic energies and ESIPT energy diagram

Due to the three unique intramolecular hydrogen bonds present in (*C*)-(–)-**11**, several ways of ESIPT processes are possible, namely, PT pathways by stepwise or simultaneous double and/or triple PT. Hence, various intermediates are possibly generated in the excited-state levels (Fig. 16). First, the optimized EEE, KEE, KKE and KKK structures in the S_1 state were considered and the vertical emission energies of $S_1 \rightarrow S_0$ transition were analyzed. The corresponding results are shown in Fig. 17.

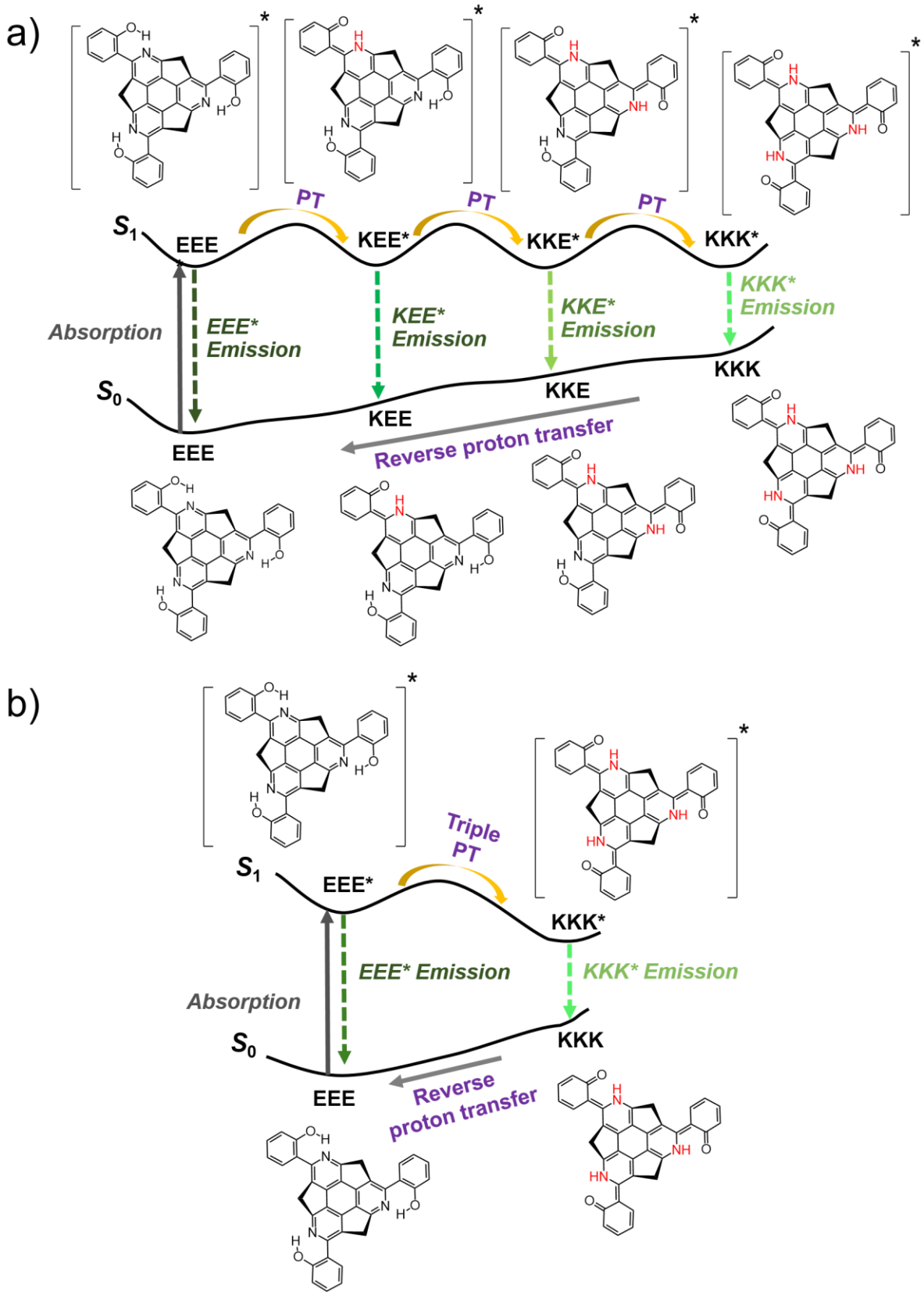

Figure 16. Two proposed ESIPT mechanistic process of intramolecular three protons transfer in (*C*)-(–)-**11**. a) Stepwise proton transfer and b) simultaneous triple proton transfer.

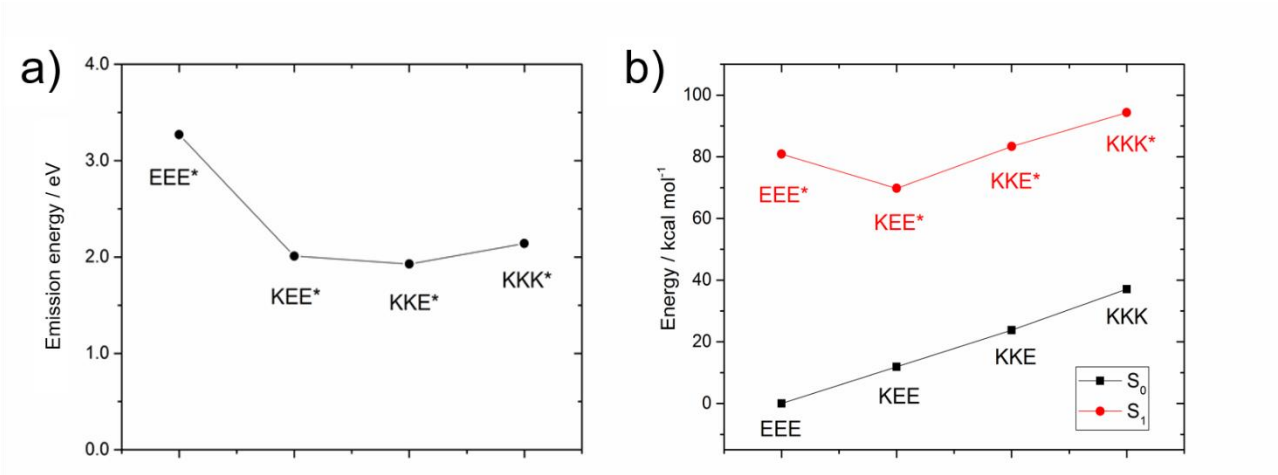

Figure 17. a) Vertical emission energies ($S_1 \rightarrow S_0$ transition) of enol forms. b) Adiabatic energies of the S_0 (black line) and S_1 (red line) states. Asterisk denotes the S_1 state in each structure.

The calculated strong emission peak of EEE was observed at 3.27 eV (378 nm) (Fig. 17a), indicating that the experimental fluorescence at 2.77 eV (447 nm) (Fig. 14) corresponds to the emission from the S_1−EEE structure. Notably, the calculated vertical emission energies of all three keto forms, (KEE, KKE, and KKK) are almost similar values (c.a., 1.93–2.15 eV, 577–643 nm) (Fig. 17a, Table 2 and 3). DFT calculations revealed that the experimental emission peak observed at 621 nm (Fig. 14) with a large Stokes shift could correspond to the emission from any of these excited keto species. Therefore, we could not distinguish either a stepwise or a concerted process involved in the ESIPT of (*C*)-(–)-**11** only from the results of the vertical emission energy. In other words, photoexcited S_1−EEE molecule transfers the protons accompanied by tautomerization to reach either KEE, KKE or KKK via concerted or stepwise ESIPT mechanisms (Fig. 16). Then, the adiabatic energies of these four species in the S_0 and S_1 states were evaluated (Fig. 17b). From the result, the S_1−KEE was the most energetically stable compared with other excited keto intermediates, for instance, it is stable by 0.44 eV relative to S_1−EEE. Notably, the single PT of S_1−KEE at the phenol ring with dihedral angle φ = 9.66° afforded more energetically stable structure compared to that at the other phenol ring with φ (13.6°) due to the nearly planar structure around hydrogen bond. The PT energy profile of the S_1 state from EEE to KEE with dihedral angle φ being fixed is slightly downhill and nearly barrierless as shown later. These results indicated that after photoinduced absorption, (*C*)-(–)-**11** readily undergoes single PT from S_1−EEE to more energetically stable S_1−KEE. Although simultaneous double or triple PT from S_1−EEE to reach S_1−KKE or S_1−KKK possibly happen, the higher PT energy barriers should exist due to the energetically unstable nature of these two keto species. On the other hand, S_0−EEE was found to be the most stable structure because three-fold intramolecular H-bonds stabilize the structure. As

the number of transferred protons increases, the S_0−keto forms become unstable (Fig. 17b). Noteworthy, the total energy of all keto species in S_0 and S_1 showed the same trend: KEE < KKE < KKK (Fig. 17b). The energetically unstable nature of keto species at S_0 and S_1 states is attributed to the destabilization of the keto tautomer from cyclohexadienone structure after PT, which leads to the loss of stabilization energy of π-conjugation as well as the greater rings strain due to tautomerization.[41] Moreover, the energy required for bond alternation due to enol-keto tautomerization at phenol ring moieties enhances due to the increasing number of PT processes.

Table 2. Optimized energy (a.u.), emission wavelength (λ_{emi}), transition energy (eV), corresponding oscillator strength (*f*), HOMO (eV), LUMO (eV) and HOMO-LUMO energy gap (eV) of the S_1 state of (*C*)-(–)-**11** calculated by TDDFT with CAM-B3LYP/6-31+G(d,p) level (solid state).

S_1-Excited form	Optimized energy (a.u.)	λ_{em} (nm)	Transition energy (eV)	*f*	HOMO (eV)	LUMO (eV)	E_{gap} (eV)
EEE	−1773.44795867	378	3.27	0.667	−7.27	−1.73	5.54
KEE	−1773.46423914	616	2.01	0.144	−6.17	−2.23	3.94
KKE	−1773.44188272	643	1.93	0.161	−6.24	−2.39	3.85
KKK	−1773.42513271	577	2.15	0.207	−6.45	−2.38	4.07

Table 3. Optimized energy (a.u.), emission wavelength (λ_{emi}), transition energy (eV), corresponding oscillator strength (*f*), HOMO (eV), LUMO (eV) and HOMO-LUMO energy gap (eV) of the S_1 state of (*C*)-(–)-**11** calculated by TDDFT with CAM-B3LYP/6-31+G(d,p) level with polarizable continuum model (PCM) of CH_2Cl_2 (solution state).

S_1-Excited form	Optimized energy (a.u.)	λ_{em} (nm)	Transition energy (eV)	*f*	HOMO (eV)	LUMO (eV)	E_{gap} (eV)
EEE	−1773.46770372	407	3.04	1.053	−7.16	−1.64	5.52
KEE	−1773.51482930	506	2.45	0.660	−6.41	−1.67	4.74
KKE	−1773.46495370	527	2.35	0.649	−6.60	−2.03	4.57
KKK	−1773.45480724	502	2.47	0.838	−6.70	−2.00	4.70

From the above result, the predominant ESIPT process of (*C*)-(–)-**11** observed as dual emission was concluded as a single PT process (Fig 18). Starting from the most stable S_0−EEE in the system, photo-absorption leads to two possible radiative processes. First, the relaxation of S_1−EEE affords an enol emission at 378 nm (3.30 eV). Another pathway is that, single ESIPT occurs at the most co-planar conformation with dihedral angle φ = 9.66° to reach more energetically favorable S_1−KEE state, and the emission with a larger Stokes shift from

corresponding keto form is observed at 621 nm (2.00 eV). Because of the barrierless nature of single PT, more energetically stable S_1–KEE readily generates via extremely fast ESIPT in the sub-picosecond time scale. Finally, the reverse PT happens in the ground state from S_0–KEE to S_0–EEE, hence, completes the ESIPT cycle of (*C*)-(–)-**11**. Moreover, the similar trend of the adiabatic energies for enol-keto species at the S_0 and S_1 states was confirmed by the PCM-TDDFT calculations in CH_2Cl_2. The main ESIPT contribution for the $S_0 \rightarrow S_1$ transition was a ππ*-type transition. The TDDFT calculation results for the photophysical properties of (*C*)-(–)-**11** in the solid state and CH_2Cl_2 solution, respectively, are summarized in Tables 2 and 3. Some H-bonded parameters from optimized DFT geometries of EEE and KEE species in S_0 and S_1 states are reported in Table 4.

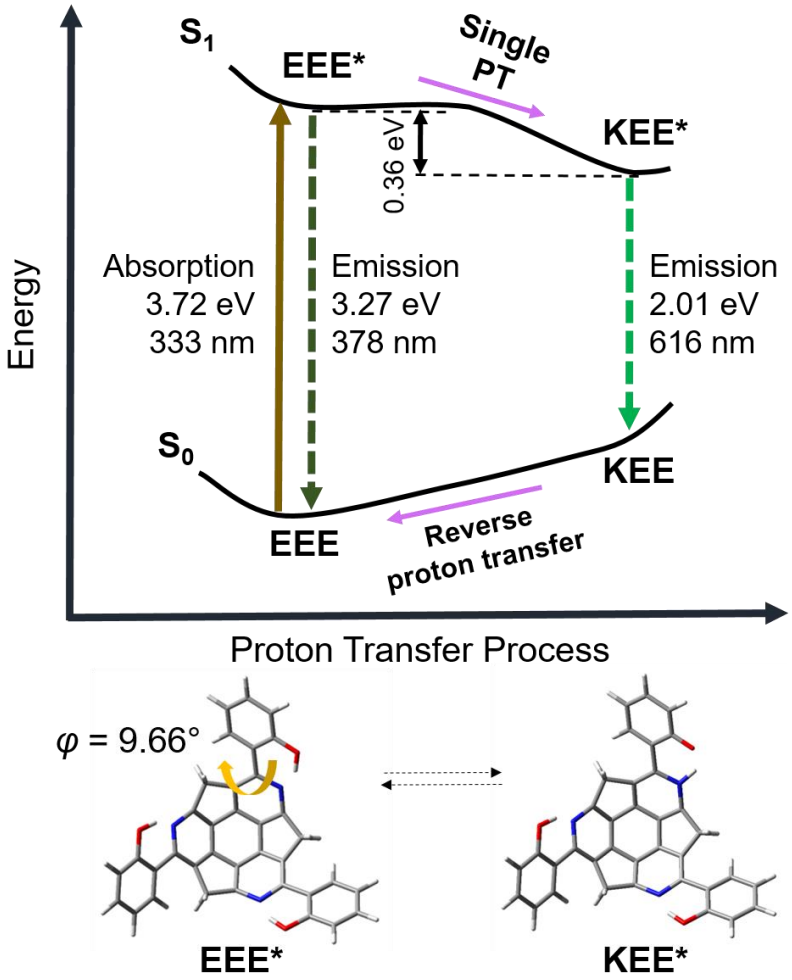

Figure 18. Energy diagram of ESIPT in (*C*)-(–)-**11**, confirming that single PT is the predominant process and the PT happened at co-planar $\varphi = 9.66°$.

Table 4. Bond length (Å) and torsion angles φ (°) of optimized (*C*)-(–)-**11** geometries of EEE and KEE at S_0 and S_1 states calculated by TDDFT with CAM-B3LYP/6-31+G(d,p)

Parameters	S_0−EEE			S_1−EEE			S_0−KEE			S_1−KEE		
	OH-1	OH-2	OH-3	OH-1	OH-2	OH-3	OH-1	OH-2	OH-3	OH-1	OH-2	OH-3
$d_{O–H}$ (Å)	0.99	0.99	0.99	0.99	0.99	0.99	1.50	0.99	0.99	1.72	0.99	0.99
$d_{O\cdots N}$ (Å)	2.59	2.59	2.59	2.53	2.59	2.58	2.45	2.60	2.59	2.62	2.59	2.60
$d_{N\cdots H}$ (Å)	1.70	1.70	1.70	1.62	1.69	1.67	1.03	1.70	1.70	1.03	1.69	1.68
φ (°)	9.66	13.62	11.80	9.92	13.21	13.44	7.48	15.94	15.21	16.30	12.64	12.97

[a]transfer proton at single ESIPT occurred at OH-1 moiety.

2.2.3 Potential energy curve (PEC) scan from EEE* to KEE* along the N-H bond and T_1/S_0 minimum energy crossing point (MECP)

As mentioned in the introduction, the large Stokes shift from ESIPT in (*C*)-(–)-**11** was observed in the crystalline state, but scarce in a non-polar solution, which can be explained by non-radiative decay from conical intersection (CI).[42] Theoretical interpretation using the CI model by state-averaged complete active space self-consistent field (CASSCF) method has been widely accepted to explain radiationless decay in the excited states. The calculated results showed that twisted geometries at inter-ring bond leading to the proximity in energy (crossing point) between the S_1 (minimum energy) and S_0 states (maximum energy) of keto forms at a twisting φ between the proton donor and acceptor units around 90°. Under the conditions, CI directly or indirectly acts as an efficient decay channel from the excited state to ground state. Several studies reveals the significance of CIs for an ESIPT property to explain the radiationless decay at the keto form of several luminescent compounds.[35,43] In contrast, luminescent compounds in the solid state is mainly related to the prohibition of radiationless decay via CI by maintaining φ constant at or near the coplanar structure. Several authors have reported weak fluorescence of HPP,[40] with a structure and a behavior similar to those of the ESIPT-active moiety in (*C*)-(–)-**11**, resulting from efficient non-radiative decay together with the inter-ring twisting motion. Therefore, the similar explanation might be reasonable for the non-radiative decay of (*C*)-(–)-**11** for the weak emission in the solution state.

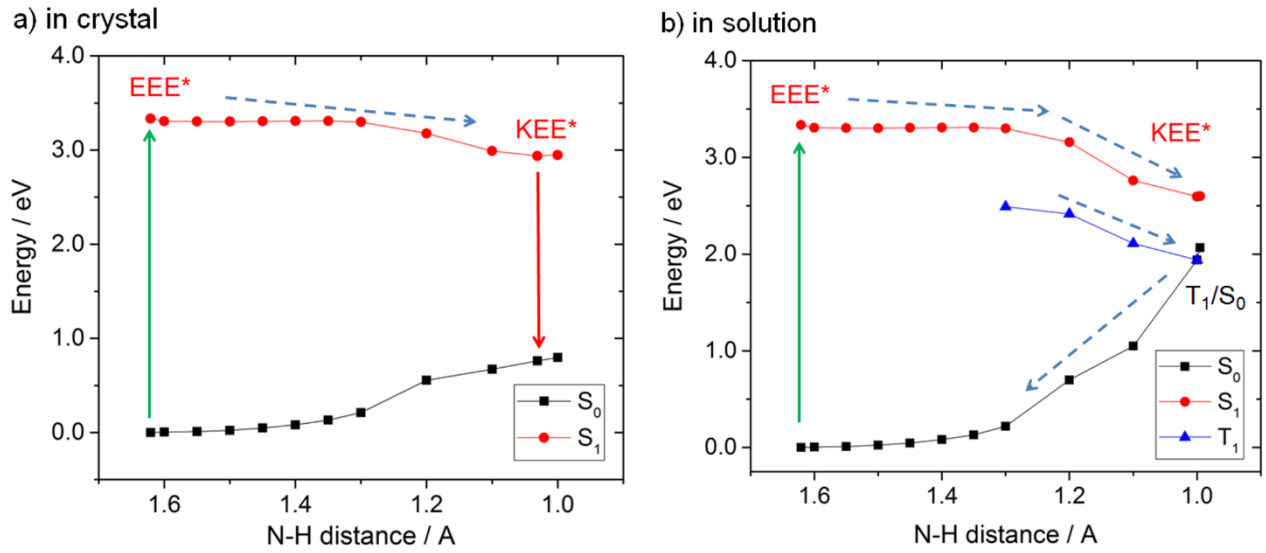

Figure 19. The potential energy surfaces (PESs) of the radiative and non-radiative decay pathways of (*C*)-(–)-**11** in crystal and solution environments, respectively, calculated by the DFT partial optimization. a) In crystal, the dihedral angle φ was fixed at 9.9° and all the other coordinates were optimized for the S_1 state and the geometries of the S_0 state were taken as the same as the S_1 state. b) In solution, the S_1 and T_1 states were optimized for each state without restricting the dihedral angle φ and the geometries of the S_0 state were taken as the same as the S_1 state except for T_1/S_0 MECP.

To analyze the radiative or non-radiative decay routes for ESIPT of (*C*)-(–)-**11** more clearly, the calculations of potential energy surfaces by partial optimization have been carried out for the pathway in crystal and solution environments, respectively. In the crystal environment, it was assumed that the dihedral angle φ does not change due to the restriction of the stacking structure of triazasumanene moiety. Then, the potential energy curve (PEC) of the S_1 state along the PT process from EEE to KEE does not stabilize much as shown in Fig. 19a (plotted along N-H distance); the PEC is slightly downhill with very low energy barrier of 0.006 eV at around N-H distance of 1.40 Å. This means that the non-radiative decay is prohibited in crystal and the photoemission occurs from S_1–KEE. In solution, on the other hand, the S_1 state significantly stabilizes along the PT process, but, with tiny energy barrier of 0.006 eV as shown in Fig. 19b and the non-radiative decay becomes possible, which was also suggested in similar systems previously.[35] In this case, dihedral angle φ can relax and is 97° at the minimum energy point of S_1–KEE by the DFT calculations. However, the precise calculation to locate CI was too difficult in the present system and beyond the scope of this work because the size of (*C*)-(–)-**11** is too large to perform the multi-reference wavefunction theory calculations like CASSCF or CASPT2.

Another non-radiative relaxation via minimum energy crossing point (MECP) of T_1/S_0 is also possible, which is shown in Figure 19b. The T_1/S_0 MECP was located using the Harvey's method[44] and the calculated dihedral angle φ at T_1/S_0 MECP was 123°. Note that this pathway is also prohibited in the case of crystal environment. The approximate non-radiative decay pathways in solution and the structures of KEE* and MEXP of T_1/S_0 were illustrated in Fig. 20. In the potential energy curves, the S_1 and T_1 states were optimized for each state without restricting the dihedral angle φ and the geometries of the S_0 state were taken as the same as the S_1 state except for T_1/S_0 MECP. Decay pathways showing with dotted lines were not precisely calculated because of the limitation of the computational method. The bond length of NH was 1.000 and 1.001 Å for the energy minimum of S_1 and MECP and the energies are 2.595 and 2.291 eV, respectively, relative to the ground state.

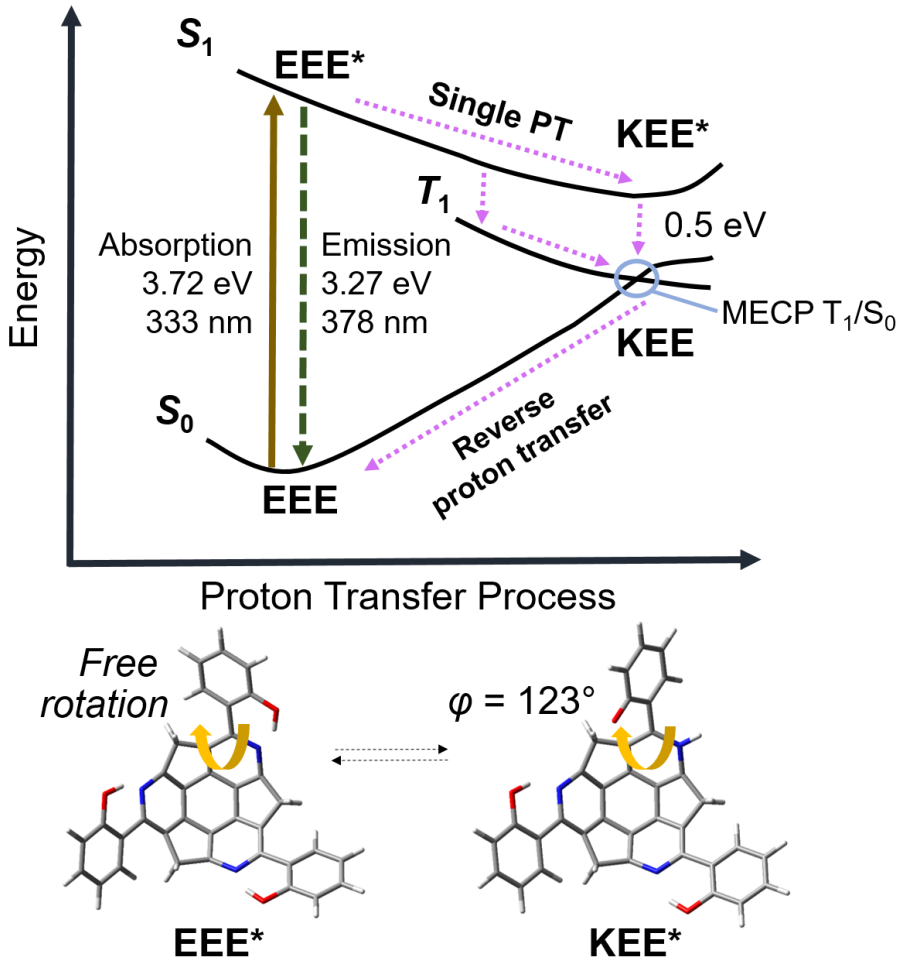

Figure 20. Approximate non-radiative decay pathways in solution (purple dotted lines) and the structures of KEE* relaxed at MECP of T_1/S_0 φ = 123° followed by Harvey's method.[44]

2.3 Conclusion

The mechanism of the ESIPT process of (*C*)-(–)-**11** is investigated by the TDDFT calculations. Intramolecular single PT is found to be the predominant pathway in the (*C*)-(–)-**11** molecule due to the energetically favorable mono-keto form in the first excited state as well as the low PT barrier. There is no significant difference in the calculated vertical emission energies among the single, double, and triple PT states. Dual emission in the solid states is predominantly related to the emissions from S_1–EEE and S_1–KEE, while emission from S_1–KEE is restricted in the solution. The reason for the silence of ESIPT in the solution state might originate from the adiabatic radiationless decay due to twisting motion of the 2-hydroxyphenyl ring in excited state either through CI or T_1/S_0 MECP pathways. Since (*C*)-(–)-**11** composed of three HPP units on aromatic nitrogen-doped bowl-shaped structure, it exhibited slightly larger redshift ($\Delta \sim 110$ cm^{-1} in non-polar aprotic solvent) over a simple HPP molecule due to larger π-conjugated aromatic contribution after photoinduced tautomerization.

2.4 Computational methods

Density functional theory (DFT) calculations were performed for characterizing the electronic structures of (*C*)-(–)-**11** in the ground and excited states. First, B3LYP[45] method was preliminary conducted to compare with the experiment emission energies results; then the long-range correction CAM-B3LYP[46]/6-31+G(d,p)[47] level of theory was adopted in all calculations because of the presence of heteroatoms in (*C*)-(–)-**11** The ESIPT processes were characterized as charge reorganization in the excited state. The ground-state (S_0) geometries were optimized for the four forms (EEE, KEE, KKE, and KKK,) of PT states in the gas phase. The geometry optimization of the first excited state (S_1), the oscillator strength of which was sufficient for photoemission, was carried out by TDDFT. Vertical absorption and emission energies of these species were calculated by TDDFT in solution. Solvent effects were considered using the polarizable continuum model (PCM)[48] for dichloromethane (CH_2Cl_2), which was used in the measurement of the experimental UV-Vis spectrum. A linear response scheme with non-equilibrium solvation was adopted in the PCM-TDDFT calculations. The local minima of each structure both in the ground and excited states were confirmed without imaginary vibrational frequencies. The energy profile of the S_0 state of EEE as a function of the dihedral angle (φ) between the 2-hydroxyphenyl and peripheral pyridine rings of the triazasumanene skeleton were evaluated by the partial optimization, in which dihedral angle φ was fixed with all the other coordinates optimized. The energy profiles of the ESIPT for the radiative and non–radiative pathways between EEE and KEE were also calculated by the partial optimization assuming in crystal and solution environments, respectively. The detailed computational condition will be discussed later. All calculations were performed with the Gaussian09 B01 suite of program.[49] Zero-point energy correction was considered for calculations of vertical and adiabatic transition energies.

Chapter 3

Synthesis and Dimerization Properties of Cup- and Bowl-shaped Cyclic Trilactams

S. Sartyoungkul, Y. Yakiyama, H. Sakurai,

Asian J. Org. Chem., **2020**, *9*, 947-952.

Chapter 3: Synthesis and Dimerization Properties of Cup- and Bowl-shaped Cyclic Trilactams

3.1 Introduction

Amides are often observed in natural products and medicines and are also the important structural motifs in terms of molecular recognition by hydrogen bond (H-bond) as represented by the secondary structures of proteins and double helices in DNA (Fig. 21).[50] Furthermore, due to the contribution of the lone pair on N atoms to the conjugation with carbonyl oxygen (Scheme 4), C–N bond in amide structure has high stability toward various reaction conditions.[51] These features of amide are often utilized as a supramolecular synthon,[52] realizing the binding of the components by hydrogen bond with high directionally to give supramolecular structures.[26]

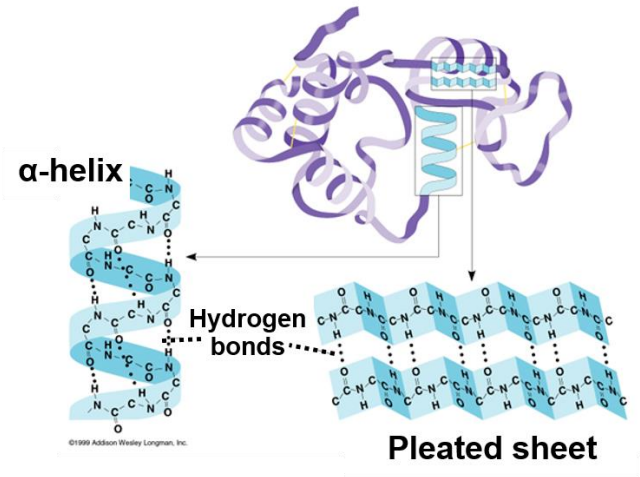

Figure 21. Hydrogen bonding property of amide in structures of *α*–helix and pleated sheet of proteins.

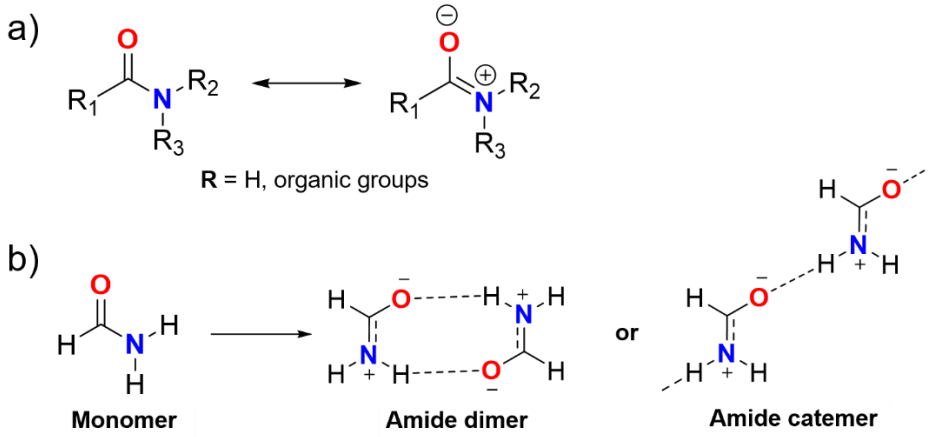

Scheme 4. Molecular structure of amide. a) Resonance structures of amide and b) mode of H-bonding interactions found in amides.

Multiple cyclic amides can be obtained by synthetic approach in laboratory and their several properties are investigated. Still *et al* reported chiral C_3-symmetric multiple cyclic amides compounds and demonstrated the reversible binding of peptides by H-bonding interactions (Fig. 22a).[53] Chiral C_3-symmetric bowl-shaped cyclic triamides bearing hydrogen-bonding ability reported by Azumaya *et al* showed chiral capsule-type dimer via H-bonds in solid state (Fig. 22b).[54d]

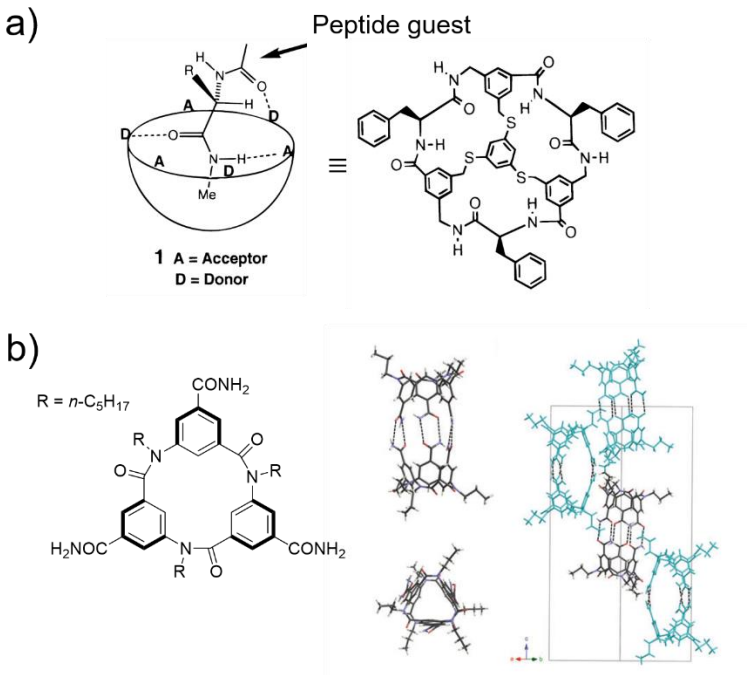

Figure 22. Some examples of synthetic *C*3-symmetric multiple cyclic amides. a) Cyclic amides as peptide binding receptor reported by Still and co-workers and b) Chiral bowl-shaped triamides functionalized with amide moieties reported by Azumaya and co-workers showed capsule-type dimer via H-bonds.

As the author stated in the Chapter 1, the synthesis of triazasumanene was successfully achieved enantioselectively and pass through two types of 3-fold *p*-methoxybenzyl(PMB)-protected chiral trilactam intermediates, cup-shaped (–)-**5** and bowl-shaped (–)-**6** (Scheme 2). Their highly symmetrical structure with H-bonded motif inspired the author to utilize their deprotected compounds as the new building blocks for the construction of three-dimensional capsule-unit,[54] which may further be applied to the formation of networking structure using metal coordination[55] and/or molecular encapsulation.[27] This Chapter will demonstrate the enantioselective preparation of chiral cup- and bowl- shaped trilactams (–)-**12** and (–)-**13** from PMB-protected chiral triamide precursors (–)-**5** and (–)-**6**, and their structural properties.

3.2 Results and discussion

3.2.1 Optimization of *p*-methoxy(PMB) deprotections from cup- and bowl-shaped cyclic triamides precursors

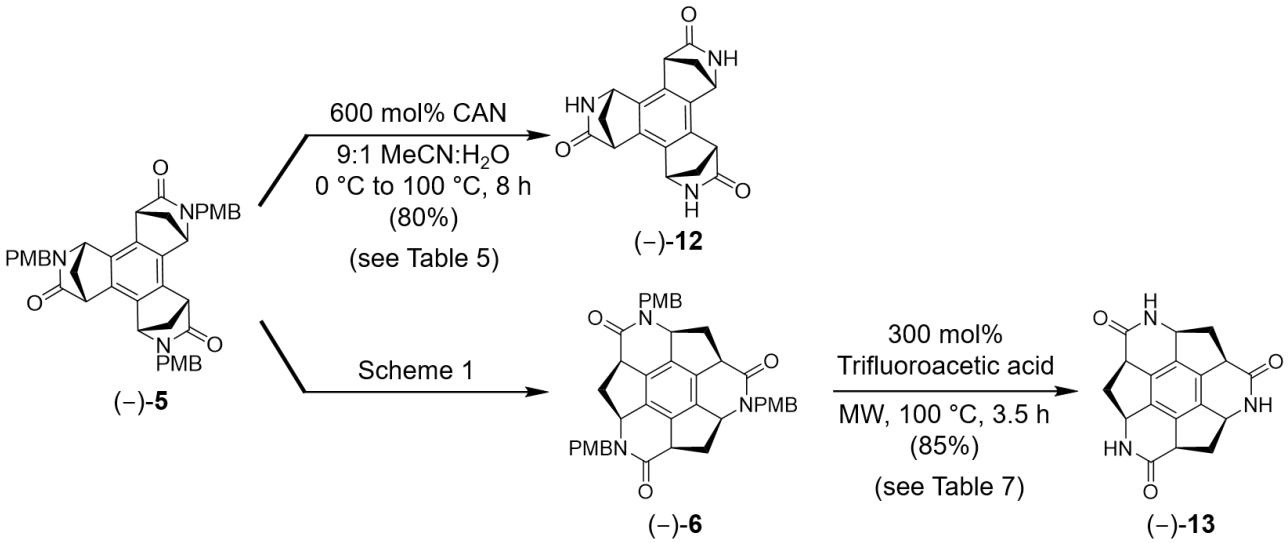

Scheme 5. Synthetic scheme of deprotection reactions of cup-shaped (–)-**5** and bowl-shaped (–)-**6** triamides.

The author first investigated the preparation of different triamides (–)-**12** and (–)-**13** (Scheme 5). Surprisingly, it was found that these two triamides exhibited very different chemical characters even at the first deprotection conditions investigation of PMB group from (–)-**5** and (–)-**6**. PMB-deprotection condition of (–)-**5** was firstly investigated by oxidative cleavage by $(NH_4)_2Ce(NO_3)_6$ (CAN)[56] (Table 5). At the first trial, the excess amount of CAN (600 mol%) was added to 0.02 M of (–)-**5** in MeCN/H_2O (14:1) mixed solvent at 27 °C and stirred for 12 h to give (–)-**12** in 51% isolated yield (Entry 1, Table 5). Performing the reaction with longer time (24 h) at 50 °C afforded the better yield to be 74% (Entry 2, Table 5). However, the PMB was not cleaved off in lower concentration of 3 (Entry 3, Table 5). Further optimization to apply 0.02 M of (–)-**5** in 9:1 MeCN/H_2O mixed solvent at room temperature for 8 h gave (–)-**12** in 80% isolated yield (Entry 4, Table 5).

Table 5. Optimization of PMB-deprotection of (–)-**5** by oxidative cleavage using CAN.

Entry	CAN (mol%)	Solvent ($MeCN:H_2O$)	Concentration (M)	T (°C)	Time (h)	Yield (%)[a]
1	600	14:1	0.02	27	12	51
2	600	14:1	0.02	50	24	74
3	600	14:1	0.006	50	24	0
4	600	9:1	0.02	27	8	80

[a]Isolated yield by PTLC silica gel

In contrast, the PMB-deprotection of bowl-shaped intermediate (–)-**6** by CAN was not effective despite numerous attempts (Table 6), indicating that the characters of (–)-**5** ((–)-**12**) and (–)-**6** ((–)-**13**) might be different. More harsh condition using excess amount of trifluoroacetic acid (TFA) under microwave (MW) irradiation was necessary to convert to (–)-**13** in 85% yield in 3.5 h (Table 7). Noteworthy is the MW irradiation PMB deprotection is the similar PMB deprotection method of tris(thioamide)triazasumanene ((–)-**8**) from the precursor (–)-**7** (Scheme 1).[22]

Table 6. Optimization of PMB-deprotection of (–)-**6** by oxidative cleavage using CAN.

Entry	CAN (mol%)	Solvent	Concentration (M)	T (°C)	Time (h)	Yield of PMB (%)[a]	Yield of (−)-**13** (%)
1	600	$MeCN:H_2O$ (9:1)	0.02	27	24	35	0
2	600	$MeCN:H_2O$ (9:1)	0.02	55	15	68	0
3	600	$CHCl_3$:$MeCN:H_2O$ (10:5:1)	0.02	27	24	57	0
4	600	$CHCl_3$:$MeCN:H_2O$ (10:5:1)	0.02	55	24	12	0
5	600	CH_2Cl_2:H_2O (9:1)	0.02	27	24	35	0

[a]Isolated yield by PTLC silica gel

Table 7. Optimization of PMB-deprotection of (–)-**6** by acidic hydration under MW irradiation.

Entry	TFA (excess)	T (°C)	Time (h)	Yield of (−)-**2** (%)
1	2 mL	100	2.5	59
2	2 mL	100	3.5	85

3.2.2 X-ray single analysis of cup-shaped trilactam (–)-12

X-ray single crystal analysis revealed the effect of the 3-fold symmetrical amide moieties in **12**. (–)-**12** afforded colorless block crystals by vapor diffusion method in MeOH/$CHCl_3$ at the ambient temperature under N_2 atmosphere (Fig. 23 and 24). As (–)-**12** possesses the chiral structure, the space group of the crystal packing was chiral $P2_1$. Two independent (–)-**12** molecules were observed forming three complementary NH···O type H-bonding pairs with averaged distances of 2.77 Å to give the dimer structure (Fig. 24a). The centroid-to-centroid distance between the two central benzene rings of the capsule-forming two (–)-**12** molecules was 6.05 Å. As observed in the reported cup-shaped trioxime dimer,[57] this dimeric structure possessed the inner cavity with the volume of 47.2 $Å^3$ (probe radius 1.4 Å, grid spacing 0.2 Å) calculated from the space-filling model of the dimer. This size is large enough for the encapsulation of H_2 (c.a., 11 $Å^3$).[58] Further specific feature of the crystal structure of (–)-**12** is to have one-dimensional $CHCl_3$ channel along the *c* axis, in which $CHCl_3$ molecules were bound to (–)-**12** by CH···O interaction (Fig. 24b and c). Among the dimers, CH···π interactions were also observed (Fig. 24c).

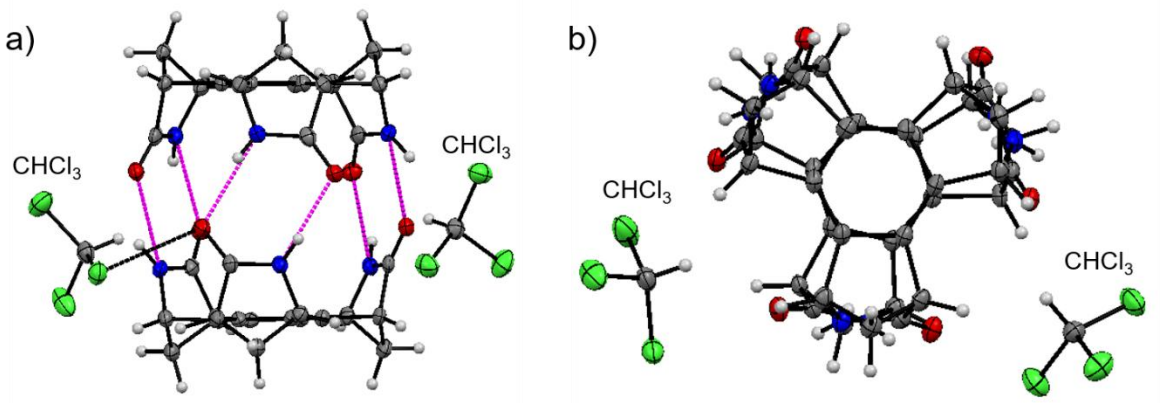

Figure 23. X-ray crystallographic analysis of (–)-**12** by vapor diffusion from $CHCl_3$/MeOH in glove box. ORTEP model of (–)-**12** a) side view, b) top view. In a) and b), the ellipsoids are shown in 50% probability. C, grey; N, blue; O, red; H, white; Cl, green.

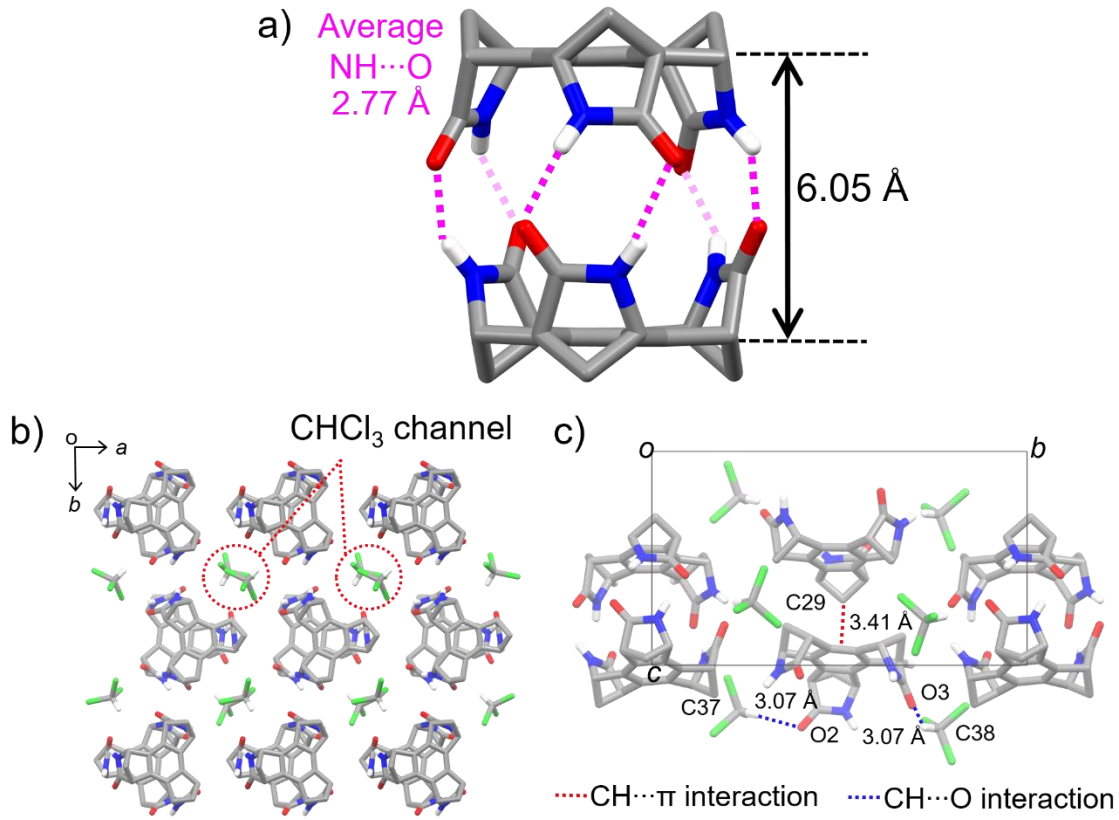

Figure 24. Crystal structures of (–)-**12**. a) A hydrophobic capsule-like dimer structure composed of two (–)-**12** molecules via three complementary NH···O type intermolecular hydrogen bonds. b) *c* axis projection and c) *a* axis projection of the packing structure of (–)-**12** crystal. C, grey; N, Blue; O, red; Cl, green. The hydrogen atoms are omitted for clarity.

3.2.3 Dimerization properties of (–)-12 and (–)-13

The simple structural difference, cup or bowl shape, caused the drastic solubility difference of (–)-**12** and (–)-**13**. Since (–)-**12** and (–)-**13** possess three amide moieties on the periphery, it is reasonable that they are soluble in polar solvent such as DMSO and DMF. However, the cup-shaped (–)-**12** also dissolved in less polar solvents such as chloroform and dichloromethane (e.g., > 5 mg/mL in CH_2Cl_2) (Table 8). Single crystals of (–)-**12** obtained by vapor diffusion method using $CHCl_3$ as the inner solvent (Fig. 25) also revealed the formation of dimer, indicating this amphiphilic nature of (–)-**12** attributable to the formation of the dimer especially in less polar solvent.

Table 8. Solubility of (–)-**12** and (–)-**13**.

Solvent	(–)-12[a]	(–)-13[a]
CH_2Cl_2	○[b]	X
$CHCl_3$	○[b]	X
MeOH	○	△
EtOH	○	△
DMF	○	○
DMSO	○	○
H_2O	X	X

○ Soluble △ Partially soluble X Insoluble

[a] Sample 0.5 mg per 1 mL of solvent
[b] Lower solubility when higher concentration

Nuclear magnetic resonance (NMR) spectroscopy was used to characterize the trilactam (−)-**12** and (−)-**13**. ^{1}H NMR and of two different trilactam products revealed the solubility difference behavior and were assigned as shown in Fig. 26 and 27, respectively. ^{1}H NMR results exhibited –NH amide chemical shift were clearly observed at 8.70 ppm in $CDCl_3$ and 8.0 ppm in $(CD_3)_2SO$ for (−)-**12** and (−)-**13**, respectively. This implied that PMBs were cleaved nicely from their corresponding precursor skeletons.

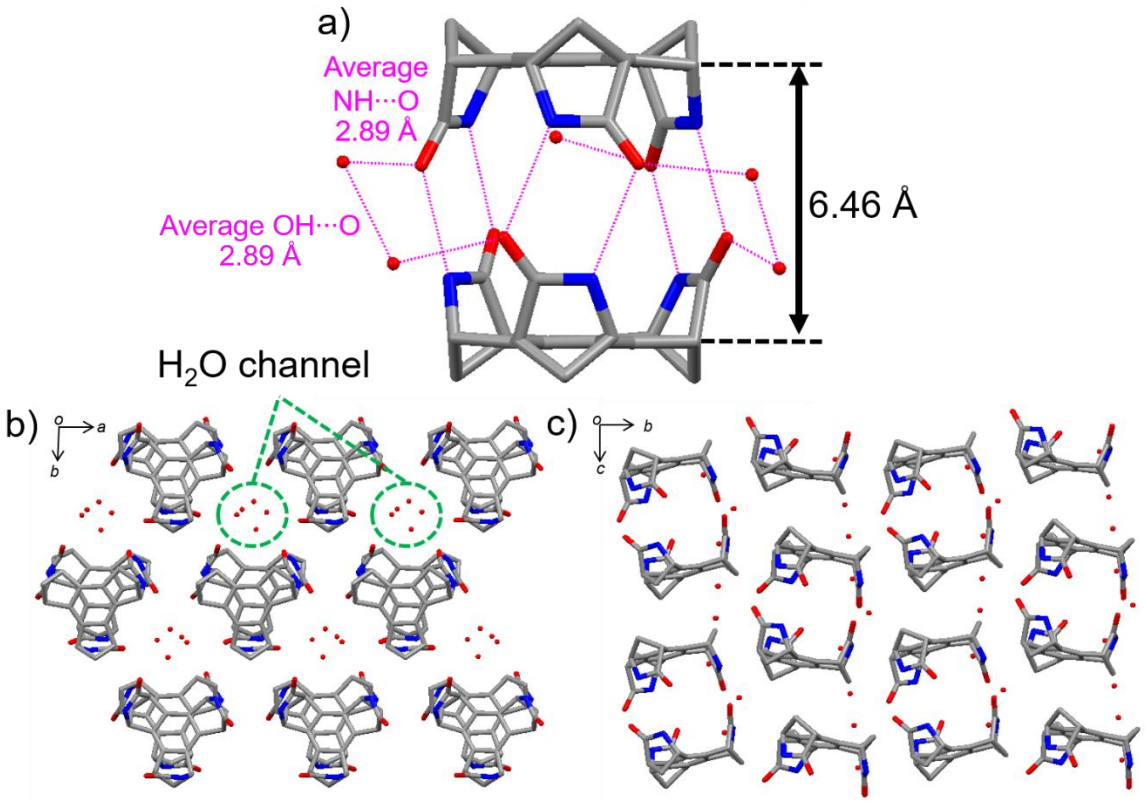

Figure 25. X-ray crystallographic analysis of (–)-**12** by vapor diffusion from $CHCl_3$/Hexane at the ambient temperature under air. a) Cap-stick model showing hydrophobic capsule-like dimer structure with average intermolecular NH···O and centroid-to-centroid lengths were shown. b) Top view and c) side view of the crystal packing structure showing the water channel-like located along *c* axis with the formation of OH···O type hydrogen bonds (2.67–2.80 Å). Though no direct interaction among the dimers was not confirmed, water molecules in the channels also formed strong OH···O type hydrogen bonds (2.62–2.78 Å) with amide moiety of (–)-**12** to bridge the dimers. The hydrogen atoms are omitted for clarity. C, grey; N, blue; O, red; H, white.

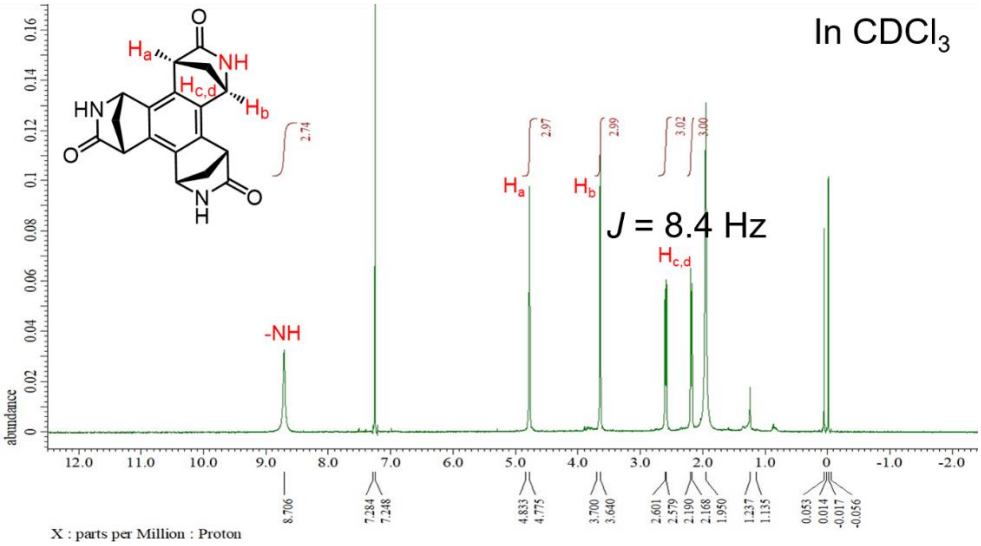

Figure 26. ^{1}H-NMR spectrum of (–)-**12** in $CDCl_3$.

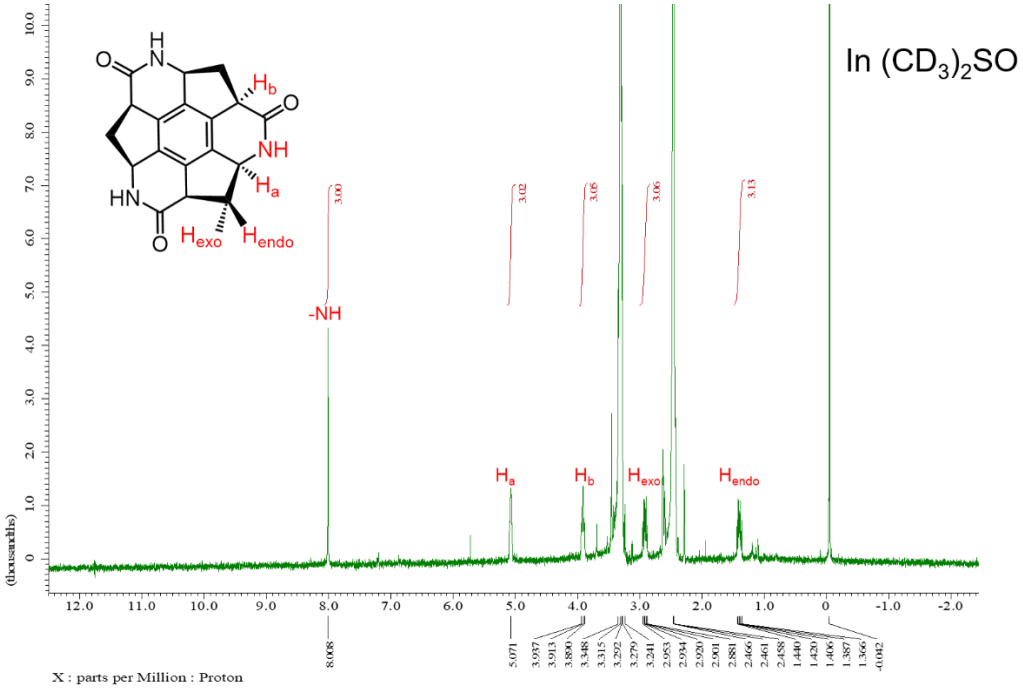

Figure 27. ^{1}H-NMR spectrum of (–)-**13** in $(CD_3)_2SO$.

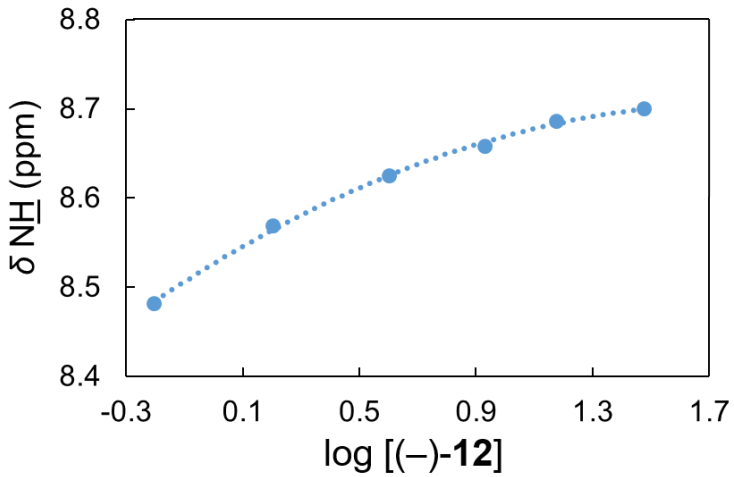

Figure 28. Concentration dependency of chemical shift of amide proton of (–)-**12** performed at 25 °C in $CDCl_3$.

To reveal the detailed aspect of the dimerization event of (–)-**12** in the solution state, concentration-dependent ^1H NMR measurement of (–)-**12** in $CDCl_3$ was performed (Fig. 28). At low concentration (0.625 mM at 293 K), the broad signal assignable to NH-lactam proton was observed at 8.48 ppm, while it shifted to lower 8.66 ppm as the concentration became higher to 8.5 mM. This indicated the equilibrium shift from the monomer to the H-bonded dimer upon higher concentration of (–)-**12**.

Variable temperature (VT) NMR of (–)-**12** in $CDCl_3$ solution gave additional information (Fig. 29). The amide proton shifted to higher magnetic field by heating, while to lower magnetic field by cooling the sample solution. This also indicated the presence of the equilibrium between (–)-**12** and its dimer. At the temperature below 243 K, the amide proton split into two distinguished peaks of broad peak at 8.9 ppm and sharp peak at 8.6 ppm, corresponding to the dimer and monomer species, respectively. The calculated abundance ratio of (–)-**12** and the dimer was 2.5:1 at 223 K in $CDCl_3$ solution according to the integral values of the broad and the sharp peaks.

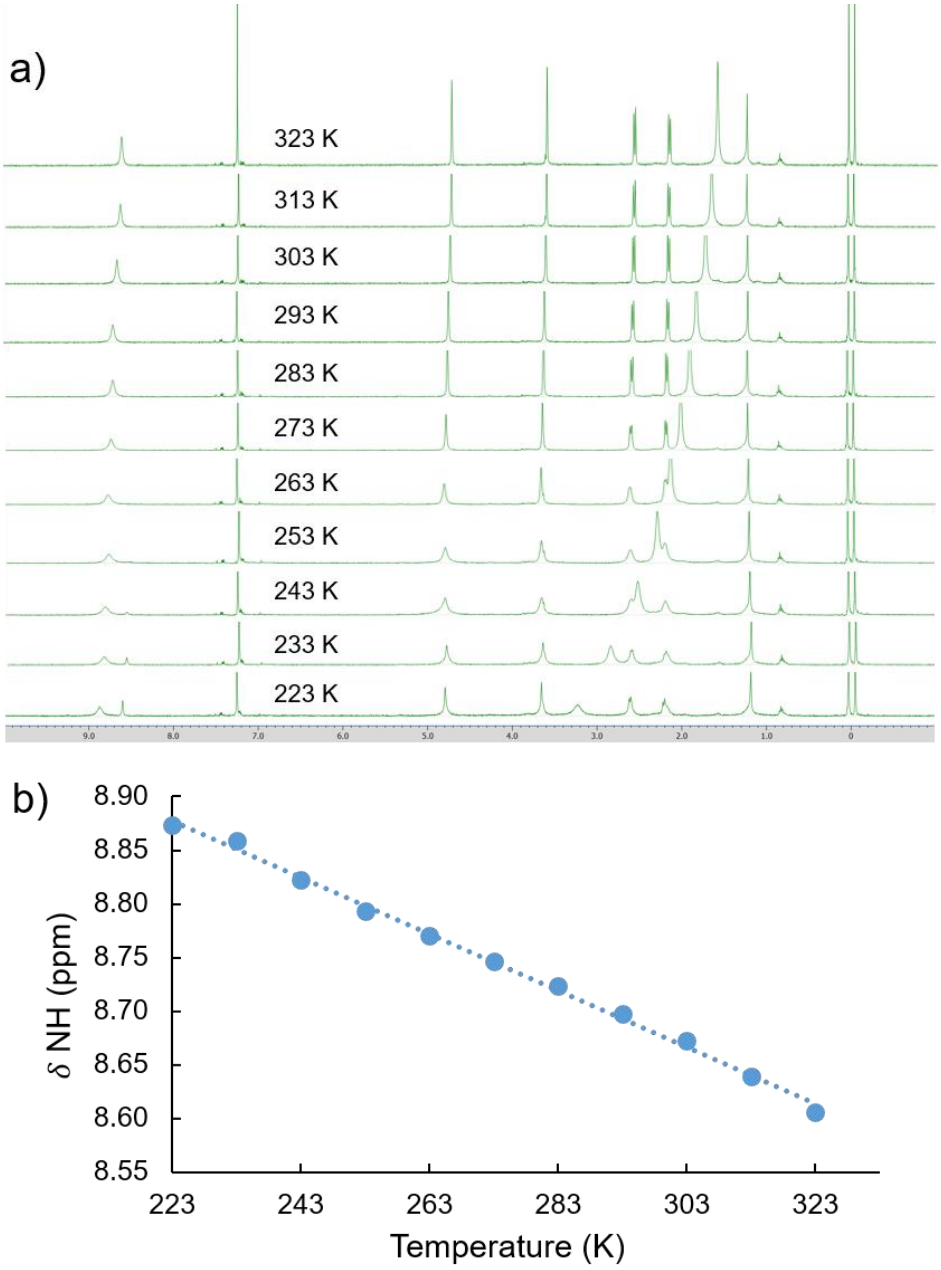

Figure 29. Temperature dependence ^{1}H NMR of 15 mM (–)-**12** in $CDCl_3$. a) VT ^{1}H NMR spectra revealed NH-lactam chemical shift (ppm) shifted to lower magnetic field by decreasing temperature. b) The graph showed linear relationship between –NH chemical shift and measuring temperatures.

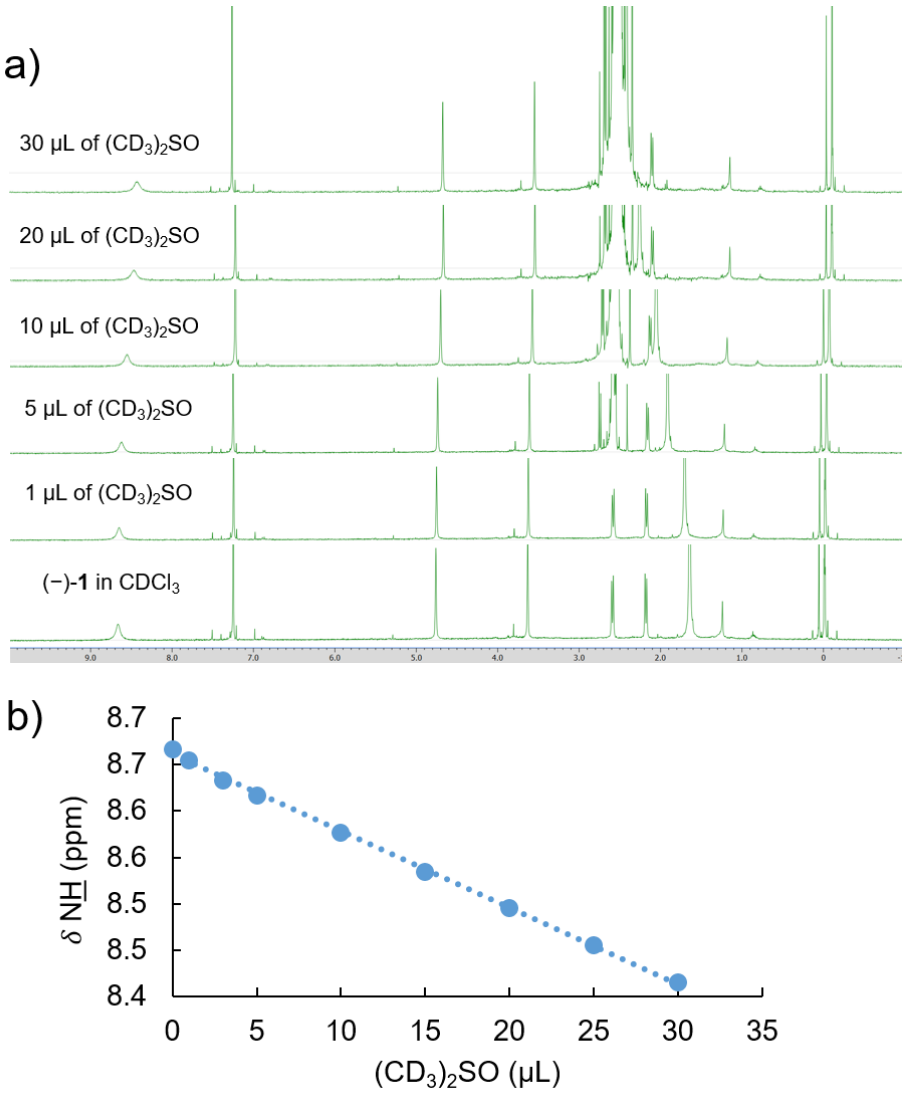

Figure 30. Portionwise addition of $(CD_3)_2SO$ into 15 mM (–)-**12** in $CDCl_3$. a) ^1H NMR spectra with increasing amounts of coordinating solvent $(CD_3)_2SO$. b) Graph plotted the relationship between NH-lactam chemical shift and adding amount of $(CD_3)_2SO$.

This dimerization event was interrupted by polar solvent, which easily forms H-bonds with lactam moieties at the rim positions of (–)-**12**. The portionwise addition of $(CD_3)_2SO$ made the quick shift of –NH protons to higher magnetic field, indicating the deformation of the H-bonded dimer into two (–)-**12**s (Fig. 30). These results indicated that the three complementary H-bonds in (–)-$\mathbf{12}_{dimer}$ was affected by outer environments in solution.

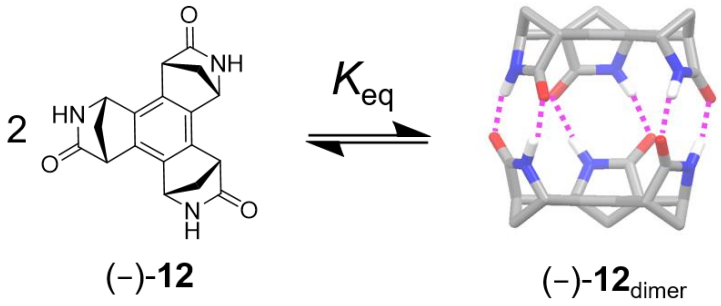

(–)-**12** (–)-**12**$_{dimer}$

Scheme 6. Equilibrium of non-H-bonded-monomer and H-bonded-dimer formation of (–)-**12**.

To comprehend the dimer formation study, I next quantified the binding ability of (–)-**12** in the solution state. As observed in Fig. 29a, broad singlet at 8.7 ppm of (–)-**12** in $CDCl_3$ at 293 K was attributable to the equilibrium of non-H-bonded-monomer and H-bonded-dimer states. It shifted between 8.5 ppm and 8.9 ppm by temperature change from 223 K to 323 K. With referring Lightner and coworkers work on the monomer-dimer equilibrium involved by the intermolecular H-bond formation in dipyrrinones,[59] the amide proton equilibrium constant (K_{eq}) of (–)-**12** was determined using amide proton chemical shifts (δ) from VT ^{1}H NMR (15 mM in $CDCl_3$) when the limiting chemical shifts; the amide proton chemical shift of fully non-hydrogen-bonded monomer (δ_M) and hydrogen-bonded dimer (δ_D) obtained at specific conditions, are known.

δ is the weighted average of the chemical shifts of the protons in separate environment, can be expressed by

$$\delta = X_M\delta_M + X_D\delta_D \qquad \text{Eq. 1}$$

While X_M is mole fraction of monomer in the solution and X_D is mole fraction of dimer, substitution in Eq. 1, δ can be obtained by

$$\delta = \frac{[M]\delta_M}{[M]+[D]} + \frac{[D]\delta_D}{[M]+[D]} \qquad \text{Eq. 2}$$

By using the law of mass expression: $[C]_0 = [M] + 2[D]$, while $[C]_0$ is total concentration of (–)-**12** in solution, [M] is concentration of monomer species, and [D] is concentration of dimer, By using expanding and substitutions, we could obtain K_{eq} as

$$K_{eq} = \frac{[D]}{[M]^2} \qquad \text{Eq. 3}$$

δ was recorded by ^{1}H VT NMR measurement from 243 to 323 K at 15 mM of (–)-**12** in $CDCl_3$. Van't Hoff plotted between ln K_{eq} versus 1000/T (K^{-1}) (Eq. 4) was allowed for the determination of $\Delta H°$ and $\Delta S°$ differences between the H-bonded monomer and non-H-bonded dimer from slope and intercept of the fitting linear curve, respectively.

$$\ln K_{eq} = \frac{\Delta S°}{R} - \frac{\Delta H°}{RT} \qquad \text{Eq. 4}$$

While δ is observed chemical shift of amide proton respecting to measured temperatures. δ_M corresponds to the limiting chemical shift for non-H-bonded monomer state obtained by lower concentration of (–)-**12** measured at high temperature (0.625 mM, measured at 333 K), which is 8.15 ppm and δ_D corresponds to the limiting chemical shift for fully H-bonded dimer obtained by higher concentration of (–)-**12** measured at low temperature (30 mM, measured at 223 K), which is 8.87 ppm. R is gas constant, 8.314 J mol^{-1} K^{-1}.

The obtained K_{eq} at each studied temperature indicated that the formation of (–)-**12**$_{dimer}$ was favorable at all considered temperature especially at lowest 243 K (K_{eq} ~ 23000 M^{-1}) (Table 9). The formation of (–)-**12**$_{dimer}$ was considered stronger than the previous study on 9-Acyl-dipyrrinone molecule,[59b] which showed monomer form in $CHCl_3$ solution (K_{eq} ~60 M^{-1} in 10 M^{-2} at 298 K), whereas formation of (–)-**12**$_{dimer}$ considered weaker than Kryptopyrromethenone,[59a] which known to perform strong H-bonded dimer both in crystal and in $CHCl_3$ solution (K_{eq} ~23000 M^{-1} at 295 K) (Fig. 31).

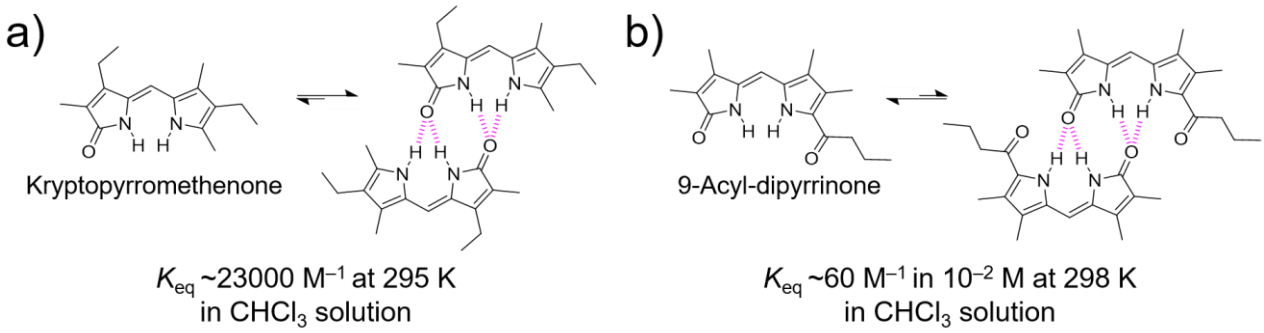

Figure 31. Monomer-dimer equilibrium in $CHCl_3$ solution of a) Kryptopyrromethenone and b) 9-Acyl-dipyrrinone.

Van't Hoff analysis using K_{eq} values allowed us to evaluate the thermodynamic parameters $\Delta H°$ and $\Delta S°$ for the equilibrium between (–)-**12** and its dimer at this considered concentration. The slope and the intercept of fitting linear curve were 3.5782 and −4.9098, which $\Delta H°$ and $\Delta S°$

were calculated as −29.8 kJ mol^{-1} and −40.8 J mol^{-1} K^{-1}, respectively (Fig. 32). Noteworthy is the monomer-dimer equilibrium of (–)-**12** were additional confirmed by ESI-MASS, which was clearly shown the mass of Na^+ at 344.1124 and 665.2244 for monomer-Na^+ and dimer-Na^+, respectively (Fig. 33).

Table 9. Parameters for calculation of equilibrium constant (K_{eq}) of 15 mM of (–)-**12** in $CDCl_3$.

Temperature (K)	δ NH (ppm)	1000/Temperature (K^{-1})	K_{eq} (M^{-1})	In K_{eq}	$\Delta G°$ (kJ mol^{-1})
243	8.82	4.11	23600	10.0	−19.8
253	8.79	3.95	8980	9.10	−19.4
263	8.77	3.80	5140	8.54	−19.0
273	8.75	3.66	3190	8.07	−18.6
283	8.72	3.53	2190	7.70	−18.2
293	8.70	3.41	1490	7.30	−17.8
303	8.67	3.30	1060	6.97	−17.4
313	8.64	3.19	705	6.56	−17.0
323	8.61	3.09	491	6.20	−16.1

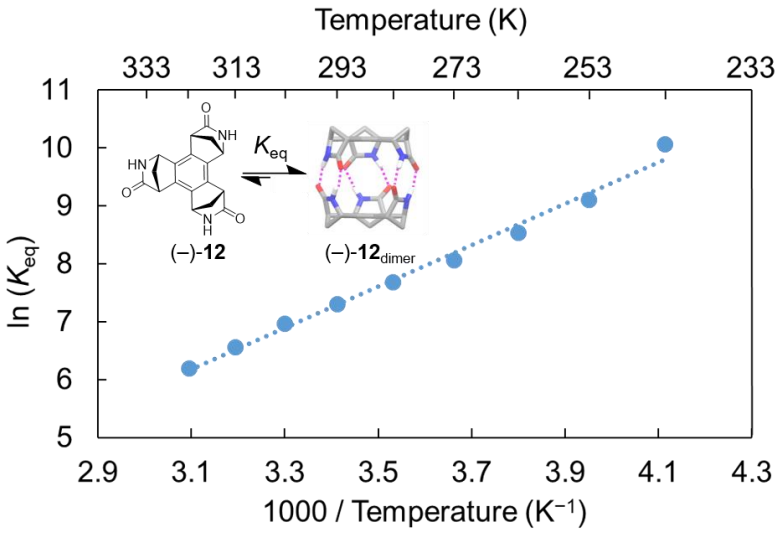

Figure 32. Van't Hoff plot constructed from amide proton chemical shifts for (–)-**12** in $CDCl_3$ measured at 243 to 323 K.

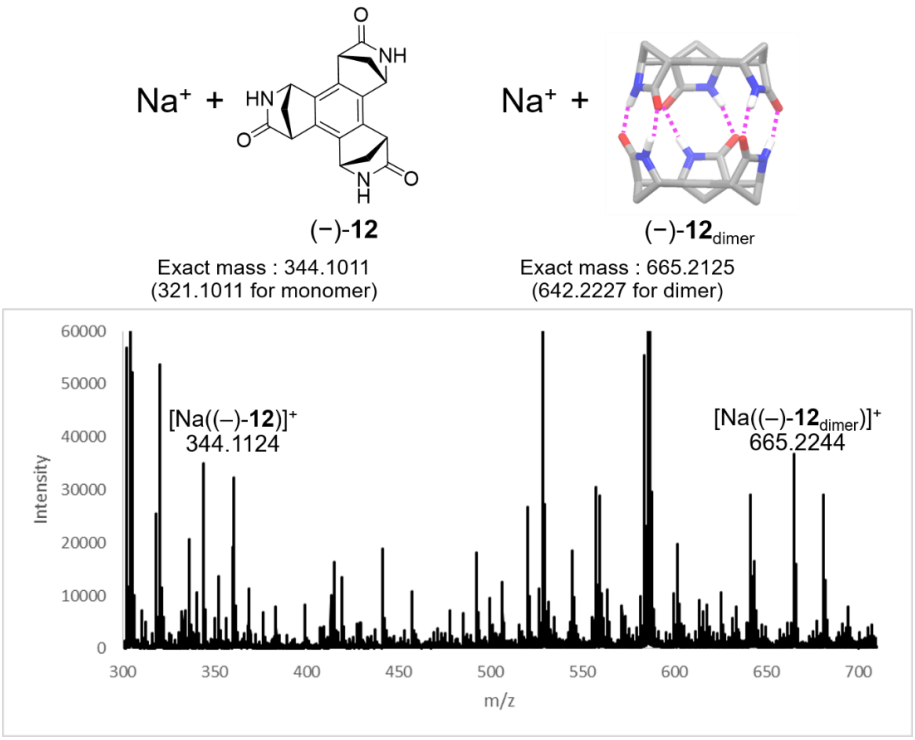

Figure 33. ESI-Mass revealed the monomer and dimer of (–)-**12** (20 μM in acetonitrile solution, measured in positive mode).

The same attempt was applied to bowl-shaped (–)-**12** to analyze its hydrogen-bonded formation, revealing the significance of structural factor for dimerization. Unlike (–)-**12**, (–)-**13** were only soluble in polar solvents (Table 8). DFT calculations clearly explained this phenomena. We considered two possible spatial arrangements in terms of the dimer formation of bowl-shaped (–)-**13**, (–)-**13**$_{dimer}$-**A** with one NH···O type hydrogen bond and (–)-**13**$_{dimer}$-**B** with three complementary NH···O type hydrogen bonds (Fig. 34).

First, the ground state cup-shaped dimer (–)-**12**$_{dimer}$ and two proposed bowl-shaped (–)-**13**$_{dimer}$-**A** and (–)-**13**$_{dimer}$-**B** structures were conducted full optimized at the B3LYP/6-31+G(d,p) level of theory because of the presence of heteroatoms in the molecules. All calculations were performed with the Gaussian09. The local minima of each structures were confirmed without imaginary vibrational frequencies. Zero-point energy correction is considered for calculation of binding energy calculation. The relative binding energies of dimerization could be determined by

$$\text{Relative Binding Energies} = E_{dimer} - 2(E_{monomer}) \quad \text{(unit in kcal mol}^{-1}\text{)} \quad \text{Eq. 5}$$

While E_{dimer} responded to the optimized total energy of each dimer structures and $E_{monomer}$ referred to the optimized total energy of their corresponding (cup or bowl) monomer conformation.

The corresponding relative binding energies and some H-bonded parameters calculation results were shown in Table 10. In a comparison of the six NH···O type hydrogen bonds in (–)-**12**$_{dimer}$ and (–)-**13**$_{dimer}$-**B**, (–)-**12**$_{dimer}$ possessed more desirable H-bonded dimer structure, corresponding to have ~8.8 kcal mol^{-1} lower relative binding energy than (–)-**13**$_{dimer}$-**B**, while the H-bonded distance were almost equal. (–)-**13** $_{dimer}$-**A**, the one H-bonded unit dimer, of course, proposed the shortest H-bond distance, realizing strongest H-bond of the three.[60] However, the presence of only one pair of H-bond in (–)-**13**$_{dimer}$-**A** afforded total 18.7 kcal mol^{-1} higher binding energy of it than (–)-**12**$_{dimer}$ possessing six H-bonds. These results suggested that shallower bowl-shaped (–)-**13** forms H-bonded dimer structure in less favorable manner than in the case of (–)-**12**, which corresponds to their solubility difference.

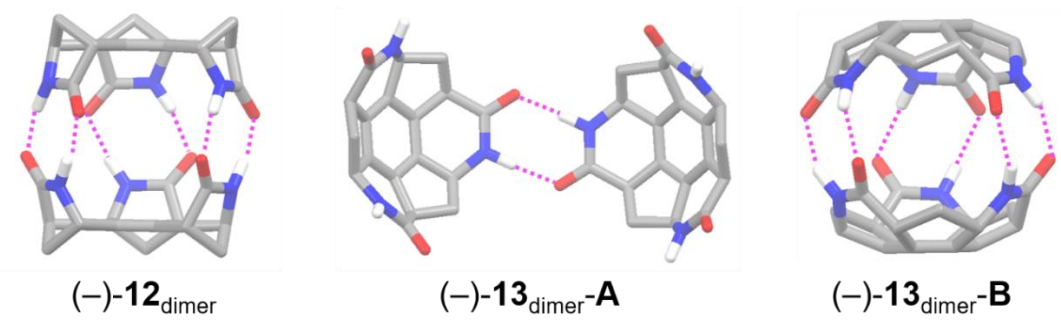

Figure 34. Optimized dimeric structure of (–)-**12**$_{dimer}$, (–)-**13**$_{dimer}$-**A** and (–)-**13**$_{dimer}$-**B** at the B3LYP/6-31+G(d,p) level of theory. The pink dash lines correspond to NH···O hydrogen bonds. Some of hydrogen atoms are omitted for clarity.

Table 10. Relative binding energy and intermolecular hydrogen bonded parameters of (–)-**12**$_{dimer}$, (–)-**13**$_{dimer}$-**A** and (–)-**13**$_{dimer}$-**B**. Calculated at B3LYP/6-31+G(d,p).

H-bonded parameters	(–)-**12**$_{dimer}$	(–)-**13**$_{dimer}$-**A**	(–)-**13**$_{dimer}$-**B**
Relative binding energy (kcal mol^{-1})	–31.0	–12.3	–22.2
Averaged N(H)···O distance (Å)	2.90	2.89	2.94
NH···O angle (°)	168	179	152
Centroid-to-centroid distance (Å)	6.32	9.06	6.98

3.2.4 Metal coordination of cup-shaped trilactam

Finally, the capsule-like dimer of (–)-**12** was utilized for the preparation of the host-guest network system using metal coordination. Complexation of (–)-**12** with $Zn(NO_3)_2 \cdot 6H_2O$ by layer-diffusion method in $CHCl_3$/MeOH afforded clear colorless block-shaped crystals. Single crystal X-ray analysis revealed that Zn was successfully introduced in the system to give the network structure composed of hydrogen-bonded dimer of (–)-**12** (Fig. 35). In a dimer, two Zn^{2+}(pale green sphere) directly coordinated to carbonyl oxygens of two amide parts on a same cup-shaped unit of the dimer (Fig. 35, purple part), bridging the neighbouring dimers to form two-dimensional network structure (Fig. 35b and d, purple part). All Zn^{2+} possessed octahedral coordination geometry and additionally coordinated two nitrates (pink) and two water molecules (pale blue) (Fig. 35a). Noteworthy is the same attempt with $Co(NO_3)_2 \cdot 6H_2O$ provided amorphous solid product, which indicated the unsuccessful formation of networking structures.

Interestingly, by introducing Zn^{2+} into the system, the centroid-to-centroid distance in the dimer became slightly shorter compared to the pristine (–)-**12** with water channel (from 6.46 Å to 6.37 Å), while longer than the one with $CHCl_3$ channel (from 6.05 Å to 6.37 Å) (Fig. 36). These results indicated that metal coordination allows not only the networking of cup-shaped trilactam but also the adjustment of the centroid-to-centroid distance of the dimer structure.

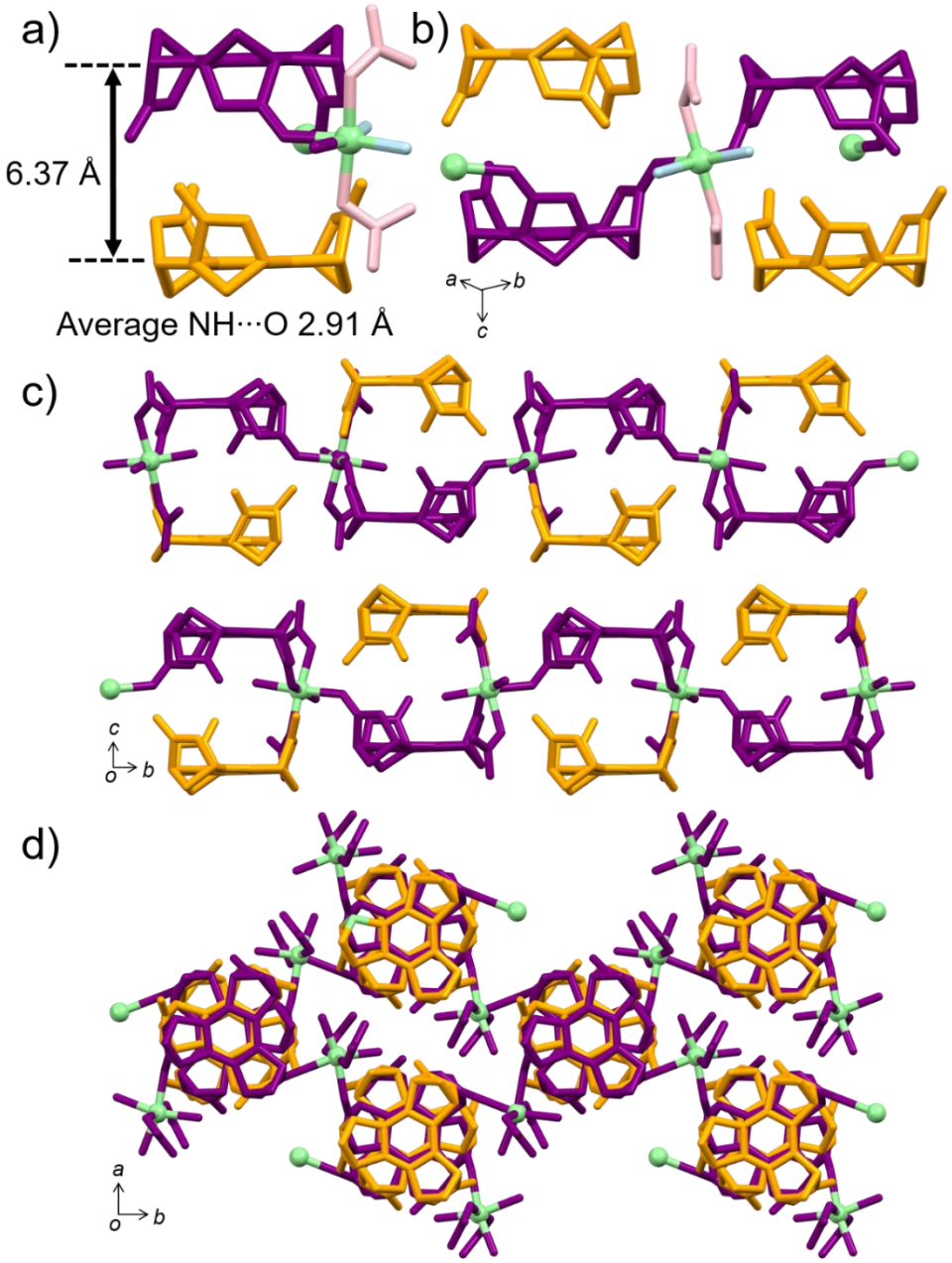

Figure 35. X-ray crystallographic analysis of complexation of (–)-**12** and $Zn(NO_3)_2 \cdot 6H_2O$ by layer-diffusion method from $CHCl_3$/MeOH in ambient air and temperature. a) cap-stick model showing hydrophobic capsule-like dimer structure with shorter centroid-to-centroid distance and Zn (pale green sphere) coordinated to two nearby dimer (purple), two nitrates (pink) and two water molecules (pale blue). b) top and c) side view of the crystal packing structure showing the Zn atom acted as a horizontal linker connected neighboring dimers in the same row (purple) and the free monomer (yellow). The hydrogen atoms are omitted for clarity.

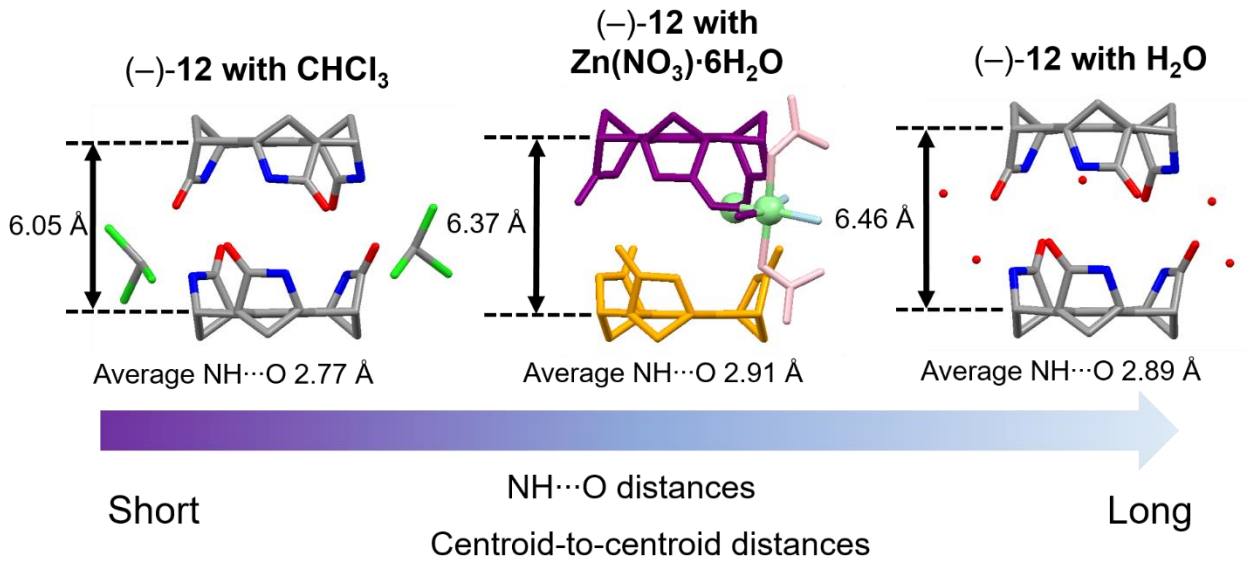

Figure 36. X-ray crystallographic analysis of (–)-**12** by different preparation conditions. The ordered of shortest centroid-to-centroid distances of the dimeric structures were shown followed from pristine (–)-**12** with $CHCl_3$, coordination with Zn, and pristine (–)-**12** with water with 6.05, 6.37, and 6.46 Å, respectively. The hydrogen atoms are omitted for clarity. C, grey; N, blue; O, red; H, white; Cl, green; Zn, pale green; nitrate, pink; water molecule, pale blue; (–)-**12** connected to Zn, purple; free (–)-**12**, yellow.

3.3 Conclusion

In summary, novel cup- and bowl-shaped trilactams (–)-**12** and (–)-**13** were successfully prepared. They exhibited different solubility behavior due to their structural features, cup and bowl shapes. The cup-shaped trilactam (–)-**12** showed the amphiphilic nature to dissolve in both non-polar to high polar solvent. This is because of the favorable formation of capsule-like dimer structure via three complementary NH···O type hydrogen bonding interactions at the rim positions. Solvation of highly polar solvent to (–)-**12** prohibited the formation of its complementary dimer, while the bowl shaped (–)-**13** was found to be soluble only in highly polar media due to its instability of dimer form. Complexation of (–)-**12** and Zn^{2+} afforded network structure with retaining the hydrogen-bonded dimer, realizing the control of inner space size.

3.4 Experimental section

Cup-shaped trilactam ((–)-12)

To a solution of (–)-**5** (50 mg, 0.073 mmol)[22] in acetonitrile (450 μL) at 0 °C was added CAN (242 mg, 0.44 mmol) dropwise as a solution in H_2O (50 μL). The mixture was stirred at 0 °C for 1 h, then at 25 °C for 7 h. The mixture was poured into 1:1 H_2O/ sat. $Na_2S_2O_3$ aq. (14 mL). The suspension was extracted with 3:1 $CHCl_3$/*i*-PrOH (12 mL × 3). The combined organic layer was dried over Na_2SO_4, filtered and the solvent was evaporated under reduced pressure. The crude product was purified by silica gel PTLC (MeOH/Ethyl acetate = 2:8) to afford (–)-**12** (18 mg, 0.056 mmol, 80%) as a white solid. R_f = 0.20 (MeOH/Ethyl acetate = 2:8); m.p.: 160 °C (dec.); ^{1}H NMR (400 MHz, $CDCl_3$) δ (ppm) 8.70 (s, 3H), 4.76 (s, 3H), 3.63 (s, 3H), 2.60 (d, 3H, J = 8.4 Hz), 2.19 (d, 3H, J = 8.4 Hz); ^{13}C NMR (100 MHz, $CDCl_3$): δ (ppm) 202.9, 182.8, 57.5, 55.7, 51.7 ppm; IR (ATR): 3407, 3212, 2962, 1689, 1330, 1259, 1083, 1012, 790 cm^{-1}; HRMS (ESI, pos): *m*/z calcd for $C_{18}H_{15}N_3O_3Na$ [M+Na$^+$]: 344.1124. Found: 344.1011. *m*/*z* calcd for $(C_{18}H_{15}N_3O_3)_2Na$ [M_2+Na$^+$]: 665.2244. Found: 665.2125 (M = monomer form of (–)-**12**) (Fig. 28).

Bowl-shaped trilactam ((–)-13)

A solution of (–)-**6** (30 mg, 0.044 mmol)[22] in TFA (2 mL) was sealed in a microwave instrument vial (0.5-2 mL). The solution was irradiated with stirring at a fixed temperature of 100 °C for 3.5 h on a microwave apparatus. On completion of the reaction time, the vial was cooled with a stream of air and opened. From the obtained green solution, TFA was removed under reduced pressure, and the resulting solid was added to $CHCl_3$ and the mixture was sonicated for 5 min. The white solid was collected by filtration and washing with $CHCl_3$ (5 mL × 3) to afford pure compound (–)-**13** (12 mg, 0.037 mmol, 85%) as an off-white solid. m.p.: 165 °C (dec.); ^{1}H NMR ($(CD_3)_2SO$): δ (ppm) 8.00 (s, 3H), 5.07 (t, 3H, J = 8.16 Hz), 3.91 (t, 3H, J = 8.16 Hz), 2.92 (dt, 3H, J = 7.63, 13.2 Hz), 1.40 (dt, 3H, J = 7.63, 13.2 Hz); ^{13}C NMR ($(CD_3)_2SO$): δ (ppm) 172.3, 142.0, 141.0, 57.0, 43.6, 43.1 ppm; IR (ATR): 3255, 1635, 1608, 1434, 1313, 1197, 1130, 773 cm^{-1}; HRMS (EI$^+$) *m*/*z* calcd for $C_{18}H_{15}N_3O_3$ [M$^+$]: 321.1113. Found: 321.1102.

Crystal data for (–)-12

The diffraction data for (–)-**12** was recorded on a DICTRIS PILATUS3 X CdTM 1M Detector System (λ= 0.416700 Å) at 100 K at SPring-8 BL02B1. The diffraction images were processed by using RIGAKU RAPID AUTO. The structures were solved by direct methods (SHELXS) and refined by full-matrix least squares calculations on F^2 (SHELXL) using the Olex2 program package. $C_{38}H_{32}Cl_{16}N_6O_6$, crystal dimensions 0.30 × 0.20 × 0.10 mm^3, monoclinic, space group = $P2_1$, a = 9.5594(19) Å, b = 17.782(4) Å, c = 10.607(2) Å, α = 90°, β = 99.44(3) °, α = 90°, V = 1778.6(6) Å^3, Z = 2, ρ_{calcd} = 1.646 g cm^{-1}. 6950 unique reflections out of 8152 with $I > 2\sigma(I)$, 505 parameters, 1.141° < θ < 15.691°, R_1= 0.0374, wR_2= 0.0834, GOF = 0.984. Flack = 0.01(5). CCDC 1980863.

Crystal data for (−)-12 and $Zn(NO_3)_2{\cdot}6H_2O$

The diffraction data for (−)-**12** and $ZnNO_3{\cdot}6H_2O$ was recorded on Rigaku FR-E Superbright rotating-anode X-ray source with a Mo-target (λ = 0.71073 Å) equipped with a Rigaku RAXIS VII imaging plate as the detector at 150 K in house. The diffraction images processing and absorption correction were performed by using RIGAKU RAPID AUTO. The structures were solved by direct methods (SHELXS) and refined by full-matrix least squares calculations on F^2 (SHELXL) using the Olex2 program package. $C_{18}H_{17}N_4O_7Zn_{0.5}$, crystal dimensions 0.15 × 0.15 × 0.10 mm^3, orthorhombic, space group = $P2_12_12_1$, a = 9.828(2) Å, b = 17.526(4) Å, c = 21.191(4) Å, V = 3650(1) Å^3, Z = 8, ρ_{calcd} = 1.580 g cm^{-1}. 5069 unique reflections out of 8345 with $I > 2\sigma(I)$, 529 parameters, 3.02° < θ < 27.02°, R_1= 0.0994, wR_2= 0.1589, GOF = 1.079. Flack = 0.04(1). CCDC 1980864.

Chapter 4

Application of Cup-shaped Trilactams for Selective Extraction of Volatile Compounds with Analysis by Gas Chromatography-Mass Spectroscopy

S. Sartyoungkul, I. Thaveesangsakulthai, M. K. E. Cabello, C. Kulsing, H. Sakurai,

Analyst, **2020**, DOI: 10.1039/D0AN01061H

Chapter 4: Application of Cup-shaped Trilactams for Selective Extraction of Volatile Compounds with Analysis by Gas Chromatography-Mass Spectroscopy

4.1 Introduction

Several C_3-symmetric cage-like compounds exhibit molecular recognition of small guest molecules by multiple interactions such as hydrophobic, hydrophilic and H-bonded interactions.[54,61] Davis *et al* reported water-soluble C_3-symmetric cage-like compounds tailored by hydrophobic central benzene rings and amides binding sites to provide specific binding site and cavity selective to carbohydrate substrate β-D-gluocopyranose. The Monte Carlo Molecular Mechanics predicted the encapsulation complex through 10 intermolecular H-bonds (Fig. 37a).[54h] Enantioselective recognition to sugar substrates were demonstrated by Martinez *et al* using the chiral hemicryptophane cage combining an electron-rich cyclotriveratrylene (CTV) unit and polar amine groups (Fig. 37b). The chiral recognitions can be interchangeable from mannose and glucose by switching the chirality of CTV unit from M to P. DFT revealed the encapsulation interactions via CH···π and H-bonded interactions.[61a]

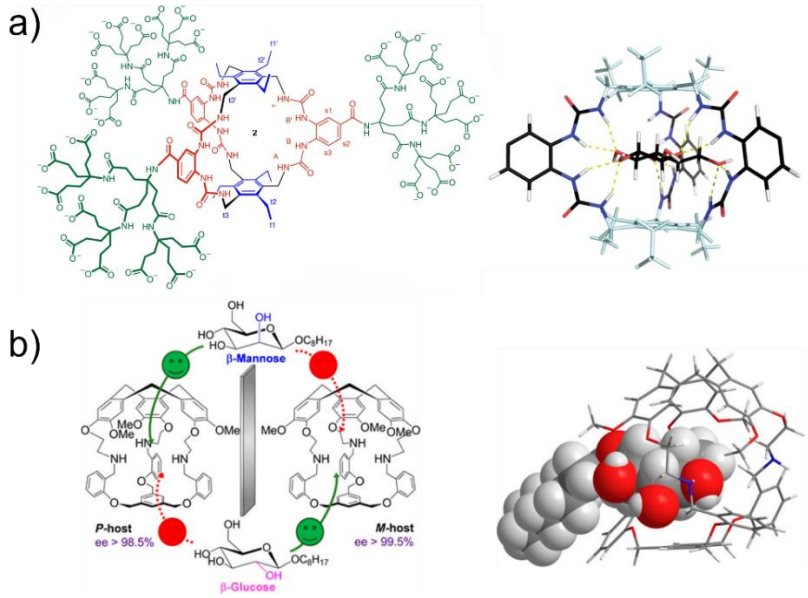

Figure 37. Some examples of C_3-symmetric cage-like compounds show molecular encapsulations of small substrates via multiple interactions. a) Water soluble cage compound reported by Davis and co-workers[54h] and b) chiral hemicryptophane cage by Martinez and co-workers with selective chiral recognition of small carbohydrate guests.[61a]

As the author presented in Chapter 3, the chiral C_3 symmetric hydrophobic capsule-like dimer (–)-**12** was nicely prepared through deprotection of PMB from the precursor (–)-**5**. Since (–)-**12** possesses H-bonded binding site from triamides, showing unique curved structure and soluble in various solvent; (–)-**12** could be a good candidate of building block for molecular recognition. Fig. 38 demonstrated proposed binding mode of (–)-**12** after introduction of some guest molecules. The possible mode of interactions derived from (–)-**12** could be hydrophobic interactions from central benzene ring, hydrophilic and/or H-bonded interactions at triamide moieties, and/or located inside the cavity of the curved structure. Hence, the suitable candidate guest molecules and methods to analyze the corresponding result needed to be considered.

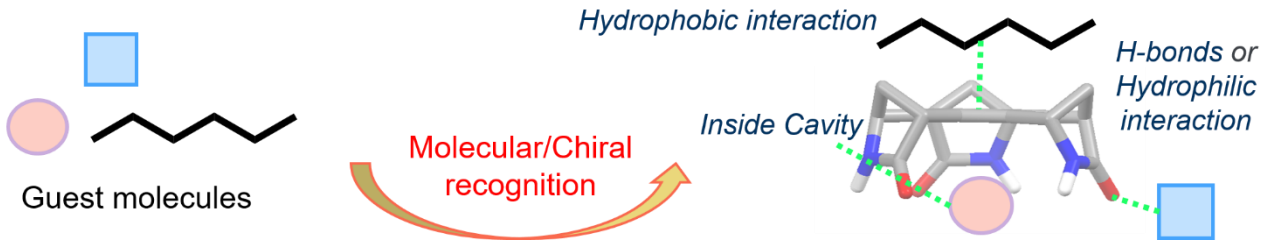

Figure 38. The proposed binding mode of (–)-**12** with different kinds of guest molecules via several interactions. The green dashed line indicated the possible interactions between (–)-**12** and guest molecules.

For candidate guest molecules, the author turned the interest to perfume, which consists of several (>100) achiral and/or chiral volatile odor active compounds extracted from the nature.[62] These volatile compounds exhibit various shaped (e.g., acyclic, cyclic, and terpenoid structures) and sizes composed with variety of functional groups (e.g., aldehydes, alcohols, esters), which provide several binding modes to the host molecules.

The analytical techniques solid phase microextraction (SPME) coupled with gas chromatography-mass spectroscopy (GC-MS) are applied to analyze the molecular recognition ability between **12** and the volatile compounds in perfume. SPME is often applied as a simple and fast method that requires only a small amount of sample preparation where solvent is effectively removed. Volatile compounds in the sample headspace are adsorbed onto the SPME fiber, offering concentration enrichment prior to the desorption into the GC instrument that allows for further analysis (Fig. 39).[63] This technique has been most commonly applied to preparing sample prior to GC analysis of a wide range of substances, including essential oils, fragrances, foods, beverages, and environmental, biological and petrochemical.[64] GC-MS is applied for untargeted analysis of volatile compounds in a range of multi-component samples such as essential oils, fragrance, food

or petroleum.[63,65] Compounds are tentatively identified according to matching with libraries of mass spectra and retention indices.[66] Therefore, SPME coupled with GC-MS could be suitable analysis method for randomly screening of molecular recognition of volatile compounds by **12** with exemption of one by one interactions study.

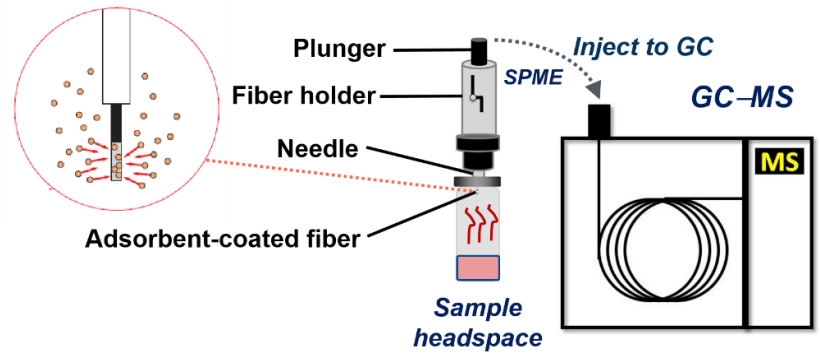

Figure 39. Diagram of analysis with SPME and GC-MS techniques.

In this Chapter, the author aim to utilize the two chiral trilactams (+)-**12** and (–)-**12** for molecular chiral recognition using an analytical chemistry approach. The experimental diagram was illustrated in Fig. 40. Both enantiomers **12** were selected for this work because they demonstrate well solubility in wide range of organic solvents, especially alcohol, which is the predominant solvent used to extract and produce perfume. Each enantiomer **12** was dissolved in methanol (MeOH) solvent and applied as a material for selective liquid phase extraction of odor active compounds in perfume. The extracted samples were analyzed by SPME and GC-MS. The results were discussed according to different volatile compounds peak areas from chromatograms and enrichment factors compared to the control experiment. The mode of interactions of **12** and some extracted compounds were further investigated by using molecular dynamic (MD) simulation and theoretical density functional theory (DFT) calculation.

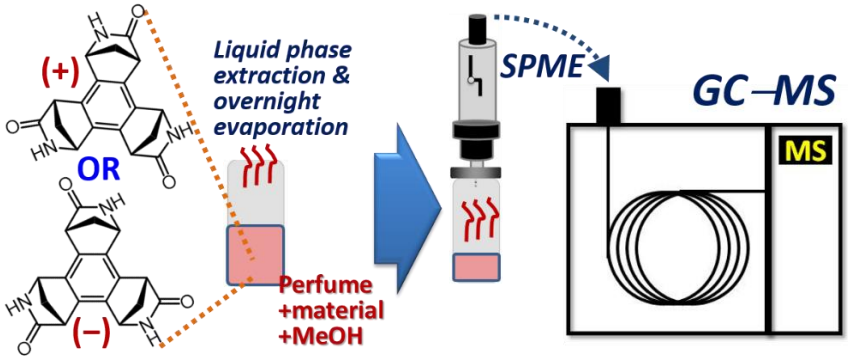

Figure 40. Diagram illustrating **12** applied as host molecules to encapsulate the volatile compounds in perfume and the overall analysis process with SPME GC-MS.

4.2 Results and discussion

4.2.1 GC-MS chromatogram after overnight extraction

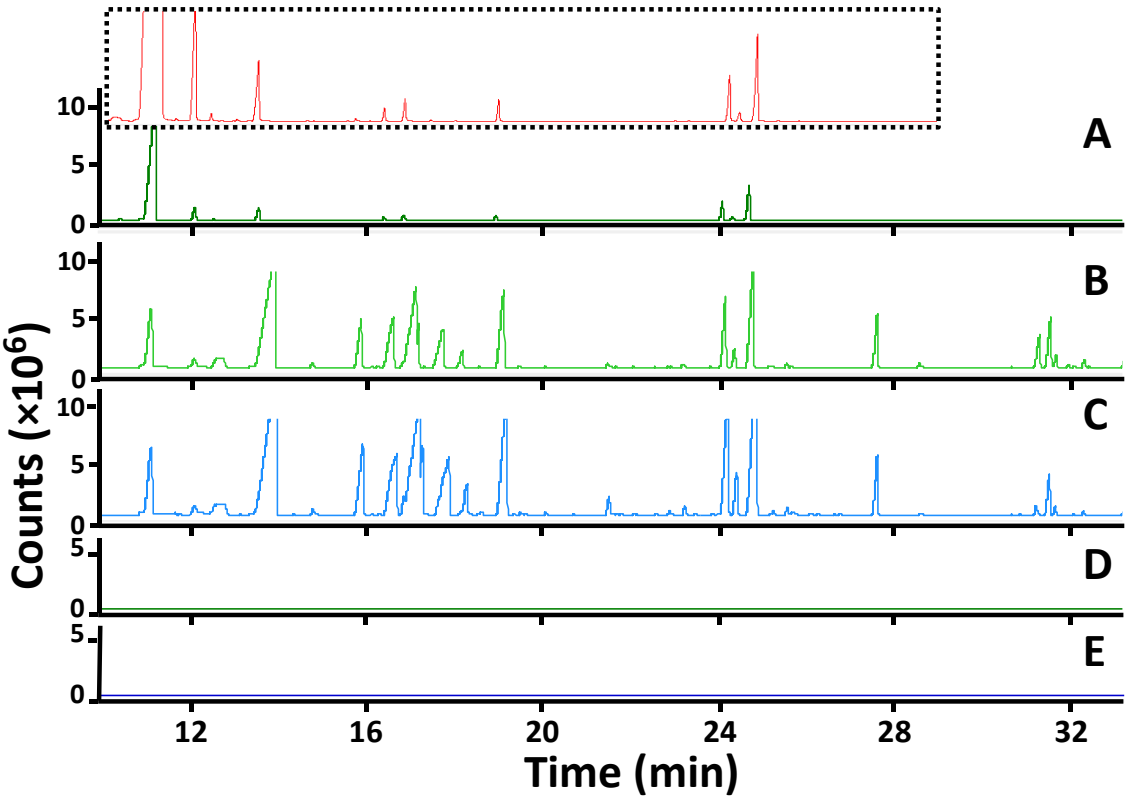

Figure 41. GC–MS total ion chromatogram of (A) volatile compounds present in a perfume solution with overnight extraction in MeOH (control sample) with the insert of the corresponding chromatograms of different extracts obtained by using (B) (+)-**12**, (C) (–)-**12** with the corresponding results for the solutions containing (+)-**12** and (–)-**12** without the perfume in D and E, respectively. The identified compounds are listed in Table 11.

The extraction performance in solution of (+)-**12** and (–)-**12** for analytes observed in perfume sample were investigated utilizing SPME GC-MS. The experimental setup is shown in Fig. 40. This consists of four different sets of experiments. In each set, the same perfume solutions were mixed with the solution of (+)-**12** or (–)-**12** material in MeOH in an open vial compared with the perfume in MeOH (without material) as the control. Each mixture was evaporated overnight under atmospheric pressure prior to the collection of the remaining liquid for the SPME GC-MS analysis. Re-crystallization of (+)-**12** and (–)-**12** occurred during the overnight extraction. The crystals were collected and analyzed revealing the re-crystallized shape was the same as that observed of $\mathbf{12}_{\text{dimer}}$. This indicates either a strong hydrogen bonding interaction within the dimer or an insufficient number of compounds interacting with **12** to result in detectable crystals.

The SPME GC-MS results of different samples after the overnight evaporation are illustrated in Fig. 41. For the control sample, compounds evaporation out of the perfume solution mainly occurred resulting in small amount of the volatiles detected in Fig. 41A. It should be noted that the qualitative compound profile was the same as that without overnight evaporation (insert in Fig. 41A) albeit with the evaporation resulting in smaller peak areas. The presence of lactams in the solutions decreased evaporation rates of volatile compounds resulting in their increased amount of the after evaporation compared with the control.

Together with evaporation of the solvent (mainly MeOH) out of the system, there was evidence of sample enrichment compared with the control as can be observed with the increasing peak areas in Fig. 41B and C. The solutions containing **12** in MeOH without perfume were also analyzed in order to confirm that the enriched signals were not caused by the materials (Fig. 41E and F). The list of the identified compounds is shown in Table 11. Three different extraction batches were performed for each material and the control. The enrichment factor (EF) was approximately the ratio of analyte peak area in each sample to area of the same analyte in control was used to indicate extraction performance for each set of analyte and material (Eq. 6). Higher enrichment factors are representative of stronger interactions between the analytes and each **12** enantiomers.

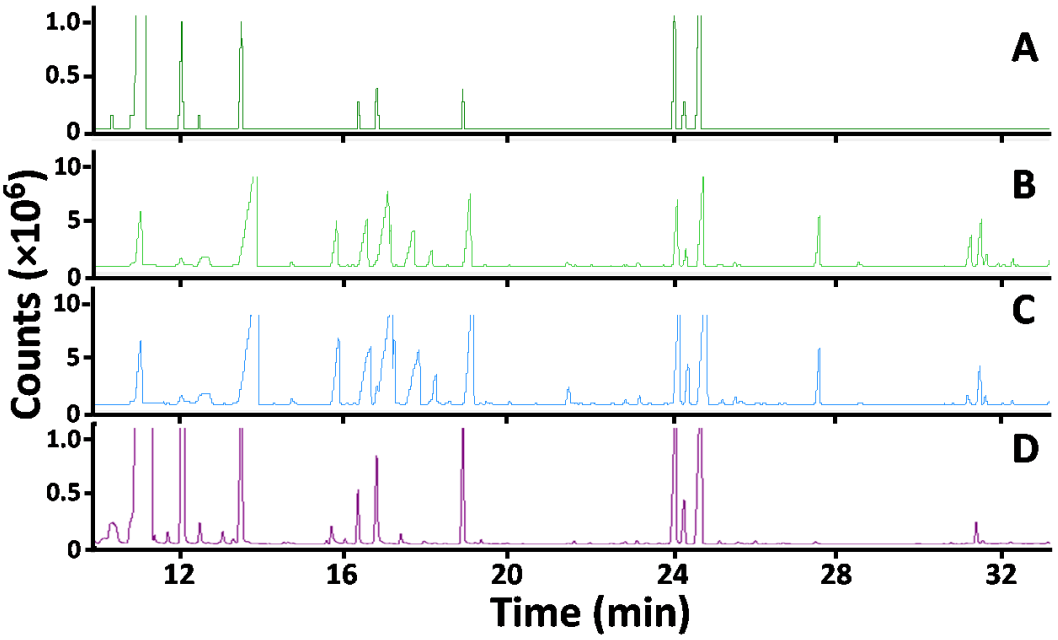

Figure 42. GC–MS total ion chromatogram of (A) volatile compounds present in a perfume solution with overnight extraction in MeOH (control sample) with the insert of the corresponding chromatograms of different extracts obtained by using (B) (+)-**12**, (C) (–)-**12** and (D) achiral 2-Piperidinone. The identified compounds are listed in Table 11.

$$\text{The enrichment factor} = \frac{\text{Analyte peak area of volatile compounds in sample}}{\text{Analyte peak area of volatile compounds in control}} \qquad \text{Eq. 6}$$

Table 11. Compound profiles of retention index from literature (I_{Lit}), average peak area (counts·s) with n = 3, enrichment factor (EF) analyzed with GC-MS with the potential compounds showing significant chiral recognition highlighted in bold and italic.

No.	Compound name	I_{Lit}	Peak area in Control	Perfume-(–)-12		Perfume-(+)-12		2-Piperidinone	
				Peak area	EF	Peak area	EF	Peak area	EF
1	Camphene	952	(9.2±4.0)×10^4	0±0	-[a]	0±0	-	0±0	-
2	Sabinene	974	(22±7.2)×10^5	(9.1±3.9)×10^4	-	(1.6±1.2)×10^5	-	0±0	-
3	3-Carene	1011	(3.0±1.6)×10^5	(2.0±1.8)×10^4	-	(3.4±1.7)×10^4	-	0±0	-
4	Sylvestrene	1027	(11±1.2)×10^7	(2.5±1.1)×10^7	-	(2.8±0.34)×10^7	-	0±0	-
5	7-Octen-2-ol, 2,6-dimethyl-	1064	(13±9.1)×10^5	(8.0±4.5)×10^6	6.1	(1.7±0.73)×10^7	13	(6.6±0.8)×10^4	1.5
6	Linalool	1099	(1.8±1.3)×10^7	(8.0±4.5)×10^7	4.5	(1. 2±0.18)×10^8	6.5	(7.1±0.8)×10^5	1.1
7	***l-menthol (LMT)***	***1175***	***(5.0±4.4)×10^5***	***0±0***	-	***(2.7±1.2)×10^7***	***54***	0±0	-
8	Linalyl formate	1215	0±0	(5.2±0.017)×10^7	NA[b]	(6.2±2.9)×10^7	NA[b]	0±0	-
9	6-Methyl-2-heptanol, 2-methylpropionate	1222	(4.4±2.9)×10^5	(1. 9±1.4)×10^7	43	(2.4±0.76)×10^7	54	(2.5±1.1)×10^4	5.8
10	Citronellol	1228	(3.1±2.6)×10^5	(5. 4±4.1)×10^6	17	(6.7±2.4)×10^6	22	(0.3±0.3)×10^4	0.2
11	Carvone	1242	(0.20±0.20)×10^4	(4.3±3.7)×10^5	22×10	(7.3±2.9)×10^5	37×10	0±0	-
12	Linalyl acetate	1257	(5.6±4.5)×10^6	(2.9±2.0)×10^7	-	(4.5±1.5)×10^7	8	(2.7±1.2)×10^5	1.3
13	***δ-EIemene***	***1338***	***(4.4±1.9)×10^4***	***(1.3±0.68)×10^5***	-	***(4.1±1.8)×10^5***	***9.3***	(0.3±0.3)×10^4	0.6
14	*α*-Terpinyl acetate	1350	(3.9±3.4)×10^4	(2.3±1.7)×10^5	-	(4.4±2.1) ×10^5	11	0±0	-
15	***Ylangene***	***1372***	***(1.7±1.2)×10^4***	***0±0***	-	***(7.4±6.1)×10^5***	***44***	(0.6±0.3)×10^4	22
16	***Copaene***	***1376***	***(5.3±2.7)×10^4***	***0±0***	-	***(1.5±0.67)×10^5***	***2.8***	(0.6±0.5)×10^4	0.5
17	*β*-Funebrene	1414	(8.0±3.1)×10^6	(2.2±1.6)×10^7	-	(3.7±1.7)×10^7	4.6	0±0	-
18	*cis*-Thujopsene	1429	(1.6±0.63)×10^7	(4.0±2.9)×10^7	-	(6.6±2.9)×10^7	4.1	(1.6±0.3)×10^6	0.5
19	Cyclamal	1466	(3.3±2.9)×10^4	(6.9±6.0)×10^5	21	(1.0±0.41)×10^6	32	0±0	-
20	*γ*-Himachalene	1477	0±0	(1.9±1.6)×10^5	NA[b]	(3.4±0.0)×10^5	NA[b]	0±0	-
21	*α*-Curcumene	1483	(1.0±0.80)×10^4	(0.60±0.50)×10^4	-	(1.2±1.0)×10^5	-	0±0	-
22	Lilial	1533	(3.8±3.3)×10^5	(7.0±5.6)×10^6	19	(1.3±0.47)×10^7	33	0±0	-
23	***Kharismal (KRM)***	***1649***	***0±0***	***(9.5±8.3)×10^5***	***NA[b]***	***(5.0±3.2)×10^6***	***NA[b]***	0±0	-
24	*β*-Acorenol	1649	(5.5±4.8)×10^4	0±0	-	(1.5±0.59)×10^5	-	0±0	-

[a]Insignificant enrichment effect.
[b]Enrichment factor was very high and could not be calculated due to the compounds not detected in control.

In general, the materials showed good enrichment performance for the compounds with *I* >1060 especially the cyclic terpenes with specific shapes and the oxygenated terpenes. The compounds with the *I* values above 1060 showed significant enrichment performance indicated by EF values of either >1 or NA (very high EF due to the compounds not detected in control) (see Table 11). The major volatiles enriched by both (+)-**12** and (–)-**12** with the average peak areas of

>5,000,000 counts·s were 7-octen-2-ol, 2,6-dimethyl- (**5**), linalool (**6**), linalyl formate (**8**), 6-methyl-2-heptanol, 2-methylpropionate (**9**), citronellol (**10**) and lilial (**22**). There are several kinds of interactions that can govern the extraction performance such as hydrophobicity, CH···π interactions, polarity, hydrogen bonding interactions or size selective interactions.[65b,67] Apart from their relatively higher boiling point or hydrophobicity captured by the *I* values of >1060, these enriched compounds contain either oxygen atoms (e.g., undergoing polar and hydrogen bonding interactions) or π-system (e.g., undergoing CH···π interaction). This indicates effective sample enrichment of these compounds using the synthetic **12** compounds (see the chromatograms in Fig. 41B and 41C with the control in Fig. 41A). However, the areas of several compounds were similar within the errors for the extraction using (+)-**12** and (–)-**12**.

For the enantioselective interactions, significantly higher enrichment factors were only observed for several compounds during the extraction with the (+)-**12**. This could be explained according to the excess of L-enantiomers of compounds obtained from plants observed as the perfume components which could prefer interaction with the (+)-**12**. The major components specifically enriched by (+)-**12** were *l*-menthol (LMT) (**7** with the enrichment factor of 54) and kharismal (KRM) (**23** with the enrichment factor not available due to the compound not being identified in control), respectively. These molecules contain oxygen atom(s) with a six or five membered ring, respectively (e.g., undergoing shape interaction). This specific enrichment was also observed for *δ*-elemene (**13**) with the six membered ring and the π systems as well as the isomers of ylangene and copaene (**15** and **16**, respectively) with the bended cyclic structures containing the π systems. The same experiments with achiral simple lactam, 2-piperidone, also used as extraction material to compare the chiral recognition efficient of the chiral cup-shaped trilactams (+)-**12**. The results were shown in Fig. 42 and Table 11, revealed that EF values of 2-piperidone with the same analytes were significantly lower than that of (+)-**12** (Entry **7**, **13**, **15**, **16**, and **23**). This is evidence that the (+)-**12** has the performance of liquid phase extraction via chiral recognition with active chiral odor compounds in perfume.

4.2.2 Molecular dynamics simulation and DFT calculation

Molecular dynamics (MD) is a computer simulation method for analyzing the physical movements of atoms and molecules for period of time. Hence, several literatures reported the MD simulations provides reliable method to study the mode of interactions between molecules. Recently, Smith and co-workers used MD simulations performed by Summit, the World's most powerful supercomputer to identify 77 (from > 8000) small drug compounds that bind to S-protein

of novel Wuhan coronavirus (SARS-CoV-2) at its host receptor region, which may be repurposed to limit viral recognition of host cells and/or disrupt host-virus interactions.[68]

The mode of interaction mechanisms with (+)-**12** and (–)-**12** and enriched compounds *l*-menthol (LMT) and kharismal (KRM) (Fig. 43), which showed high EF values from Table 11, were investigated with MD simulation. To confirm the MD simulation with experiment result and simplify the binding interaction study, the host molecule ((+)-$\mathbf{12}_{dimer}$ or (–)-$\mathbf{12}_{dimer}$) and guest molecule (LMT or KRM) were simulated in 1:1 ratio in ternary solvent system (MeOH/H_2O/EtOH) (the initial complex structures were shown in Fig. 44) and the corresponding results were measured as the radial distribution function (RDF), which calculated the point probability of finding a group at a given distance *r* around the reference particle.[69]

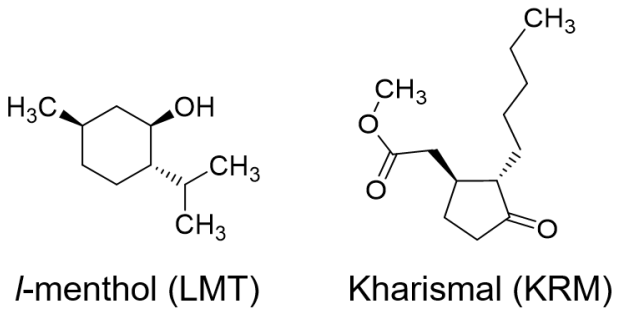

Figure 43. Molecular structures of selected compounds, *l*-menthol (LMT) and kharismal (KRM)

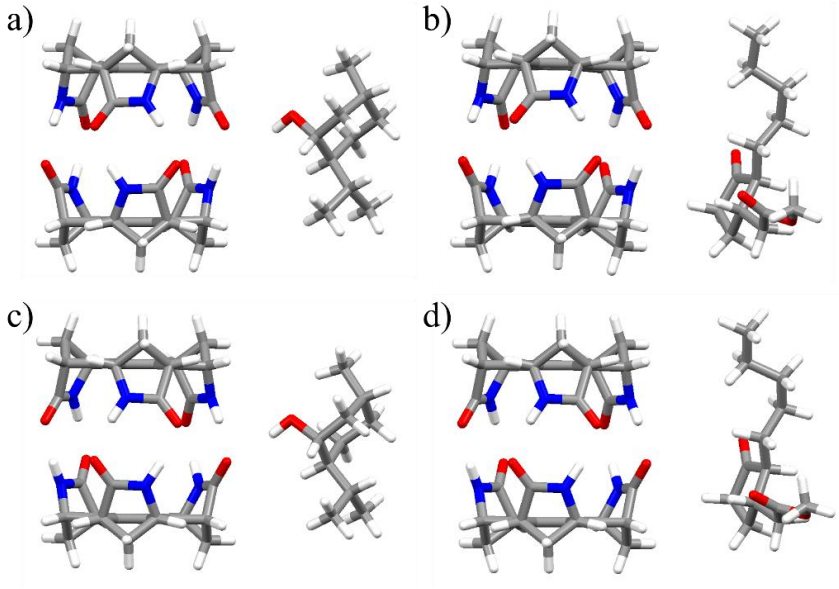

Figure 44. The initial molecular complex of (+)-$\mathbf{12}_{dimer}$ and selected enriched compounds a) LMT and b) KRM and (–)-$\mathbf{12}_{dimer}$ with c) LMT and d) KRM. C, grey; N, Blue; O, red; H, white.

To our surprise, the chiral **12**$_{dimer}$ was found to restrain dimer conformation even in the very high polar ternary solvent system with average N(H)···O bond distance of 2.92 Å (c.f., single crystal analysis 2.77 Å from Chapter 3), which indicated extremely strong intermolecular hydrogen bonds via three self-complementary NH···O types. The molecular RDFs were calculated as shown in Fig. 45 relative to the center of the mass of the **12**$_{dimer}$ as a reference (*g(r)* = 0). The molecular RDF indicated that the (+)-**12**$_{dimer}$ is significantly more favorable with g(r) about 2.5 and 1.5 for LMT (Fig. 45a, black) and KRM (Fig. 45b, black), which indicates strong interactions between these molecules over (–)-**12**$_{dimer}$, with *g(r)* being approximately **12** for LMT and KRM (Fig. 45a and b, red). In particular, KRM was found to have no significant interaction with (–)-**12**$_{dimer}$ as *g(r)* was found to be below 1 (Figure 45b, red). Moreover, the higher *g(r)* of (+)-**12**$_{dimer}$ implied a stronger interaction toward LMT over KRM. These results also corresponded to the calculated root mean square deviation (RMSD) illustrated in Fig. 46. RMSD were evaluated to compare the initial complex structure's change in movement, which implied the stability of the complex in period of time. Both RMSD of (+)-**12**$_{dimer}$ with LMT or KRM revealed small deviated curve from the initial complex (Fig. 46a and b, black) compared to that of (–)-**12**$_{dimer}$ (Figure 46a and b, red), implied the more stable complex between both enriched substrates and (+)-**12**$_{dimer}$.

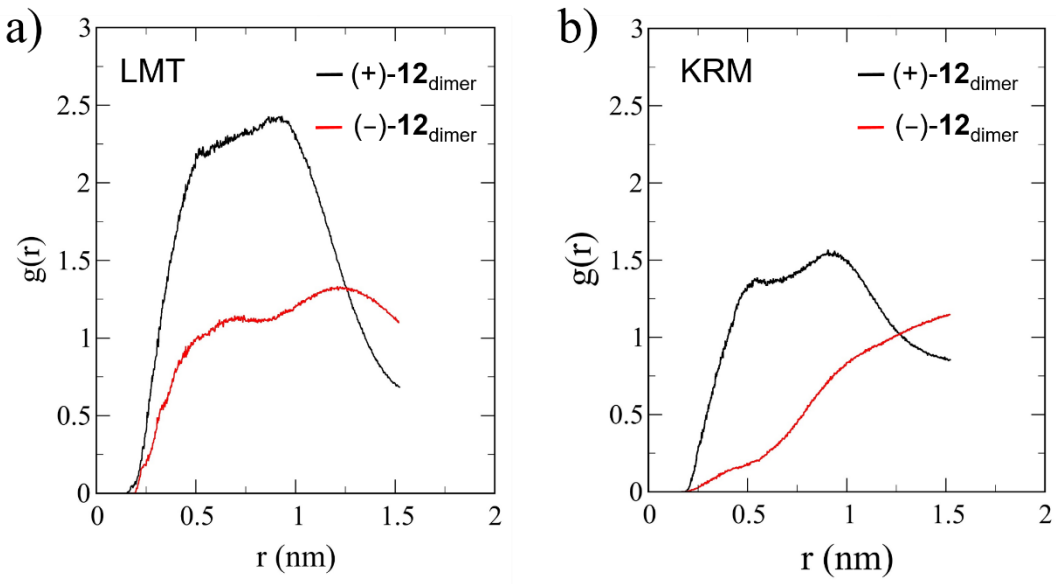

Figure 45. Molecular radial distribution function (RDF) calculation for **12**$_{dimer}$ and the enriched compounds: a) LMT and b) KRM by the relative distance *r* from the center of mass of **12**$_{dimer}$; black and red represents for (+)-**12**$_{dimer}$ and (–)-**12**$_{dimer}$, respectively.

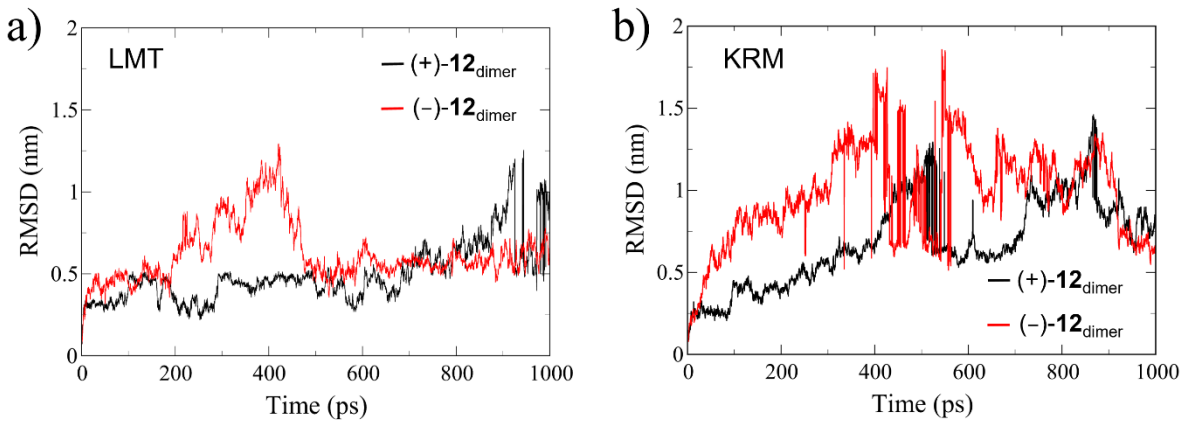

Figure 46. Root mean squared deviation (RMSD) measured the change in movement of the selected enriched compounds a) LMT and b) KRM from the initial complex structures; (+)-**12**$_{dimer}$ (black color) and (–)-**12**$_{dimer}$ (red color).

Since **12**$_{dimer}$ possesses three amide binding site on the rim position, the interaction between oxygen, nitrogen and hydrogen atoms of amide moiety could be responsible for interaction with the oxygen and/or hydrogen atoms of the enrich compounds via hydrogen bonds, van der Waals, or electrostatic interactions (Fig. 44). In order to investigate the mode of interactions between these compounds, RDF for specific atomic positions of oxygen and nitrogen atoms of (+)-**12**$_{dimer}$ toward hydrogen atom of selected guests are presented in Fig. 47. With LMT, the RDF curves initially showed a small peak of *g(r)* around 1 for oxygen atoms of the (+)-**12**$_{dimer}$ at a closed distance (about 0.2 nm) (Fig. 47a, black), which indicates that carbonyl oxygen atom from the (+)-**12**$_{dimer}$ backbone was closer to the hydrogen atoms of the LMT guest. Where $r > 0.3$ nm, the RDF curves of both oxygen and nitrogen atoms showed three significant peaks located at a similar distance and *g(r)* values that demonstrated the overlap interactions in both atoms. Some snapshots of the particular interactions of the (+)-**12**$_{dimer}$-**LMT** complex are visualized in Fig. 48. The mode of interactions between oxygen and/or nitrogen atoms of dimer with hydrogen atoms from hydroxyl, methyl and methylene groups of LMT were observed, and the bond distances involved hydrogen bonding (0.28–0.30 nm) and van der Waals interactions (0.30–0.34 nm).

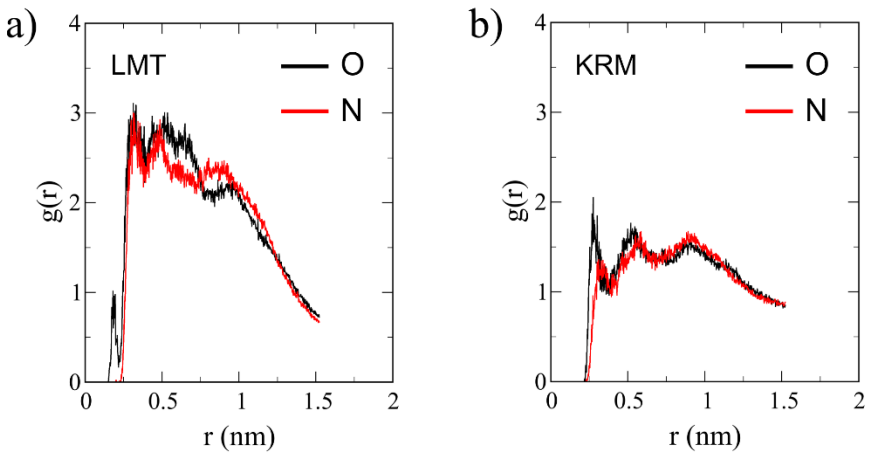

Figure 47. Atomic radial distribution function (RDF) calculation of oxygen atom of carbonyl group (black) and nitrogen atom of the amide groups (red) of (+)-**12**$_{dimer}$ by the relative to the distance *r* of the hydrogen atom of the enrich compounds a) LMT and b) KRM.

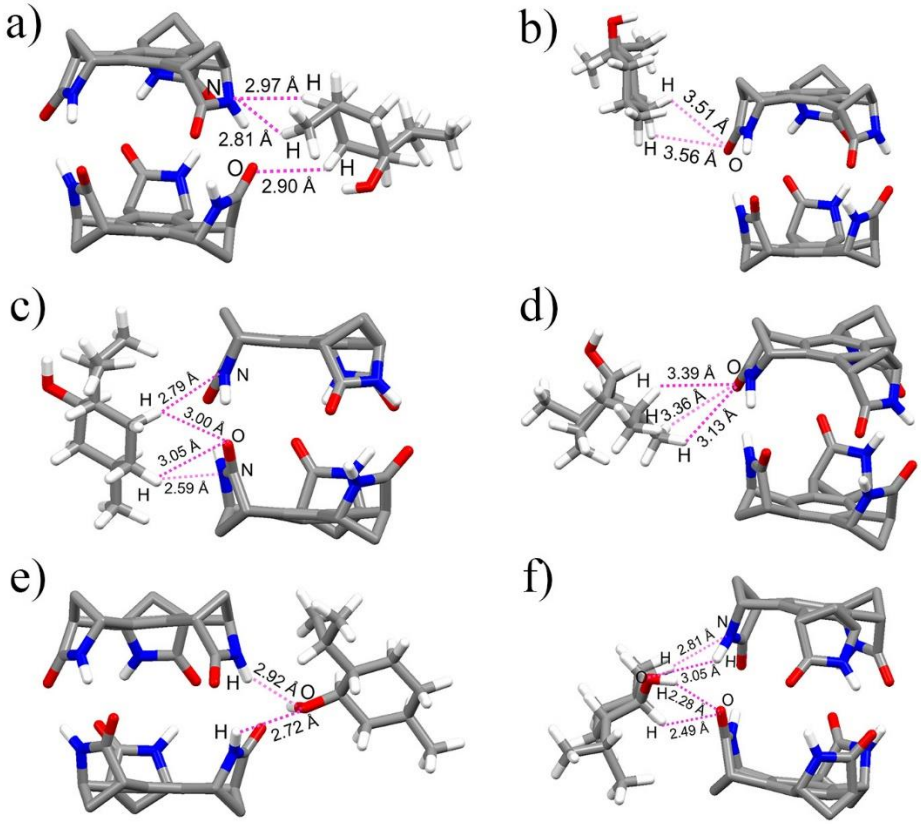

Figure 48. Some snapshots of (+)-**12**$_{dimer}$-**LMT** complex showing the mode of interactions and bond distances between (a-d) oxygen and/or nitrogen atoms of amide moiety of (+)-**12**$_{dimer}$ with methyl and methylene groups of LMT. (e-f) hydroxyl oxygen of LMT with hydrogen of –NH amide and methylene groups. The pink dashed lines correspond to the bond distance of the considered atomic interaction. C, grey; N, Blue; O, red; H, white. Some of the hydrogen atoms of (+)-**12**$_{dimer}$ are omitted for clarity.

Regarding the KRM complex, the RDF showed about three clear peaks with similar distance between the hydrogen atoms of KRM. Specifically, the *g(r)* intensity of oxygen atoms showed a slightly higher intensity (*g(r)* ~ 2) at closer distance $r < 0.4$ nm, which implies that the oxygen atom offered the main contributed interactions of the complex. The specific interactions of (+)-**12**$_{dimer}$-**KRM** were snapshotted and illustrated in Fig. 49, which reveals the interactions between oxygen and/or nitrogen atoms from amide moieties with methylene hydrogen either from alkyl chain and/or cyclopentane ring through hydrogen bonding or van der Waals interactions, which is similar to what was observed in (+)-**12**$_{dimer}$-**LMT** complex. It is noteworthy that, referring to the atomic RDF peak intensity *g(r)*, the interactions between (+)-**12**$_{dimer}$ and LMT is 1.5 times stronger than that with KRM (Fig. 47), which may resulted from stronger hydrogen bonding interaction through the proton donor from hydroxyl group of LMT, which participates to nitrogen atom of amide as a proton acceptor (Fig. 48e).

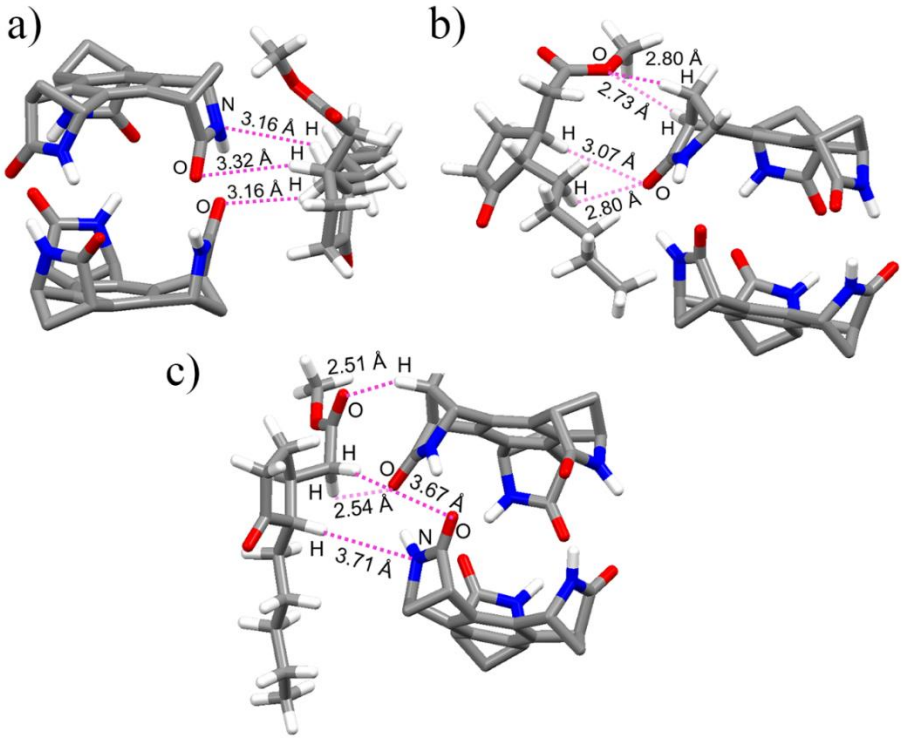

Figure 49. Some snapshots of (+)-**12**$_{dimer}$-**KRM** complex showing the mode of interactions coupled with bond distances between oxygen, nitrogen, and methylene hydrogen atoms of (+)-**12**$_{dimer}$ with carbonyl oxygen, methoxy oxygen, and/or methylene hydrogen atoms of KRM. The pink dashed lines correspond to the bond distance of the considered atomic interaction C, grey; N, Blue; O, red; H, white. Some of the hydrogen atoms of (+)-**12**$_{dimer}$ are omitted for clarity.

The interactions of potential complex (+)-**12**$_{dimer}$-**LMT** and (+)-**12**$_{dimer}$-**KRM** structures were further confirmed in higher level of calculation by DFT. The corresponding optimized structures and some bond distances are shown in Fig. 50 with more insight to be specific interactions. In the (+)-**12**$_{dimer}$-**LMT** complex, three main interactions were observed; the hydroxyl hydrogen pointed toward the –NH amide of the dimer caused by hydrogen bonds with N(H)···O bond distance 2.99 Å, which correlated to the previous RDF result from simulated MD structures (Fig. 47a and 48e and f) that revealed higher *g(r)* resulted from the stronger hydrogen bonding interaction from hydroxyl of LMT and amide binding site from (+)-**12**$_{dimer}$. The another interactions that from the heteroatoms of nitrogen and oxygen from amide provided the bonds to methylene hydrogen and methyl groups of LMT with polarities of approximately 2.55 and 3.20 Å, respectively (Fig. 50a). These result corresponded to the atomic RDF result by MD snapshots (Fig. 47a and 48a-d), which demonstrated that both oxygen and nitrogen of amide moiety were responsible for binding interactions. More complicated interactions could be observed in the (+)-**12**$_{dimer}$-**KRM** complex because of the existence of three oxygen atoms of KRM, thus more interactions of these heteroatom could be expected. From the lowest geometry structure, two oxygen atoms from carbonyl and methoxy groups of KRM could bind to the methylene protons of the dimer with distances of 2.41–2.92 Å. Otherwise, the oxygen atoms of carbonyl and –NH amide bonded to the methylene hydrogens either from cyclopentane rings or alkyl chains by 2.22–2.67 Å. The above result correlated with RDF by MD simulations (Fig. 47b and 49), which showed that the carbonyl oxygen favored binding with the dimer.

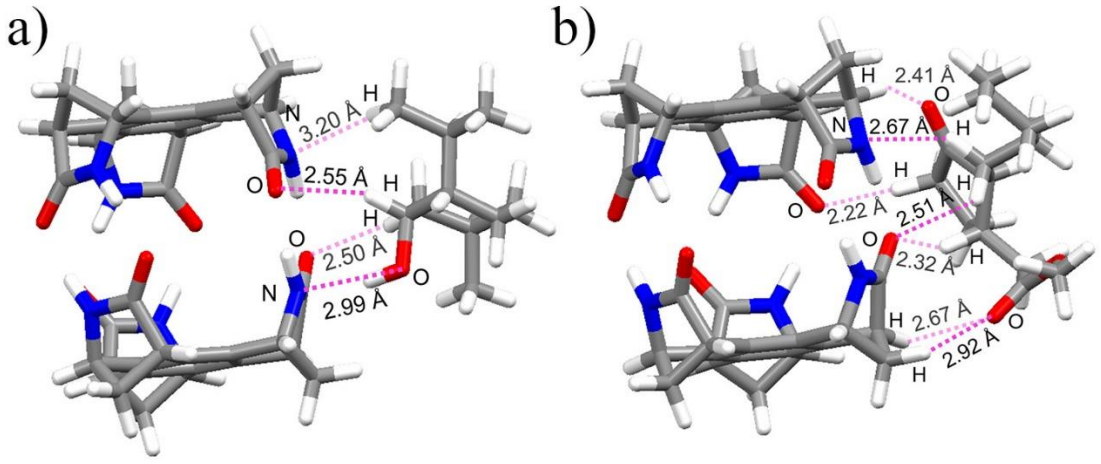

Figure 50. DFT optimized the complex a) (+)-**12**$_{dimer}$-**LMT** and b) (+)-**12**$_{dimer}$-**KRM** structures at the B3LYP-D3/6-31+G(d,p) level of theory. The pink dashed lines correspond to the bond distances of considered atomic interactions. C, grey; N, Blue; O, red; H, white.

The interactions of (–)-**12**$_{dimer}$-**LMT** and (–)-**12**$_{dimer}$-**KRM** structures were calculated by DFT with same level of theory. The corresponding optimized structures and bond distances are displayed in Fig. 51. The similar interactions between oxygen and nitrogen heteroatoms from amides and protons from enriched compounds were founds. The relative binding energies of complexes can be calculated by

$$\text{Relative Binding Energy} = E_{complex} - (E_{dimer} + E_{enriched}) \qquad \text{(unit in kcal mol}^{-1}\text{)} \qquad \text{Eq. 7}$$

While $E_{complex}$ referred to the optimized total energies of the complexes, E_{dimer} responded to the optimized total energy of each **12**$_{dimer}$ structures and $E_{enriched}$ referred to the optimized total energy of corresponding enriched compounds. The resulting relative binding energies of all complexes were evaluated and showed in Table 12. Surprisingly, the relative binding energies of each complex were not much different, which implied that all host-guest complexes showed similar energetic stability at relaxed state and the selective chiral recognition mainly took place at the early state of binding interactions.

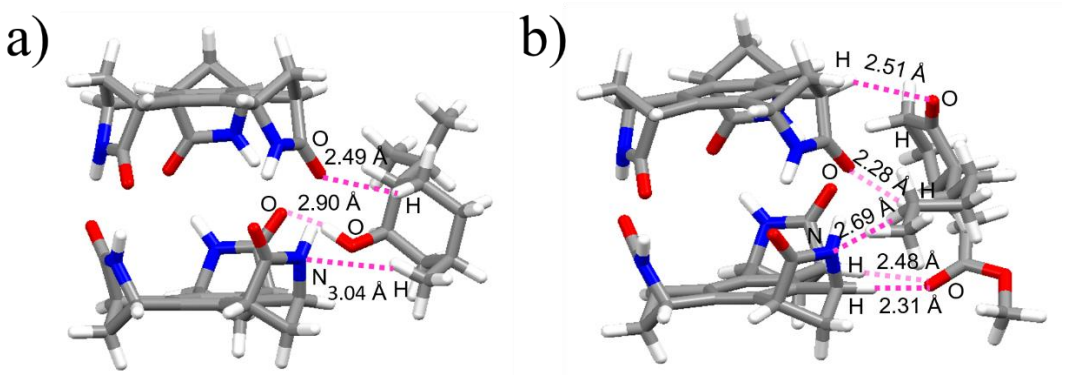

Figure 51. DFT optimized the complex a) (–)-**12**$_{dimer}$-**LMT** and b) (–)-**12**$_{dimer}$-**KRM** structures at the B3LYP-D3/6-31+G(d,p) level of theory. The pink dashed lines correspond to the bond distances of considered atomic interactions. C, grey; N, Blue; O, red; H, white.

Table 12. Relative binding energy of all complexes. Calculated at B3LYP-D3/6-31+G(d,p).

Enriched compounds	**Complexes**	**Relative binding energies (kcal mol^{-1})**
LMT	(+)-**12**$_{dimer}$-**LMT**	–16.51
	(–)-**12**$_{dimer}$-**LMT**	–10.83
KRM	(+)-**12**$_{dimer}$-**KRM**	–20.30
	(–)-**12**$_{dimer}$-**KRM**	–18.40

4.3 Conclusion

In this Chapter, performances of the synthesized cup-shaped trilactams, as found in recognitions of chiral volatile compounds in perfume, have been examined. The materials showed good enrichment performance for the compounds with $I > 1060$, especially cyclic terpenes with specific shapes and the oxygenated terpenes. Enantioselective interaction with the (+)-**12**$_{dimer}$ was also observed for terpenes with unique shapes. Both MD simulations and DFT calculation revealed that (+)-**12**$_{dimer}$ exhibited more favorable interactions with the enrich compounds via either hydrogen bonds or polarity forces, which existed in heteroatoms in the molecules. The investigated selective interaction mechanisms further scope the opportunities for these materials for the use in other applications.

4.4 Experimental section

4.4.1 Chemicals and materials

Both enantiomers of cup-shaped cyclic trilactam (+)-**12** and (–)-**12**, which formed a capsule-like dimer structure in the solid state, were prepared according to Chapter 3. Sample of perfume was purchased from a local supermarket in Thailand. A mixture of *n*-alkanes (C8-C20, purchased from Sigma Aldrich) was used as a reference to calculate the retention index (*I*) of the analyte peaks. A SPME fiber (50/30 μm DVB/CAR/PDMS, grey) and a holder were purchased from Supelco (Sigma-Aldrich, Bellefonte, PA). The instruments included a vortex mixer (Scilogex, MX-S, Rocky Hill, USA), adjustable pipettes (Eppendorf, 100-1000 μL, Hamburg, Germany), SPME apparatus (including SPME fiber CAR/PDMS, PDMS/DVB, and PDMS), a sampling stand and a fiber holder (Supelco, Bellefonte, USA), electronic balances (Sartorius, Gottingen, Germany), 2 mL screw top vials and caps (HPLC and GCMS grade, Agilent Technologies, USA), 20 mL clear headspace vial glass and caps (Agilent Technologies, USA).

4.4.2 Extraction of samples

Each material was weighed separately into a vial (each containing 1 mg of (+)-**12** and (–)-**12**) followed by addition of MeOH (500 μL). Each vial was then added with the perfume (500 μL). The vials containing (1) (+)-**12** (1 mg) and MeOH (500 μL) without the perfume, (2) (–)-**12** (1 mg) and MeOH (500 μL) without the perfume and (3) the perfume (500 μL) and MeOH (500 μL) without the materials were also prepared as the control samples. Each sample was prepared in triplicate. All the sample vials were closed with the caps and shaken for 2 min. The caps were then removed, replaced with aluminum foil punched into several channels and left at room temperature

(27 °C) for three days for recrystallization and solvent evaporation. The remaining solutions were then collected for the analysis with SPME and GC-MS.

4.4.3 Analysis of volatile compounds

The SPME fiber was conditioned at 270 °C for 1 hour via insertion into the GC injection port. The mixtures (200 μL) containing sample, material and residue solvent(s) after evaporation were transferred into 20 mL glass vials, closed with aluminum caps with sealed PTFE/silicone septa and left for the equilibrium time of 5 min. The SPME fiber was then exposed inside each vial to extract volatile compounds in the sample headspace with an extraction time of 10 min at room temperature (27 °C). The extracted samples were then injected into the injection port at 220 °C with a desorption time of 5 min in splitless mode and analyzed by using GC-QqQMS (7890A-7000, Agilent technologies Inc.), which was applied under single Q scan mode with the other quadrupoles being operated in total transfer of ion mode.

A HP-5 MS column (30 m × 0.25 mm i.d., 0.25 μm film thickness; J&W Scientific, USA) was applied. Helium (99.999%) was used as the carrier gas with a flow rate of 1 mL min^{-1}. The GC oven temperature was programmed to increase from 40 to 240 °C at a rate of 4 °C min^{-1}. The temperature of the ion source in the MS was set at 230 °C. The electron ionization voltage was –70 eV. The mass spectra were collected over the m/z range of 30–300 with a scan time of 100 ms.

4.4.4 Data processing

Data presentation and peak integration were conducted by using Agilent MassHunter software. Chromatographic peaks of interest were tentatively identified by comparing their MS spectra with those obtained from the NIST library 2017. For compound identity confirmation, the criteria were selected with a match score of > 650 and a difference of ≤ 20 units between the calculated retention index (*I*) and the literature *I* for the same (or a similar) stationary phase. All the results were further processed by using Microsoft Excel. Note that the experimental *I* of each peak was calculated by comparison with the peak retention time with that of an alkane mixture under the same experimental conditions according to the van den Dool and Kratz relationship.[63]

4.4.5 Computational simulation detail

The MD package, called GROMACS,[70] was employed for dynamics simulation to mimic the experiments, comprising of each enantiomers $\mathbf{12}_{dimer}$ and selected compounds (*l*-menthol or kharismal) in a 1:1 ratio in a ternary solvent system of MeOH, water (H_2O), and ethanol (EtOH)

in 50/35/15 %v/v, with the number of the corresponding molecules being 215, 335, 45, respectively. The workflow of MD production was illustrated in Fig. 52 with the following three assumptions: 1) the ratio between **12**$_{dimer}$ and enriched compounds is 1:1, 2) **12**$_{dimer}$ is constrained during equilibrium step, and 3) host-guest interaction is assumed to be at the nearest logical distance to each other before simulation. Initially, selected compounds were placed beside (+)-**12**$_{dimer}$ at the binding site of amide moiety separated by approximately 0.5–0.6 nm, which is within the interaction distance of van der Waals forces. Fig. 44 showed the initial simulated conformations of (–)-**12**$_{dimer}$ and (+)-**12**$_{dimer}$ with either *l*-menthol (LMT) or kharismal (KRM). The running dynamic of 5 ns was given for achieving equilibrium of the entire system under periodic boundary conditions (PBC) at 27 °C and under atmospheric pressure and a time step of 0.002 ps was used. The periodic box was defined depending on the size of **12**$_{dimer}$ and enriched compounds and amount of solvent molecules, the dimension of the box is chosen to be 3.2 × 3.2 × 3.2 nm^3. All complexes were further calculated by the quantum chemical calculation using the B3LYP-D3 method, which includes an empirical a posteriori correction term proposed by Grimme[71] to account for dispersion interactions in the pure B3LYP density functional method, with 6-31+G(d,p) basis set. The DFT calculation was performed using Gaussian09 suite of program by using the same initial molecular structures in MD to fully optimize the ground state geometry in the gas phase condition. Zero-point energy correction was considered for calculations and the local minima of each structures were confirmed without imaginary vibrational frequencies. The molecular structures were visualized using Mercury program.

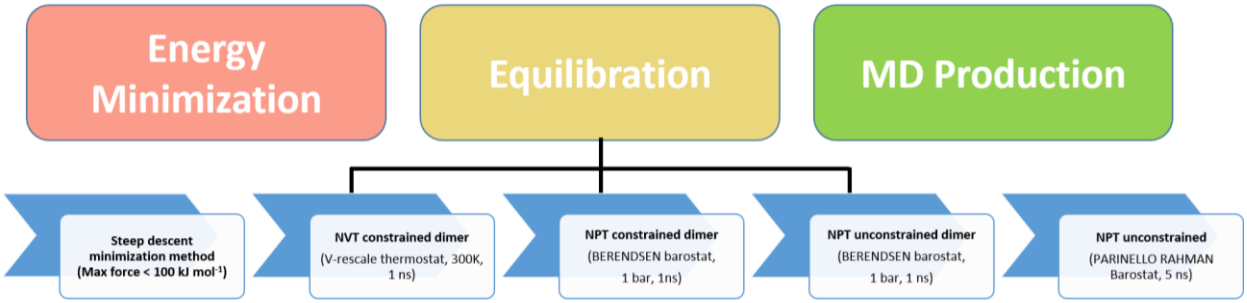

Figure 52. Workflow of MD production for host-guest equilibrium.

Conclusion

This thesis demonstrated various properties from nitrogen-doping effect on various C_3 symmetric three-dimensional curved structures both in experimental and theoretical calculations approaches. In Chapter 2, The author reported the theoretical TDDFT calculation investigation of mechanistic detailed of photophysical properties ESIPT in tris(2-hydroxyphenyltriazasumanene) revealed the effect of nitrogen atoms on triazasumanene skeleton as hydrogen bonded acceptor. The calculations revealed the single ESIPT is the main contribution afforded large Stokes shift observed in the emission spectra in solid state. In the solution state, the non-radiative decay was responded to the ESIPT-inactivation and approximately predicted by using MECP T_1/S_0 pathway.

In Chapter 3, the synthesis and structural properties of two novel chiral cup- and bowl-shaped cyclic trilactams revealed the hydrogen bonding properties of nitrogen atoms of triamides effects on the different curved structures. X-ray crystal analysis revealed the dimeric capsule-like structure of cup-shaped trilactam driven by three self-complementary NH···O type intermolecular hydrogen bonds. The favorable dimerization of the cup-shaped over the bowl-shaped trilactam was intensively studied by variable temperature proton NMR and DFT calculation, which confirmed to the solubility variation against the less polar solvent. The unique structural cup-shaped dimer was utilized as molecular synthon in metal coordination to construct the networking polymer structure.

In Chapter 4, the author showed the nitrogen atoms of triamides in the cup-shaped trilactams could provide the binding sites in molecular recognition with volatile compounds in perfume using analytical SPME and GC-MS techniques. (+)-Cup-shaped trilactam significantly exhibited recognitions with several oxygenated and cyclic volatile compounds, while (–)-cup-shaped trilactam did not. The mode of interactions between each enantiomer and selected enriched compounds were further investigated by molecular dynamic simulations and DFT calculations, showing the stable complexes through noncovalent interactions either hydrogen bonds or electrostatic interactions.

The products and marvelous properties studied in this thesis will provide useful information and view point of physical and chemical properties of nitrogen-doped effects on the curved structures in the field of buckybowls, supramolecular chemistry, and heterocyclic material. The author wishes all information contained in this thesis will distribute the knowledge and provide the novel perspectives to readers.

Abbreviations

H-bond = hydrogen bond

ESIPT = excited-state intramolecular proton transfer

AIEE = aggregated-induced emission enhancement

DFT = density functional theory

TDDFT = time-dependent density functional theory

φ = dihedral angle (phi)

EEE = trienol

KEE = monoketo

KKE = diketo

KKK = triketo

S_0 = singlet ground state

S_1 = first singlet excited state

T_1 = first triplet excited state

HPP = 2-(2'-hydroxyphenyl)pyridine

PCM = polarizable continuum model

CI = conical intersection

PES = potential energy curve

CASSCF = complete active space self-consistent field

MECP = minimum energy crossing point

PMB = *p*-methoxybenzyl

CAN = ceric ammonium nitrate

TFA = trifluoroacetic acid

MW = microwave

NMR = nuclear magnetic resonance

CTV = cyclotriveratrylene

SPME = solid phase microextraction

GC-MS = gas chromatography-mass spectroscopy

I = retention index

EF = enrichment factor

LMT = *l*-menthol

KRM = kharismal

MD = molecular dynamics

References

1. a) B. C. Brodie, *Phil. Trans. R. Soc. Lond.* **1859**, 149, 249; b) J. D. Bernal, *Proc. R. Soc. Lond.* **1924**, *A106*, 749.
2. H. W. *Kroto, J. R. Heath, S. C. Obrien, R. F. Curl, R. E. Smalley, Nature* **1985**, *318, 162.*
3. S. Iijima, *Nature* **1991**, *354*, 56.
4. P. Ruffieux, S. Wang, B. Yang, C. Sánchez, J. Liu, T. Dienel, L. Talirz, P. Shinde, C. A. Pignedoli, D. Passerone, T. Dumslaff, X. Feng, K. Müllen, R. Fasel, *Nature* **2016**, *531*, 489.
5. H. Sakurai, T. Daiko, T. Hirao, *Science* **2003**, *301*, 1878.
6. W. E. Barth, R. G. Lawton, *J. Am. Chem. Soc.* **1966**, *88*, 380.
7. H. E. Bronstein, N. Choi, L. T. Scott, *J. Am. Chem. Soc.* **2002**, *124*, 8870.
8. L. T. Scott, M. S. Bratcher, S. Hagen, *J. Am. Chem. Soc.* **1996**, *118*, 8743.
9. Y. T. Wu, J. S. Siegel, *Chem. Rev.* **2006**, *106*, 4843.
10. a) V. M. Tsefrikas, L. T. Scott, *Chem. Rev.* **2006**, *106*, 4868; b) S. Higashibayashi, H. Sakurai, *Chem. Lett.* **2011**, *40*, 122; c) T. Amaya, T. Hirao, *Chem. Rec.* **2015**, *15*, 310.
11. a) T. Amaya, K. Mori, H. L. Wu, S. Ishida, J. Nakamura, K. Murata, T. Hirao, *Chem. Commun.* **2007**, *19*, 1902; b) T. Amaya, M. Hifumi, M. Okada, Y. Shimizu, T. Moriuchi, K. Segawa, Y. Ando, T. Hirao, *J. Org. Chem.* **2011**, *76*, 8049; c) T. Amaya, Y. Inada, Y. Shimizu, A. Saeki, R. Tsuji, S. Seki, T. Hirao, *Chem. Asian. J.* **2014**, *9*, 2568; d) T. Amaya, T. Ito, T. Hirao, *Angew. Chem.* **2015**, *127*, 5573.
12. a) T. Amaya, T. Hirao, *Chem. Commun.* **2011**, *47*, 10524; b) S. Higashibayashi, R. Tsuruoka, Y. Soujanya, U. Purushotham, G. N. Sastry, S. Seki, T. Ishikawa, S. Toyota, H. Sakurai, *Bull. Chem. Soc. Jpn.* **2012**, *85*, 450.
13. H. Sakurai, T. Daiko, H. Sakane, T. Amaya, T. Hirao, *J. Am. Chem. Soc.* **2005**, *127*, 11580.
14. S. Mebs, M. Weber, P. Luger, B. M. Schmidt, H. Sakurai, S. Higashibayashi, S. Onogi, D. Lentz, *Org. Biomol. Chem.* **2012**, *10*, 2218.
15. T. Amaya, S. Seki, T. Moriuchi, K. Nakamoto, T. Nakata, H. Sakane, A. Saeki, S. Tagawa, T. Hirao, *J. Am. Chem. Soc.* **2009**, *131*, 408.
16. A.Sygula, F.R. Fronczek, R. Sygula, P.W. Rabideau, M .M. Olmstead, *J. Am. Chem. Soc.* **2007**, *129*, 3842.
17. a) A. S. Filatov, A. V. Zabula, S. N. Spipak, A. Y. Rogachev, M. A. Petrukhina, *Angew. Chem. Int. Ed.* **2014**, *53*, 140; b) S. N. Spipak, A. V. Zabula, A. S. Filatov, M. A. Petrukhina, *J. Organomet. Checm.* **2015**, *784*, 69; c) S. N. Spisak, Z. Wei, A. Y. Rogachev, T. Amaya, T. Hirao, M. Petrukhina, *Angew. Chem.* **2017**, *56*, 2582.

18. a) O. Stephan, P. M. Ajayan, C. Colliex, Ph. Redlich, J. M. Lambert, P. Bernier, P. Lefin, *Science* **1994**, *266*, 1683; b) C. N. R. Rao, K. Gopalakrishnan, A. Govindaraj, *Nano Today* **2014**, *9*, 324.
19. a) H. Wang, T. Maiyalagan, X. Wang, *ACS Catal.* **2012**, *2*, 781; b) Y. Deng, Y. Xie, K. Zou, X. Ji, *J. Mater. Chem. A* **2016**, *4*, 1144.
20. Y. Song, W. Chen, C. Zhao, S. Li, W. Wei, Y. Sun, *Angew. Chem.* **2017**, *56*, 10840.
21. a) H. Yokoi, Y. Hiraoka, S. Hiroto, D. Sakamaki, S. Seki, H. Shinokubo, *Nat commun.* **2015**, *6*, 8215; b) S. Ito, Y. Tokimaru, K. Nozaki, *Angew. Chem.* **2015**, *54*, 7256; c) V. M. Tsefrikas, A. K. Greene, L. T. Scoot, *Org. Chem. Front.* **2017**, *4*, 688; d) M. Saito, H. Shinokubo and H. Sakurai, *Mater. Chem. Front*. **2018**, *2*, 635; e) Y. Tokimaru, S. Ito and K. Nozaki, *Angew. Chem. Int. Ed.* **2017**, *56*, 15560; f) M. Takeda, S. Hiroto, H. Yokoi, S. Lee, D. Kim and, H. Shinokubo, *J. Am. Chem. Soc.* **2018**, *140*, 6336.
22. Q. Tan, S. Higashibayashi, S. Karanjit, H. Sakurai, *Nat Commun.* **2012**, *3*, 891.
23. Q. Tan, P. Kaewmati, S. Higashibayashi, M. Kawano, Y. Yakiyama, H. Sakurai, *Bull. Chem. Soc. Jpn.* **2018**, *91*, 531.
24. R. C. Haddon, *J. Am. Chem. Soc*. **1987**, *109*, 1676.
25. a) P. Kaewmati, Q. Tan, S. Higashibayashi, Y. Yakiyama, H. Sakurai, *Chem. Lett*. **2016**, *46*, 146; b) P. Kaewmati, Y. Yakiyama, H. Ohtsu, M. Kawano, S. Haesuwannakij, S. Higashibayashi, H. Sakurai, *Mater. Chem. Front*. **2018**, *2*, 514.
26. a) M. P. Lightfoot, F. S. Mair, R. G. Pritchard, J. E. Warren, *Chem. Commun*. **1999**, 1945; b) C. B. Aakeröy, A. M. Beatty, B. A. Helfrich, *J. Am. Chem. Soc*. **2002**, *124*, 14425; c) C. Kim, K. T. Kim, Y. Chang, *J. Am. Chem. Soc.* **2001**, *123*, 5586; d) Z.-T. Li, J.-L. Hou, C. Li, H.-P. Yi, *Chem. Asian J.* **2006**, *1*, 766; e) S. Sivakova, S. J. Rowan, *Chem. Soc. Rev.* **2005**, *34*, 9; f) D. González-Rodríguez, A. P. H. J. Schenning, *Chem. Matter.* **2011**, *23*, 310.
27. a) F. Hof, S. L. Craig, C. Nuckolls, J. Rebek, Jr., *Angew. Chem. Int. Ed.* **2002**, *41*, 1488; b) J. Rebek, Jr., *Angew. Chem. Int. Ed.* **2005**, *44*, 2068; c) F. Fabris, C. Zonta, G. Borsato, O. De Lucchi, *Acc. Chem. Res.* **2011**, *44*, 6, 416; d) F. Fabris, O. De Lucchi, I. Nardini, M. Crisma, A. Mazzanti, S. A. Mason, M.-H. Lemée-Cailleau, F. A. Scaramuzzo, C. Zonta, *Org. Biomol. Chem.* **2012**, *10*, 2464; e) R. Z. Pavlović, S. E. Border, T. J. Finnegan, L. Zhiquan, M. J. Gunther, E. Mūnoz, C. E. Moore, C. M. Hadad, J. D. Badjić, *J. Am. Chem. Soc.* **2019**, *141*, 16600; f) A. Meli, S. Gambaro, C. Costabile, C. Talotta, G. Della Sala, P. Tecilla, D. Milano, M. Tosolini, I. Izzo, F. De Riccardis, *Org. Biomol. Chem*. **2016**, *14*, 9055; g) H. Behera, V. Ramkumar, N. Madhavan, *Org. Biomol. Chem.* **2017**, *15*, 4937.

28. a) A. Dybala-Defratyka, P. Paneth, J. Pu, D. G. Truhlar, *J. Phys. Chem. A* **2004**, *108*, 2475; b) K. L. Han, G. Z. He, *J. Photochem. Photobiol. C* **2007**, *8*, 55; c) B. J. Siwick, H. J. Bakker, *J. Am. Chem. Soc*. **2007**, *129*, 13412; d) M. Kasha, *J. Chem. Soc. Faraday Trans*. *2* **1986**, *82*, 2379.
29. a) J. E. Kwon, S. Y. Park, *Adv. Mater*. **2011**, *23*, 3615; b) V. S. Padalkar, S. Seki, *Chem. Soc. Rev.* **2016**, *45*, 169.
30. a) Y. Zhang, J.-H. Wang, W. Zheng, T. Chen, Q.-X. Tong, D. Li, *J. Mater. Chem. B* **2014**, *2*, 4159; b) N. Suzuki, A. Fukazawa, K. Nagura, S. Saito, H. Kitoh-Nishioka, D. Yokogawa, S. Irle, S. Yamaguchi, *Angew. Chem. Int. Ed.* **2014**, *53*, 8231; c) L. Xie, Y. Chen, W. Wu, H. Guo, J. Zhao, X. Yu, *Dyes Pigm.* **2012**, *92*, 1361.
31. a) Z. Zhang, Y.-A. Chen, W.-Y. Hung, W.-F. Tang, Y.-H. Hsu, C.-L Chen, F.-Y. Meng, P.-T. Chou, *Chem. Mater.* **2016**, *28*, 8815; b) R. H. Friend, R. W. Gymer, A. B. Holmes, J. H. Burroughes, R. N. Marks, C. Taliani, D. D. C. Bradley, D. A. Dos Santos, J. L. Brédas, M. Lögdlund W. R. Salaneck, *Nature* **1999**, *397*, 121; c) S. H. Kim, S. Park, J. E. Kwon, S. Y. Park,. *Adv. Funct. Mater*. **2011**, *21*, 644.
32. a) A. C. Sedgwick, L. Wu, H.-H. Han, S. D. Bull, X.-P. He, T. D. James, J. L. Sessler, B. Z. Tang, H. Tian, J. Toon, *Chem. Soc. Rev*. **2018**, *47*, 8842; b) J. Zhao, S. Ji, Y. Chen, H. Guo, P. Yang, *Phys. Chem. Chem. Phys.* **2012**, *14*, 8803; c) S. Chen, P. Hou, J. Wang, X. Song, *RSC Adv*. **2012**, *2*, 10869.
33. a) S. Park, J. E. Kwon, S. H. Kim, J. Seo, K. Chung, S.-Y. Park, D.-J. Jang, B. M. Medina, J. Gierschner, S. Y. Park, *J. Am. Chem. Soc*. **2009**, *131*, 14043; b) T. Mutai, H. Tomoda, T. Ohkawa, Y. Yabe, K. Araki, *Angew Chem. Int. Ed.* **2008**, *47*, 9522; c) S. Kim, J. Seo, H. K. Jung, J.-J. Kim, S. Y. Park, *Adv. Mater*. **2005**, *17*, 2077.
34. a) K. Takagi, K. Ito, Y. Yamada, T. Nakashima, R. Fukuda, M. Ehara, H. Masu, *J. Org. Chem.* **2017**, *82*, 12173; b) B. An, S. Feng, K. Wen, W. Wu, H. Yuan, Q. Zhu, X. Guo, J. Zhang, *J. Org. Electron.* **2017**, *45*, 1; c) H. Li, H. Yin, X. Liu, Y. Shi, *J. At. Mol. Sci*. **2016**, *7*, 115; d) R. Omidyan, M. Iravani, *J. Phys. Chem. A* **2016**, *120*, 1012; e) Y. Shigemitsu, T. Mutai, H. Houjou K. Araki, *J. Phys. Chem. A* **2012**, *116*, 12041.
35. a) J. Waluk, *Acc. Chem. Res.* **2003**, *36*, 832; b) G.-J. Zhao, K.-L. Han, *Acc. Chem. Res.* **2012**, *45*, 404.
36. a) J. Catalán, J. C. del Valle, J. Palomar, C. Díaz, J. L. G. de Paz, *J. Phys. Chem. A* **1999**, *103*, 10921; b) S. Maheshwari, A. Chowdhury, N. Sathyamurthy, H. Mishra, H. Tripathi, M. Panda, J. Chandrasekhar, *J. Phys. Chem. A* **1999**, *103*, 6257; c) S. Park, O.-H. Kwon, S. Kim,

S. Park, M.-G. Choi, M. Cha, S. Y. Park, D.-J. Jang, *J. Am. Chem. Soc*. **2005**, *127*, 10070; d) J. Zhao, P. Li. *Commun. Comput. Chem*. **2015**, *3*, 66.

37. a) G. A. Parada, T. F. Markle, S. D. Glover, L. Hammarström, S. Ott, B. Zietz, *Chem. Eur. J.* **2015**, *21*, 6362; b) C. Han, B. Song, X. Liang, H. Pan, W. Dong, *Anal. Methods* **2019**, *11*, 2513.
38. a) M. A. Marques, E. Gross, *Annu. Rev. Phys. Chem.* **2004**, *55*, 427; b) C. Adamo, D. Jacquemin, *Chem. Soc. Rev*. **2013**, *42*, 845; c) M. Li, W. Ren, Z. He, Y. Zhu, *J. Clust. Sci.* **2017**, *28*, 2111.
39. a) Z. Tang, Y. Wang, D. Bao, M. Lv, Y. Yang, J. Tian, L. Dong, *J. Phys. Chem. A* **2017**, *121*, 8807; b) R. Pradhan, A. K. Harshan, G. S. K. Chandrika, A. Srinisan, U. Lourderaj, *J. Phys. Chem. A* **2016**, *120*, 9894; c) J. Zhao, H. Dong Y. Zheng, *J. Phys. Chem. A* **2018**, *122*, 1200; d) Q. Zhou, C. Du, L. Yang, M. Zhao, Y. Dai, P. Song, *J. Phys. Chem. A* **2017**, *121*, 4645; e) C. Y. Peng, J. Y. Shen, Y. T. Chen, P. J. Wu, W. Y. Hung, W. P. Hu, P. T. Chou, *J. Am. Chem. Soc.* **2015**, *137*, 14349; f) K. C. Tang, C. L. Chen, H. H. Chuang, J. L. Chen, Y. J. Chen, Y. C. Lin, J. Y. Shen, W. P. Hu, P. T. Chou, *J. Phys. Chem. Lett.* **2011**, *2*, 3063; g) J. Zhao, J. Chen, J. Liu, M. R. Hoffmann, *Phys. Chem. Chem. Phys.* **2015**, *17*, 11990; h) J. D. Huang, K. Yu, H. Ma, S. Chai, B. Dong, *Dyes Pigm.* **2017**, *141*, 441.
40. a) D. LeGourriérec, V. Kharlanov, R. G. Brown, W. Rettig, *J. Photochem. Photobiol. A* **1998**, *117*, 209; b) L. Kaczmarek, R. Balicki, J. Lipkowski, P. Borowicz, A. Grabowska, *J. Chem. Soc. Perkin Trans*. **1994**, *2*, 1603.
41. a) M. Capponi, I. G. Gut, B. Hellrung, G. Persy, J. Wirz, *Can. J. Chem*. **1999**, *77*, 605; b) Li Zhu, J. W. Bozzelli, *J. Phys. Chem. A* **2003**, *107*, 3696.
42. a) D. R. Yarkony, *J. Phys. Chem. A* **2001**, *105*, 6277; b) W. Domcke, D. R. Yarkony, H. Köppel in *Conical Intersections: Theory, Computation and Experiment*; World Scientific Publishing: Singapore, **2011**, Vol. 17.
43. a) M. J. Paterson, M. A. Robb, L. Blancafort, A. De Bellis, *J. Am. Chem. Soc*. **2004**, *126*, 2912; b) J. He, F. Siddique, H. Lischka, F. H. Quina, A. J. A. Aquino, *Photochem. Photobiol. Sci*. **2019**, *18*, 1972; c) X.-Y. Liu, X.-P. Chang, S.-H. Xia, G. Cui, W. Thiel, *J. Chem. Theory Comput.* **2016**, *12*, 753; c) Y.-H. Liu, S.-C. Lan, C. Zhu, S.-H. Lin, *J. Phys. Chem. A* **2015**, *119*, 6269
44. J. N. Harvey, M. Aschi, *Phys. Chem. Chem. Phys.* **1999**, *1*, 5555.
45. a) C. Lee, W. Yang, R. G. Parr, *Phys. Rev. B: Condens. Matter Mater. Phys.* **1988**, *37*, 785; b) A. D. Becke, *J. Chem. Phys*. **1993**, *98*, 5648.
46. Y. Tawada, T. Tsuneda, S. Yanagisawa, T. Yanai K. Hirao, *J. Chem. Phys*. **2004**, *120*, 8425.

47. P. Hariharan, J. Pople, *Theor. Chem. Acc*. **1973**, *28*, 213.
48. a) C. A. Kenfack, A. S. Klymchenko G. Duportail, A. Burgerc, Y. Mely, *Phys. Chem. Chem. Phys*. **2012**, *14*, 8910; b) R. Casadesús, O. Vendrell, M. Moreno, J. M. Lluch K. Morokuma, *Chem. Phys.* **2006**, *325*, 243; c) J. Tomasi, R. Cammi, J. R. Cheeseman, M. J. Frisch, F. J. Devlin, S. Gabriel, P. J. Stephens, *J. Phys. Chem. A* **2002**, *106*, 6102.
49. M. J. Frisch, G. W. Trucks, H. B. Schlegel, G. E. Scuseria, M. A. Robb, J. R. Cheeseman, G. Scalmani, V. Barone, G. A. Petersson, H. Nakatsuji, X. Li, M. Caricato, A. Marenich, J. Bloino, B. G. Janesko, R. Gomperts, B. Mennucci, H. P. Hratchian, J. V. Ortiz, A. F. Izmaylov, J. L. Sonnenberg, D. Williams-Young, F. Ding, F. Lipparini, F. Egidi, J. Goings, B. Peng, A. Petrone, T. Henderson, D. Ranasinghe, V. G. Zakrzewski, J. Gao, N. Rega, G. Zheng, W. Liang, M. Hada, M. Ehara, K. Toyota, R. Fukuda, J. Hasegawa, M. Ishida, T. Nakajima, Y. Honda, O. Kitao, H. Nakai, T. Vreven, K. Throssell, J. A. Montgomery, Jr., J. E. Peralta, F. Ogliaro, M. Bearpark, J. J. Heyd, E. Brothers, K. N. Kudin, V. N. Staroverov, T. Keith, R. Kobayashi, J. Normand, K. Raghavachari, A. Rendell, J. C. Burant, S. S. Iyengar, J. Tomasi, M. Cossi, J. M. Millam, M. Klene, C. Adamo, R. Cammi, J. W. Ochterski, R. L. Martin, K. Morokuma, O. Farkas, J. B. Foresman and D. J. Fox, *Gaussian 09*, Gaussian, Inc., Wallingford CT, **2016**.
50. A. Greenberg, C. M. Breneman, J. F. Liebman in *The Amide Linkage: Selected Structural Aspects in Chemistry, Biochemistry, and Materials Science*, Wiley-Interscience, **2000**.
51. a) V. R. Pattabiraman, J. W. Bode *Nature* **2011**, *480*, 471; b) S. Mahesh, K.-C. Tang, M. Raj, *Molecules* **2018**, *23*, 2615; c) J. I. Mujika, J. M. Matxain, L. A. Eriksson, X. Lopez, *Chem. Eur. J.* **2006**, *12*, 7215.
52. a) G. R. Desiraju, *Angew. Chem. Int. Ed. Engl*. **1995**, *34*, 2311; b) R. D. B. Walsh, M. W. Bradner, S. Fleischman, L. A. Morales, B. Moulton, N. Rodríguez-Hornendo, M. J. Zaworotko, *Chem. Commun*. **2003**, 186.
53. a) W. C. Still, *Acc. Chem. Res*. **1996**, *29*, 155; b) D. Q. McDonald, W. C. Still, *J. Am. Chem. Soc*. **1996**, *118*, 2073.
54. a) C. Moberg, *Angew. Chem. Int. Ed*. **1998**, *37*, 248; b) M. M. Conn, J. Rebek, Jr., *Chem Rev*. **1997**, *97*, 1647; c) R. Shomura, S. Higashibayashi, H. Sakurai, Y. Matsushita, A. Sato, M. Higuchi, *Tetrahedron Lett.* **2012**, *53*, 783; d) F. Imabeppu, K. Katagiri, H. Masu, T. Kato, M. Tominaga, B. Therrien, H. Takayanagi, E. Kaji, K. Yamaguchi, H. Kagechika, I. Azumaya, *Tetrahedron Lett.* **2006**, *47*, 413; e) N. Fujimoto, M. Matsumura, I. Azumaya, S. Nishiyama, H. Masu, H. Kagechika, A. Tanatani, *Chem. Commun*. **2012**, *48*, 4809; f) R. Yamakado, K. Mikami, K. Takagi, I. Azumaya, S. Sugimoto, S. Matsuoka, M. Suzuki, K. Katagiri, M.

Uchiyama, A. Muranaka, *Chem. Eur. J.* **2013**, *19*, 11853; g) Y. Saito, M. Satake, R. Mori, M. Okayasu, H. Masu, M. Tominaga, K. Katagiri, K.Yamaguchi, S. Kikkawa, H. Hikawa, I. Azumaya, *Org. Biomol. Chem.* **2020**, *18*, 230; h) R. A. Tromans, T. S. Carter, L. Chabanne, M. P. Crump, H. Li, J. V. Matlock, M. G. Orchard, A. P. Davis, *Nat. Chem*. **2019**, *11*, 52; i) D. Beaudoin, F. Rominger, M. Mastalerz, *Angew. Chem. Int. Ed.* **2016**, *55*, 15599.

55. a) S. Tartaggia, O. De Lucchi, A. Gambaro, R. Zangrando, F. Fabris, A. Scarso, *Chem. Eur. J.* **2013**, *19*, 5701; b) H. Siegel, R. B. Martin, *Chem. Rev*. **1982**, *82*, 385; c) O. Clement, B. M. Rapko, B. P. Hay, *Coord. Chem. Rev*. **1998**, *170*, 203.
56. E. P. Balskus, E. N. Jacobsen, *J. Am. Chem. Soc*. **2006**, *128*, 6810.
57. A. Scarso, L. Pellizzaro, O. De Lucchi, A. Linden, F. Fabris, *Angew. Chem. Int. Ed.* **2007**, *46*, 4972.
58. Molecular volumes were calculated with the program MacSpartan.
59. a) D. F. Nogales, J.-S. Ma, D. A. Lightner, *Tetrahedron* **1993**, *49*, 2361; b) M. T. Huggins, D.A. Lightner, *Monatsh Chem*. **2001**, *132*, 203; c) J. G. Morton, C. L. Joe, M. C. Stolla, S. R. Koshland, C. H. Londergan, M. H. Schofield, *J. Chem. Educ*. **2015**, *92*, 1086.
60. P. A. Kollman, L. C. Allen, *Chem. Rev*. **1972**, *72*, 283.
61. a) A. Long, O. Perraud, M. Albalat, V. Robert, J.-P. Dutasta, A. Martinez, *J. Org. Chem.* **2018**, *83*, 6301; b) L. Zhiquan, H. Xie, S. E. Border, J. Gallucci, R. Z. Pavlović, J. D. Badjić, *J. Am. Chem. Soc*. **2018**, *140*, 11091.
62. a) A. Chisvert, M. López-Nogueroles, A. Salvador, P. Miralles, in *Analysis of Cosmetic Products*, ed. A. Salvador, A. Chisvert, Elsevier, Boston, second edition, **2018**, *10*, 225-248; b) A. Amenduni, M. Brattoli, G. de Gennaro, F. Massari, J. Palmisani, M. Tutino, *Environ. Eng. Manag. J*. **2016**, *15*, 1963.
63. M. Jiang, C. Kulsing, Y. Nolvachai, P. J. Marriott, *Anal. Chem*. **2015**, *87*, 5753.
64. H. Kataoka, A. Ishizaki, K. Saito, *Anal. Methods*, **2016**, *8*, 5773.
65. a) C. Kulsing, P. Rawson, R. L. Webster, D. J. Evans, P. J. Marriott, *Energy Fuels*, 2017, 31, 8978; b) Y. Nolvachai, C. Kulsing, R. I. Boysen, M. T. Matyska, J. J. Pesek, P. J. Marriott, M. T. W. Hearn, *Food Chem*. **2014**, *174*, 434.
66. Y. Nolvachai, C. Kulsing and P. J. Marriott, *TrAC, Trends Anal. Chem*. **2017**, *96*, 124.
67. Z.-Y. Gu, C.-X. Yang, N. Chang, X.-P. Yan, *Acc. Chem. Res*. **2011**, *45*, 734.
68. M. Smith, J. C. Smith, *ChemRxiv*, **2020**, doi.org/10.26434/chemrxiv.11871402.v4.
69. a) Y. H. Xie, A and K. Soh, *Mater. Lett.* **2005**, *59*, 971; b) C. Sandoval, C. Castro, L. Gargallo, D. Radic and J. Freire, *Polymer*, **2005**, *46*, 10437; c) H. Cheng, A. C. Cooper, G. P. Pez, M. K. Kostov, P. Piotrowski and S. J. Stuart, *J. Phys. Chem. B* **2005**, *109*, 3780.

70. E. Lindahl, B. Hess and D. van der Spoel, *J. Mol. Mod*. **2001**, *7*, 306; b) H. J. C. Berendsen, D. van der Spoel and R. van Drunen, *Comput. Phys. Commun*. **1995**, *91*, 43.
71. A. Grimme, J. Antony, S. Ehrlich and H. Krieg, *J. Chem. Phys.* **2010**, *132*, 154104.

Acknowledgements

The author would like to express her gratefulness and appreciation to all the supporters, without them the author could have not complete all thesis works.

First of all, the author would like to give her deepest gratitude to Prof. Dr. Hidehiro Sakurai, her supervisor, for all of his suggestions, comments and guidance. He kindly supported and respected to the author's opinions and interests. The author would like to give a special thanks to Prof. Dr. Masahiro Ehara from the Institute for Molecular Science for all of his kindly assistantships in calculation work. He gave very valuable comments and suggestions to point out how to improve the author's works without hesitation.

The author would like to thank Assoc. Prof. Dr. Yumi Yakiyama for all X-ray measurements and kindly giving the author beneficial discussions and suggestions.

The author want to thank Assoc. Prof. Dr. Ken Kokubo, Assist. Prof. Dr. Yuta Uetake, and Assist. Prof. Dr. Naohiko Ikuma, for all the fruitful suggestions and discussions.

The author want to express special thanks to Dr. Chadin Kulsing and Alice from Chulalongkorn University, who supported the author regarding SPME and GC-MS for wonderful results and useful discussions.

Thanks to all Thai members in this group, Niti, Or, and Ing for their friendships and assistantships, you guys are the idol for the author. Especially, big thanks to Ing who is the author's mentor for valuable suggestions and guidance. The author also want to thanks Champ and Peet for their assistances and spending wonderful time in the laboratory.

The author would like to thanks to my family and friends in Thailand, who encouraged and supported the author to pursue the Doctoral Degree. Especially for Joe and Min, without your encouragement, the author may give up and go out of the track. Thank you so much.

Big thanks for all Sakurai group members for precious experiences in laboratory for work hard and party harder. Thank you for sharing your knowledges, experiences, and discussion to fulfill the author's precious and unforgettable five years in Japan.

Finally, the author would like to thank MEXT scholarship for fund supporting during in Japan.